福 井 大 学 工 学 審 査

学位論文[博士(工学)]

A Dissertation Submitted to the

University of Fukui for the Degree of

Doctor of Engineering

Study on a Yarn Suction Gun with High Performance

(高性能ヤーンサクションガンに関する研究)

2010, September

Yonggui Li

Contents

Chapter 1
Introduction

1.1 What is a Yarn Suction Gun?

A yarn suction gun, i.e. aspirator suction gun, is a kind of fluid machinery, sucking a running yarn by both injection mechanism and friction between the yarn surface and high-speed air. The term “yarn” means all kinds of strand material.

Figure 1.1 is the schematic diagram of a typical yarn suction gun. The compressed air from a supply of air, which is under a constant pressure, enters the yarn suction gun through the inlet of air chamber ①, as shown in Fig. 1.1(a), and jets from compressed-air inflow tubes ② to the yarn channel of a nozzle. Details of the nozzle are shown in Fig. 1.1(b). The axes of four compressed-air inflow tubes have both circumferential and axial components of the yarn channel of the nozzle. The compressed air issued from the compressed-air inflow tubes expands, helically passes through a yarn propulsion tube, which is composed of a de Laval tube and a straight tube, and flows out from the exit ③ of the yarn suction gun. A running yarn sucked from the entrance ④ of the yarn inhalation tube is given high propulsion in the yarn propulsion tube by the air issued from the compressed-air inflow tubes and blown out from the exit ③ together with the issued air. Generally, the exit of the straight tube is connected by a flexible tube to a container of waste yarn. The yarn is discharged via the flexible tube into the container.

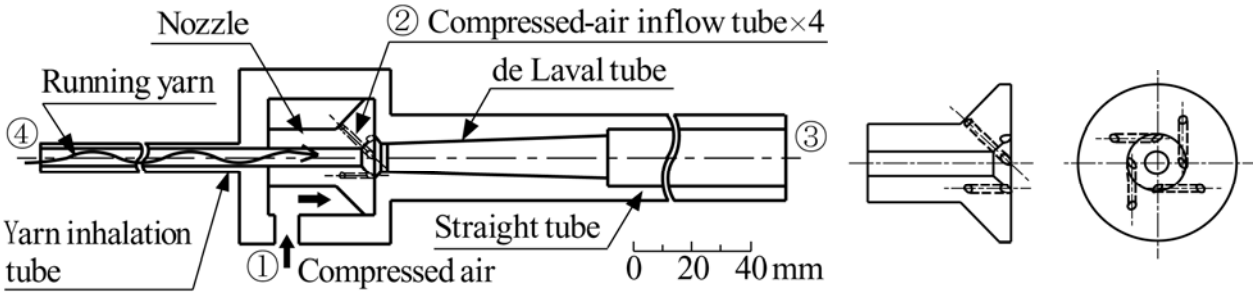

(a) General view of yarn suction gun (b) Nozzle

Figure 1.1 Schematic diagram of a typical yarn suction gun.

Compressed air is mostly used as a working fluid of yarn suction gun. Besides compressed air, water can also be used. For example, Yamaguti et al. (1973, Toyobo Co., LTD., Japan) purposed a yarn suction gun based on the idea of utilizing pressurized water instead of compressed air [1]. Sano et al. (1987, Toray Industries, Inc., Japan**)** gave details about a similar yarn-threading method and device [2].

1.2 Application of Yarn Suction Gun

The yarn suction gun has wide application. In the production and processing of fiber, yarn or filament is delivered from spinnerets, drawn, twisted or/and wound onto a bobbin. The yarn suction gun is extensively used for operations such as string-up in spinning and drawing, and doffing, during the time the filled package is being doffed and is replaced with an empty one which is put into a new operation. It is also used for removing undesirable yarn from the surface of a bobbin, which is called stripping [3].

Some fibers are formed by melt spinning, that is by melting the thermoplastic, forcing (extruding) the molten polymer through a small orifice (spinneret), cooling, and then using that extrudate, perhaps after having undergone other treatments such as drawing, as a fiber [4]. At the beginning of spinning, as shown in Fig. 1.2, a filament yarn delivered form the spinneret is sucked with a yarn suction gun, threaded to pass guide rollers and other devices such as interlacer, twisting disc and so on, and finally wound on a reel to start a production.

During doffing, the yarn suction gun is used to transfer a running yarn from a windup bobbin to another. The running yarn is captured and held firmly so that the yarn is broken owing to the rotation of the spool. The running yarn is drawn through the yarn suction gun into a waste yarn container. The rotation of the winding spool is then stopped so that the full spool is removed and replaced with an empty one. During this time the yarn is allowed to continue to run through the guide eye and into the yarn suction gun so that no slack occurs in the yarn [5]. The running yarn is then replaced around the empty spool with the yarn suction gun for starting the production. The yarn must be withdrawn at appropriate speed and tension to assure continuous production while doffing yarn package.

These operations are well known in the production of fiber. There is, therefore, no need for detailed description herein.

A yarn suction gun is also used for producing nonwoven fabrics [6, 7].

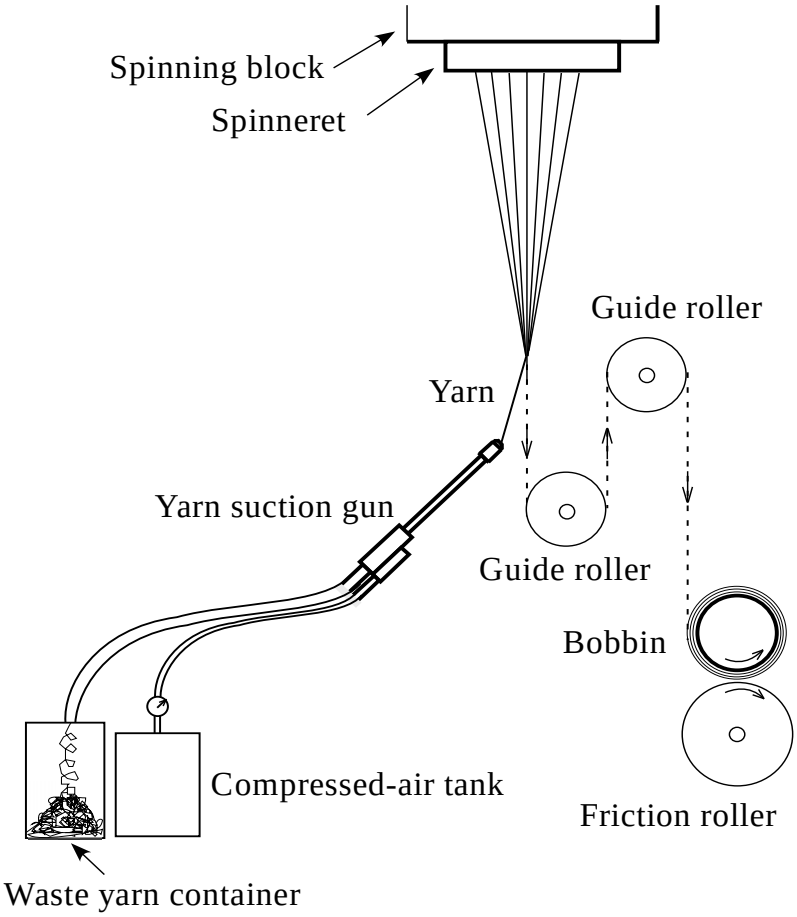

Figure 1.2 An example of apparatus for spinning fiber.

1.3 Required Performance for Yarn Suction Gun

For different fiber products and spinning systems, yarns are produced at different speeds, which require the corresponding suction capacity for a yarn suction gun to suck and discharge a yarn. An appropriate suction force must be used to assure entrainment of the yarn without yarn breakage due to over-large yarn tension. The design of a yarn suction gun is closely associated with yarn speed and yarn regularity such as fineness, strength and apparent friction coefficient and so on, and also is based on available pressure of compressed air. There are now three main types of yarn suction guns for production of POY, DTY and FDY.

On the whole, a required yarn suction gun is capable of giving powerful suction of a yarn with less noise, and is very economical because of high energy efficiency, namely low consumption of compressed air. A yarn suction gun with high performance is also easy, convenient to operate and maintain, and offers the durability to withstand the strong friction at a lighter weight. The safety standard must be met by the yarn suction gun using the highly compressed air, some of which is up to 1.2 MPa.

1.4 Survey of Previous Research

Accompanied with the development of fiber spinning technology, engineers engaging in fiber production have been trying to get the yarn suction gun with high performance. Some works have been reported on the yarn suction gun since the first patent [8] for a yarn handling device, i.e. yarn suction gun used for yarn production, was filed as early as in 1949. These works focused on the improvement of suction capacity and noise reduction.

1.4.1 Improvement in Suction Capacity of Yarn Suction Gun

A yarn suction gun was developed on the base of a waste collection apparatus [5] positioned between two cap twisters, through which airflow draws waste yarn into a waste collection basket during the time that the filled packages are being doffed and the threading is started on the apparatus for the formation of a new package, namely doffing operation.

Miller et al. (1949, du Pont company, USA) improved the above waste collection apparatus, and firstly supplied a portable yarn handling device capable of picking up a running yarn and maintaining the yarn under tension until it has been transferred to a yarn take-up or winding device [8], as shown in Fig. 1.3. This is the embryonic form of yarn suction gun. With the aid of this device an operator can carry out an entire string-up operation with one hand. Doffing operations are also facilitated. This invention represents an important improvement in yarn handling devices. However, such devices are unsatisfactory because they need the adjustment from high suction - low tension to the low suction - high tension condition of operations. To overcome this drawback, Ashby and Bunting et al (1960, du Pont Company) [9, 10, 11] made some improvements in devices of the Miller's type and provided a yarn suction gun capable of picking up a high-speed running yarn very rapidly to effectively minimize drops in the yarn line tension while maintaining adequate yarn tension during the

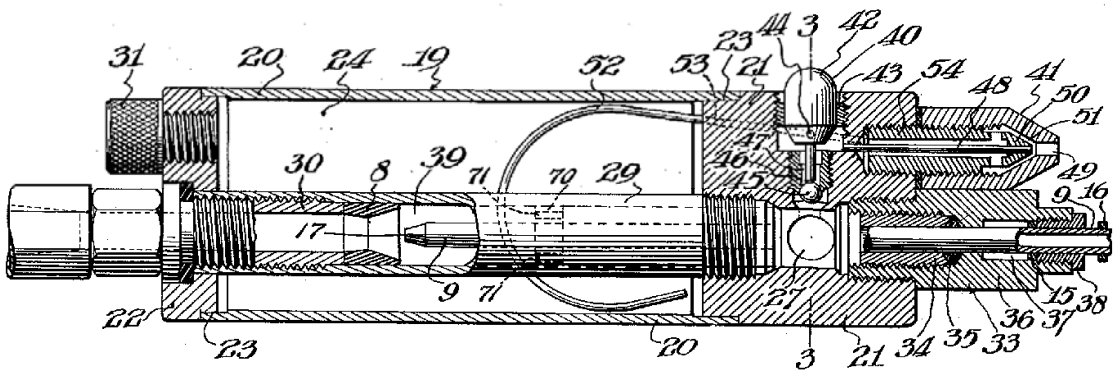

Figure 1.3 Yarn suction gun of Miller's type [8]. A yarn moves from right to left.

cut and pick-up periods and during the subsequent transfer of the running end of yarn to a winder or other device without the need for the aforementioned adjustment operations. The improved action of the new apparatus is considered to provide substantial benefits in the production of commercial yarns. The improved yarn suction gun could be used to handle the polyester fiber yarn running at a speed of up to 3,000 yards per minute.

For improving the productivity of spinning equipment to lower spinning costs, one way is to increase spinning speed. The above yarn suction gun has the airflow geometry similar to that of an air-jet loom [12, 13] by virtue of Bernoulli's principle and therefore is unable to produce enough yarn suction force to meet the requirements of high-speed spinning process thereafter. Commercially available yarn suction gun had been found unsatisfactory for handling the yarn at higher speed (3,000 to 5,000 yards per minute). Accompanied with the increase in the spinning speed, many works have been devoted to the improvement of the performance of yarn suction gun to meet the requirements of high-speed spinning process.

Richter and Cranston (1967, Leesona corporation, USA) [14] designed a yarn handling apparatus, using a vortex to increase the capacity of a aspirator, i.e. yarn suction gun, for keeping the cut yarn moving after it has been diverted to the aspirator. As shown in Fig. 1.4, the end of the conduit is provided with a plurality of helical lands and grooves, which cause the compressed air to helically enter the throat in the form of a vortex. The vortex causes the sucked yarn to follow a generally helical path transverse to a yarn propulsion tube. The apparatus is capable of handling a 1300 denier yarn advancing at a speed up to 5,000 yards per minute with an operating air pressure of 80 p.s.i. Vanderip and Cranston (1969) [15] filed an improved aspirator-shear unit for rapidly cutting and handling a rapidly moving yarn without slowing the movement of the yarn.

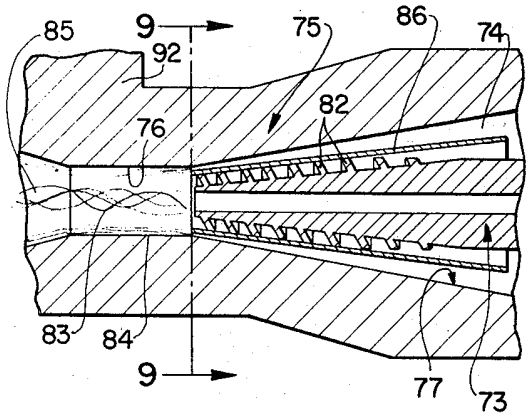

Figure 1.4 A conduit with helical grooves in yarn suction gun of Richter's type [14]. A yarn moves from right to left.

Sighieri and Colleoni (1977) also developed a device for capturing and removing textile yarns by suction and pneumatic entraining [16], namely yarn suction gun, the nozzle of which has no air injection hole but a helical groove, formed by a square multiple screw thread for imparting a rotary motion to the high speed airflow and for thus improving the discharge of the yarn, as shown in Fig. 1.5. The performance of this yarn suction gun, however, was not described. This invention is considered to be a subdivision of the Richter's type one.

McFall and Waynesboro (1978, du Pont Company) [17] synthesized the Miller's and Richter's type yarn suction guns to make a new one with improved efficiency and less noise, which was available to take up the running yarn at a speed of up to 4570 m/min when the device was operated at 5.6 kgf/cm^2 gage pressure. In this yarn suction gun, Frusto-conical surface is provided with five or six flutes, as shown in Fig. 1.6.

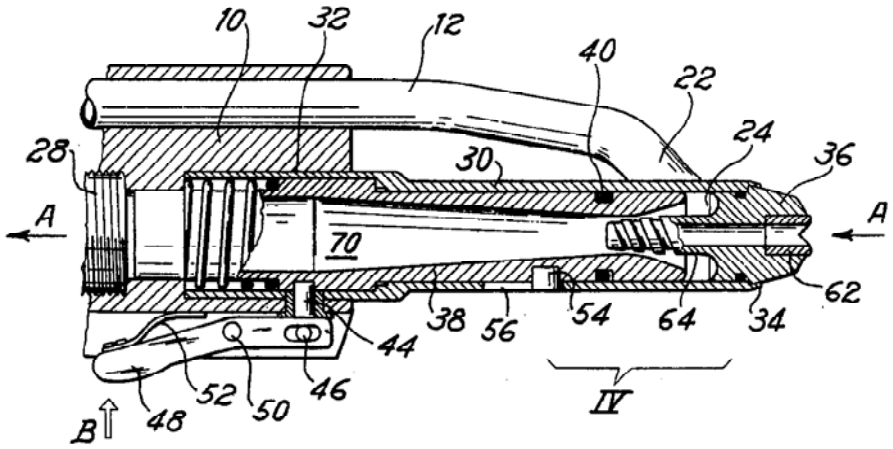

Figure 1.5 Yarn suction gun with a nozzle having a helical groove [16]. A yarn moves from right to left.

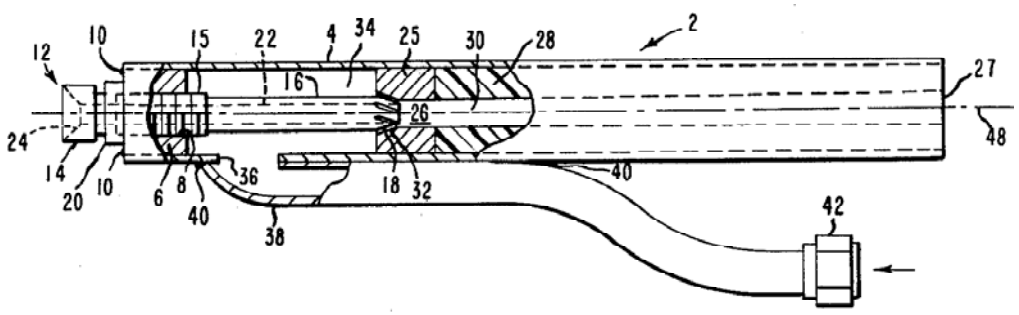

Figure 1.6 Yarn suction gun invented by McFall and Waynesboro [17]. A yarn moves from left to right.

A suction gun being fed with a pressurized liquid jet of not less than 80 kgf/cm^2 produced a state of attracting the yarn running at a speed of not less than 4,500 m/min [1, 2]. However, such device was complex, requiring an auxiliary mechanism installed at the front position of the suction gun to promote the initial attraction of the yarn since the liquid may be insufficient to create a high vacuum to draw the yarn into the yarn-guide hole.

With the progress of technology, a high-speed winder with a processing speed of 6000 m/min had been developed for practical application at the end of 1980s [18]. In such a high-speed fiber spinning device, a yarn suction gun should be able to draw the yarn at a speed of not less than 6000 m/min. However the suction ability of an air sucker had come to be insufficient.

On the basis of the yarn suction gun invented by McFall and Waynesboro, Tseng (1997) carried out an improvement by adding an accelerator in the gun [19], as shown in Fig. 1.7. The yarn suction gun allows compressed air introduced into it via a first rear end to flow into a cyclone producer and an accelerator in the gun to produce accelerated cyclonic air-flows. It is characterized in that the cyclone producer and the accelerator may either be provided at their rear ends with conic surfaces having a plurality of helical grooves or be provided at their respective stepped surfaces with several sets of inclined through holes in different inclinations to generate even stronger accelerated cyclonic airflow to suck and guide the yarn into and through the gun. However, the detailed suction capacity of the yarn suction gun is not described in this patent.

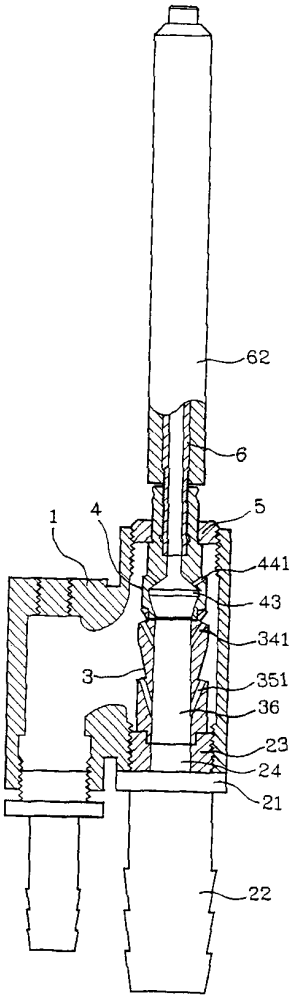

Figure 1.7 Yarn suction gun with an accelerator [19].

1.4.2 Reduction of Noise Pollution

Compressed air is the common fluid used to a yarn suction gun, although other fluids may be used. The compressed air may be supplied at a pressure ranging from 0.4 to 1.2 MPa (gauge pressure) or higher so that the noise offensive to ear is generated by the yarn suction gun during yarn threading operation, which damages physiological and psychological health of workers. For example, the noise level can sometimes exceed a level of 90 db, above which a worker must provided with ear protection. There always exists a need for reducing the noise associated with operation of the yarn suction gun, which are accomplished partly by using special design and materials.

Cylindrical insert 28 in Fig. 1.6 is made of plastic such as epoxy resin for noise reduction purposes. This yarn suction gun exhibits a greater suction power than the one with no flutes, without any increase in air consumption. The presence of the flutes at a proper angle produced a marked decrease in noise from 82 db at 0° to 60 db for flutes at a 30° angle [17].

The noise pollution level can also be reduced using water as the working fluid of a yarn suction gun, but at the price of decreasing suction capacity [1, 2].

1.4.3 Improvement in Durability and Convenience

A yarn suction gun should be in a convenient size and shape for easy portability and storage. It is made of any lightweight material, such as aluminum, stainless steel. The materials of yarn inhalation tube, particularly the rear of it, is required to be with a high wear resistance against abrasion, but at relatively low hardness to avoid damaging parts of spinning machine. For example, a marked improvement was achieved using a nylon/glass fiber composite instead of steel [20].

1.5 Present Situation and Problems

So-called super-high-speed spinning is at the wind-up speed above 6000 and up to 10000 m/min, even more [18]. The yarn-sucking speed available from the conventional yarn suction gun is low. For introduction of the super-high-speed winder in industry, the rotation of the winding roller has to be slowed down so that the yarn suction gun can capture the running yarn, and after threading, the winding roller is sped up to regular speed. This may be one mode of threading with the use of the conventional yarn suction gun, but in this mode the available high-speed is not fully used and the superior high-speed winder cannot display its full

performance. Hence the demand has developed for new yarn suction gun with super-strong suction capacity.

The supplied air pressure may be increased for the purpose of enhancing the yarn suction force, but the increase in the supplied air pressure is not a practical solution because it will also produce an increased negative impact such as increasing energy consumption and noise pollution etc. The air velocity can be increased through the decrease in the inner diameter of yarn propulsion pipe so that the suction performance can be maintained with smaller consumption of compressed air. However, the pressure at the inlet of the yarn inhalation tube will be increased, which will result in the difficulty in sucking a running yarn into the gun.

1.6 Aim of the Research

In the textile machinery subjects, there are many kinds of fluid machinery using airflow, e.g. an interlacer in interlacing process [21-31], an air-jet loom in weaving process [12, 13, 35, 36], etc. The basic studies of these subjects have been carried out actively by several researchers.

A yarn suction gun plays an important role in fiber production. There is a growing need for the yarn suction gun which is more energy efficient. However, there is little literature, especially research report, on the study of the gun except for the aforementioned patents [1-11, 14-17, 19]. There is a lack of systematic research on the yarn suction gun, which makes it difficult for researcher to compare his products with others and thereby improve them. It is therefore tried by us to systematically investigate the geometrical effects of a yarn suction gun on the suction efficiency, flow patterns and yarn behavior, and then obtain a yarn suction gun with high performance such as strong suction of yarn and low consumption of compressed air, and finally give a basic explanation of the working mechanism.

The aim of this research is to provide a design theory for yarn suction gun from the viewpoint of fluid mechanics, which will give a technological support for designing the yarn suction gun with high suction performance using low energy.

1.7 Organization of Dissertation

The dissertation is organized as follows.

Chapter 1 introduces the background of this work, including the technologies that underlie it and the previous research in this area, and gives the overall organization of the

dissertation.

In Chapter 2 the focus is on investigating effects of the geometrical parameters on the yarn suction force, mass flow rate of compressed-air and yarn suction efficiency in order to obtain the optimum geometry on the basis of the energy efficiency. The performance valuation method is also discussed.

In Chapter 3 we numerically investigate flow patterns in a yarn suction gun and dependence of the flow patterns on the supplied air pressure. The simulated results are compared with some experimental results, and the relationship between the suction efficiency and the flow characteristics is analyzed.

Chapter 4 is concerned with the simulated airflow patterns in the yarn suction gun with different geometrical parameters and discussion on the relationship between the flow patterns and yarn suction force.

In Chapter 5 geometrical effects of the yarn suction gun on yarn behavior are investigated by measuring postures of a running yarn with a still camera. The relationship between the yarn posture and yarn suction force is also discussed.

Chapter 6 is devoted to investigating the characteristics of yarn motion in the yarn suction gun and effects of airflow geometries with a high-speed video camera.

Finally, Chapter 7 presents our conclusions and future research in this area.

References

[1] Yamaguti K, Takahashi S (1973) Yarn suction apparatus. Japanese Utility Model Publication SHO51-28424

[2] Sano T, Sekido T, Ogasawara M (1987) Yarn-threading method and device. U. S. Patent 4844315

[3] McFall A, Waynesboro V (1978) Yarn-handling device. U.S. Patent 4181247

[4] Vassilatos G (2002) High speed melt-spinning of fibers. U.S. Patent 6432340 B1

[5] Burkholder A (1940) Waste collection apparatus. U.S. Patent 2206834

[6] Kaneko A, Higashiya N and Hamasuna H (1991) Filament threading in an air gun for producing nonwoven fabrics. U.S Patent 5191680

[7] Kaneko A, Higashiya N and Hamasuna H (1991) Yarn suction gun for producing nonwoven fabrics. China Patent 91109278.1

[8] Miller C. E, Staunton V (1949) Yarn handling device. U.S. Patent 2667964

[9] Ashby W, Bunting W, Wilmington J et al (1960) Improved yarn handling sucker gun. U.S. Patent 3094262

[10] Bunting W, Wilmington D, Meagher R, Wallingford P, Swayne K, Hockessin D, Work J and Horsham P (1962) Yarn handling apparatus. U.S. Patent 3175290

[11] Ashby W, Chattanooga T, Bunting W, et al (1962) Fluid pressure method for transferring yarn. U.S. Patent 3156395

[12] Ishida M, Okajima A(1994) Flow characteristic of the main nozzle in an air-jet loom Part I: measuring flow in the main nozzle. *Text Res J*, 64, 10-20

[13] Mohamed M, Salama M (1986) Mechanics of a single nozzle air-jet filling insertion system Part I: nozzle design and performance. *Text Res J*, 56, 683-690

[14] Richter H, Cranston R. Warwick, R (1967) Yarn handling apparatus. U.S. Patent 3452910

[15] Vanderip H, Cranston R (1969) Yarn handling method and apparatus. U.S. Patent 3570339

[16] Sighieri P, Colleoni G (1977) Device for capturing and removing textile yarns by suction and pneumatic entraining. U.S. Patent 4114790

[17] McFall A, Waynesboro V (1978) Yarn-handling device. U.S. Patent 4181247

[18] Tanimura S, Nagata, M (1990) Retrospect of textile machinery in the 4th OTEMAS “89”. *J Text Mach Soc Japan*, **36**, 1-8

[19] Tseng C (1997) Ultra-high speed suction gun. U.S. Patent 5857606

[20] Zhao H, Wu Q (1996) Application and modification of a yarn suction gun for FDY. *Chemical Fiber and Textile* (in Chinese), **5**, 47-48

[21] Iemoto Y, Chono S, Kasamatsu K, Lou W (1999) Size effect of interlacer Part 1: Number of tangles and yarn motion. *J Text Eng*, **45**, 71-77

[22] Iemoto Y, Chono S, Qin H, Lou W (2000) Size effect of interlacer Part 2: Pressure distribution of air flow in interlacers. *J Text Eng*, **46**, 11-19

[23] Lou W, Iemoto Y, Chono S (2000) Size effect of interlacer Part 3: Formulation of number of tangles. *J Text Eng*, **46**, 53-61

[24] Ge M, Iemoto Y, Tanoue S (2002) Frictional strength of entanglement of interlaced yarns. *J Text Eng*, **48**, 85-90.

[25] Ge M, Iemoto Y, Tanoue S (2002) Tangling angle of interlaced yarns. *J Text Eng*, **48**, 129-135

[26] Murakami K, Tokunaga K, Nomura S, Naito S, Abe M (2006) Characteristics of incompressible air flow in an interlacer. *J Text Eng*, **52**, 73-79

[27] Tokunaga K, Murakami K, Kitamura M, Nomura S, Naito S (2006) Characteristics of compressible air flow in an interlacer and yarn entanglement. *J Text Eng*, **52**, 121-129

[28] Qiu H, Iemoto Y, Tanoue S (2007) Effects of cross-sectional shape of yarn duct of interlacer on the properties of interlaced yarn. *J Text Eng*, **53**, 1-8

[29] Qiu H, Iemoto Y, Tanoue S (2007) Yarn motion in interlacers with various cross-sectional shapes of yarn duct. *J Text Eng*, **53**, 59-67

[30] Iemoto Y, Tanoue S (2008) Interlacing process of multiple filament yarn. *J Text Eng*. **54**, 207-215

[31] Iemoto Y, Tanoue S, Lu J, Takano T (2009) Effects of size of interlacer on air flow in a yarn duct. *J Text Eng*, **55**, 111-118

[35] Adanur S, Bakhtiyarov S (1996) Analysis of air flow in single nozzle air-jet filling insertion: corrugated channel model. *Text Res J*, **66**, 401-406

[36] Shintani R, Okajima A (2002) Air flow through a weft passage of profile reed in air-jet looms. *J Text Eng*, **48**, 56-63

Chapter 2
Geometrical Effect of Yarn Suction Gun on the Yarn Suction Characteristics

List of Symbols

x, y, z	Cartesian coordinates
ϕ	Compressed-air inflow angle of nozzle
θ	Passage diverging angle of nozzle
α	Converging angle of de Laval tube
D	Throat diameter of de Laval tube
L	Length of yarn propulsion tube
v	Yarn speed
p	Supplied air pressure (gauge pressure)
t	Time
F	Yarn suction force
F_m	Mean yarn suction force
G	Air mass flow rate
η	Yarn suction efficiency

2.1 Introduction

Since a yarn suction gun is a kind of fluid machinery using compressed air, the airflow geometry in the gun has a significant effect on the yarn suction capacity.

In this chapter we focus consideration on the airflow geometry of a yarn suction gun and experimentally discuss the geometrical effects on the yarn suction characteristics. The aim of the research is to obtain a yarn suction gun with high suction efficiency on the basis of energy efficiency, and a tentative understanding of the design principle.

2.2 Experiment

Figure 2.1 is an outline of the experimental apparatus. The compressed air in a compressor ① was regulated to a set pressure by a pressure adjuster ②, passed through a valve ③ and flow meter ④, and arrived in a rectification tank ⑤. The air rectified by the rectification tank was supplied to a yarn suction gun ⑦ and flowed out into the atmosphere with a yarn. The tension and speed of the yarn released from a pirn ⑧ were regulated by a tension

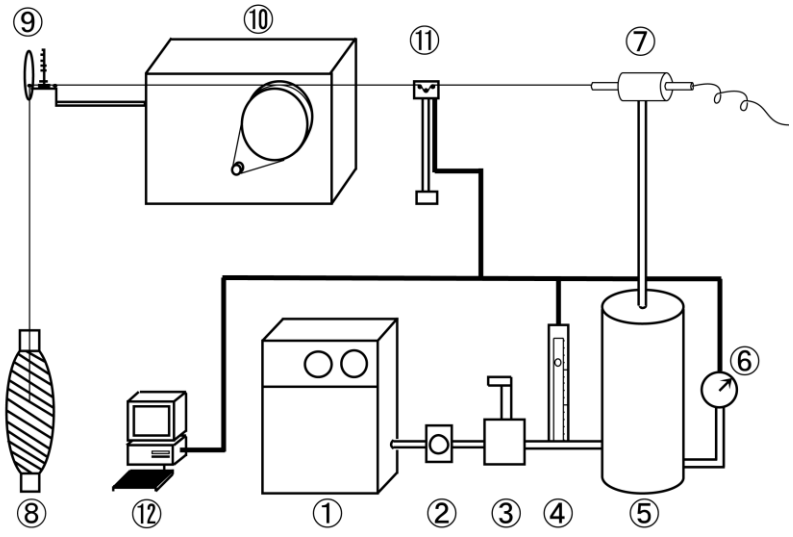

① Compressor
② Pressure adjuster
③ Valve
④ Flow meter
⑤ Rectification tank
⑥ Pressure gauge
⑦ Air suction gun
⑧ Yarn, Pirn
⑨ Tension adjuster
⑩ Speed adjuster (Feed roller)
⑪ Tension meter
⑫ Computer

Figure 1.1 Outline of the experimental apparatus

adjuster ⑨ and speed adjuster (feed roller) ⑩ respectively, and the yarn was then sucked into the yarn suction gun. Then the yarn suction force was measured by a tension meter ⑪ and these data were saved to a computer ⑫ connected to the tension meter.

Figure 2.2 shows the illustration of the yarn suction gun used in this study. It is mainly composed of yarn inhalation tube ①, nozzle including four compressed-air inflow tubes ②, and yarn propulsion tube consisting of de Laval tube ③ and straight tube ④. There are four compressed-air inflow tubes ② evenly spaced around the circumference of the nozzle, through which compressed air is introduced into the yarn passage. The axes of four compressed-air inflow tubes are in the planes parallel to *xz* and *yz* planes respectively, as shown in Fig. 2.2. Compressed air with both axial and circumferential directions of the yarn passage jets from the compressed-air inflow tubes ② to the yarn passage and passes through the yarn propulsion tube. A running yarn sucked from the entrance of the yarn inhalation tube with ambient air of the gun is given high propulsion in the yarn propulsion tube by the issued compressed air and blown out from the exit of the straight tube. The inner diameter of the yarn inhalation tube ① is 6 mm. The four compressed-air inflow tubes ② is 2 mm in diameter. The entrance and exit of the de Laval tube with a throat length of 2 mm are 15 mm in diameter. The inner diameter of the straight tube ④ is 20 mm. The focused geometrical parameters of the yarn suction gun are 1) compressed-air inflow angle of nozzle ϕ, 2) passage diverging angle of nozzle θ, 3) throat diameter of de Laval tube D, 4) converging angle of de Laval tube α, and 5) yarn propulsion tube length L. The values of each geometrical parameter are shown in Table 2.1.

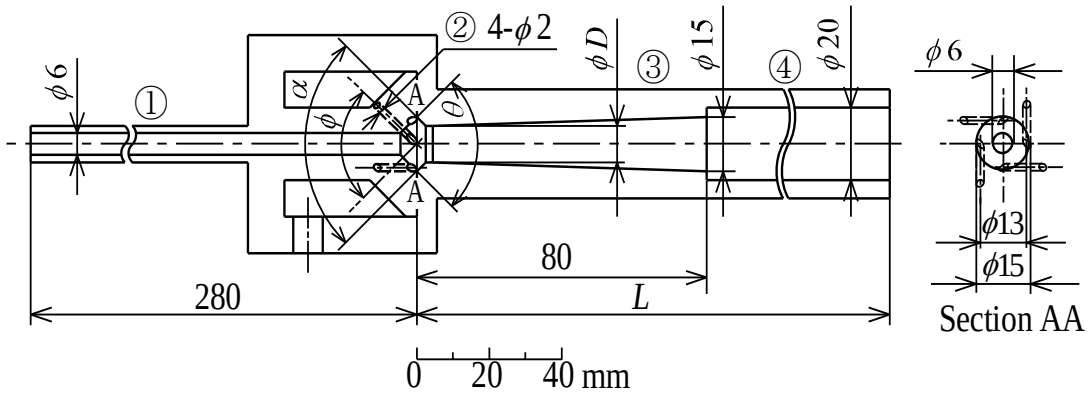

① yarn inhalation tube ② four compressed-air inflow tubes ③ de Laval tube ④ straight tube

Figure 2.2 Illustration of yarn suction gun (Yarn propulsion tube is composed of de Laval tube ③ and straight tube ④)

Table 2.1 Geometrical parameters of yarn suction gun

Geometrical parameter	Value
Compressed-air inflow angle of nozzle ϕ	30, 60, 90, 120, 150, 165°
Passage diverging angle of nozzle θ	30, 60, 90, 120°
Throat diameter of de Laval tube D	9, 10, 11, 12, 13, 14 mm
Converging angle of de Laval tube α	30, 60, 90, 120, 150°
Yarn propulsion tube length L	80, 200, 300, 400, 600, 800 mm

Other experimental conditions were yarn speed *v* and supplied air pressure *p*, i.e. the air pressure in the rectification tank. They were set up at v = 600 m/min and p = 0.5 MPa (gauge pressure) in each experiment to measure the yarn suction force and the mass flow rate for clarifying geometrical effects.

The tested yarn used in this experiment was polyester filament yarn of 167.7 dtex/48 f.

2.3 Results and Discussion

2.3.1 Time Dependency of Yarn Suction Force

Since the yarn suction force *F* showed oscillation against the passage of time *t*, its mean value F_m is discussed in this research. During the experiments, it was found that there are two types of time dependency of *F* under some of experimental conditions. An example of them is given in Fig. 2.3. The mean and amplitude of *F* in Fig. 2.3(a) are much different from those in Fig. 2.3(b). The case of small *F* is called Case 1 and the case of large *F* is called Case 2. The mean yarn suction force F_m is 228.8 mN and the standard deviation F_s is 17.5 mN in the Case 1, and F_m = 285.4 mN, F_s = 84.8 mN in the Case 2. F_m in the Case 2 is about 25 % larger than that in the Case 1.

The different time dependency of *F* appeared in the yarn after passing through the yarn suction gun. Figure 2.4 shows two photographs of the appearance of the yarn after passing through the gun under the same experimental conditions. Figures 2.4(a) and 2.4(b) correspond to Figs. 2.3(a) and 2.3(b), respectively. In the Case 2 of the large mean and amplitude of *F* in Fig. 2.3(b), knots appear in the yarn. They are not found in the Case 1 of small *F* (Fig. 2.3(a)).

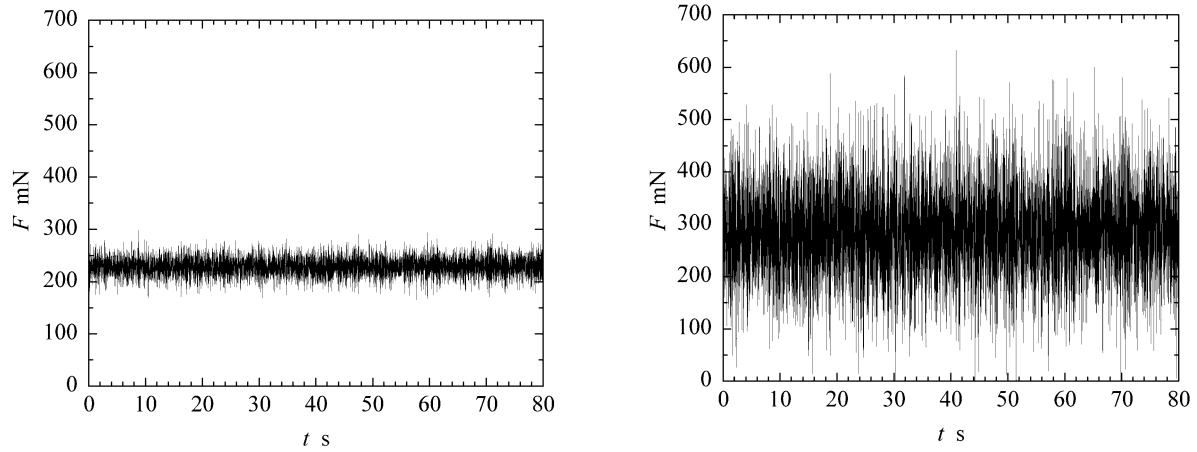

(a) Case 1: small suction force (b) Case 2: large suction force

Figure 2.3 Yarn suction force F as a function of measuring time t at the same experimental conditions of ϕ = 150°, θ = 90°, D = 10 mm, α = 90°, L = 300 mm, v = 600 m/min and p = 0.5 MPa.

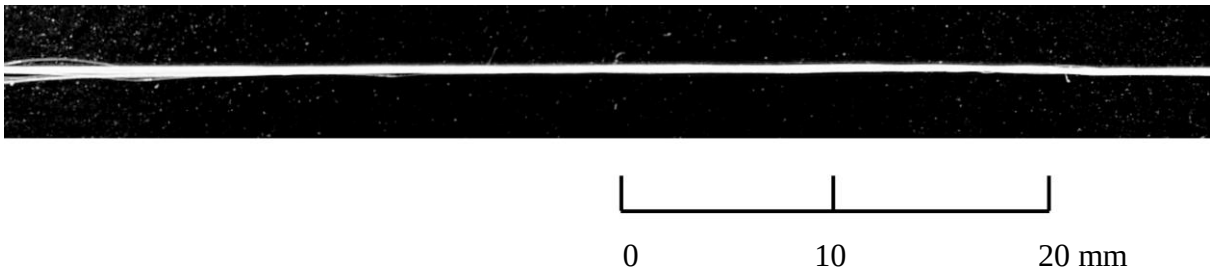

(a) Case 1: small suction force

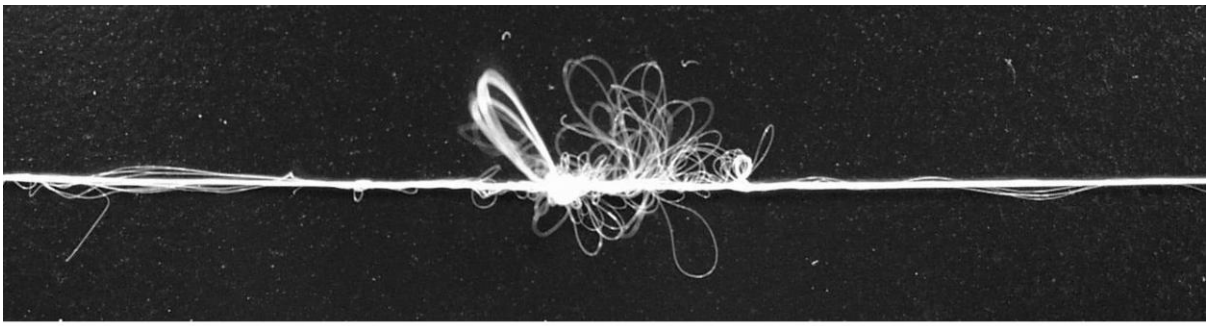

(b) Case 2: large suction force

Figure 2.4 Photographs of the yarn appearance after passing through the yarn suction gun at the same experimental conditions of ϕ = 150°, θ = 90°, D = 10 mm, α = 90°, L = 300 mm, v = 600 m/min and p = 0.5 MPa.

This phenomenon in the Case 2 frequently occurred in the case of large compressed-air inflow angle ϕ although the frequency of this occurrence depends on the geometry of the yarn suction gun and the experimental conditions. The jet of the compressed air is more vertical to the yarn axis at larger ϕ. In this case, the yarn is easier to be entangled, and then the knot gets formed more easily in the yarn after passing through the yarn suction gun [1, 2]. As a result, a large yarn suction force is produced because of the large pressure drag in addition to the frictional drag in the yarn running direction when the knots get formed in the running yarn. In addition, the dispersion of the yarn suction force becomes large because the knots are not regular and continuous in the running yarn and the airflow is very unsteady.

When F shows the two types of time dependency, we will use hereafter the smaller value of the Case 1 because the yarn suction characteristics of a yarn suction gun is represented by it.

2.3.2 Geometrical Effects of Yarn Suction Gun

Next, we will discuss the geometrical effects of a yarn suction gun on the yarn suction characteristics. In this section, we will discuss the effect of the geometrical parameters of the gun on the mean yarn suction force F_m and the air mass flow rate G. The experiments were performed at the yarn speed v = 600 m/min and the supplied air pressure p = 0.5 MPa (gauge pressure).

When we conduct the experiments to obtain the optimum values of the five geometrical parameters, the length of the yarn propulsion tube is expected to be desirable because the contact area between a running yarn and the high-speed air in the yarn propulsion tube should be kept wide so that the yarn suction force is large enough. However, the compact design of a yarn suction gun is also important because it is operated by a hand. Firstly we therefore set the yarn propulsion tube length L = 300 mm, with a total length of the gun of 580 mm.

To determine the optimum values of the four remaining parameters, experiments were carried out with a yarn propulsion tube of 300 mm in length. As a result, we obtained that the compressed-air inflow angle ϕ = 150°, the passage diverging angle of nozzle θ = 60°, the throat diameter of de Laval tube D = 10 mm, and the converging angle of de Laval tube α = 90° are the optimum geometrical parameters. The details will be presented in the following subsections.

All of experimental data are impossible to be presented here. As an example, Figure 2.5 shows isoplethic lines of the mean yarn suction force F_m and the air mass flow rate G as a

function of the compressed-air inflow angle ϕ and the passage diverging angle of nozzle θ. Other experimental conditions are the throat diameter of de Laval tube D = 10 mm, the converging angle of de Laval tube α = 90°, and the yarn propulsion tube length L = 300 mm. When θ is fixed, F_m increases with ϕ and takes the maximum at ϕ = 150°. Since the air flows with a circumferential component as well as an axial one in the yarn propulsion tube, a yarn may also run helically. Hence, as ϕ is increased, the helix pitch of the airflow becomes small; the length of the yarn in the yarn propulsion tube becomes long; frictional force between the air and yarn becomes large, and then F_m increases. For too large ϕ such as 165°, however, the circumferential component of airflow is too large, and then the propulsion is small. When ϕ is fixed, F_m attains the maximum in the range θ = 60 ~ 90° in the case of small ϕ of 30°; it is independent of θ in the case of ϕ = 60 ~ 90°, and decreases with an increase in θ in the case of ϕ exceeding 90°. However, the dependency of F_m on θ is much smaller than on ϕ. The air mass flow rate G is nearly constant although it seems to be the maximum near ϕ = 90°.

As another example, Figure 2.6 shows isoplethic lines of the mean yarn suction force F_m and the air mass flow rate G as a function of the throat diameter of de Laval tube D and converging angle of de Laval tube α. Other experimental conditions are fixed at the compressed-air inflow angle ϕ = 150°, the passage diverging angle of nozzle θ = 60°, and the yarn propulsion tube length L = 300 mm. When α is fixed, F_m reaches the maximum near D =

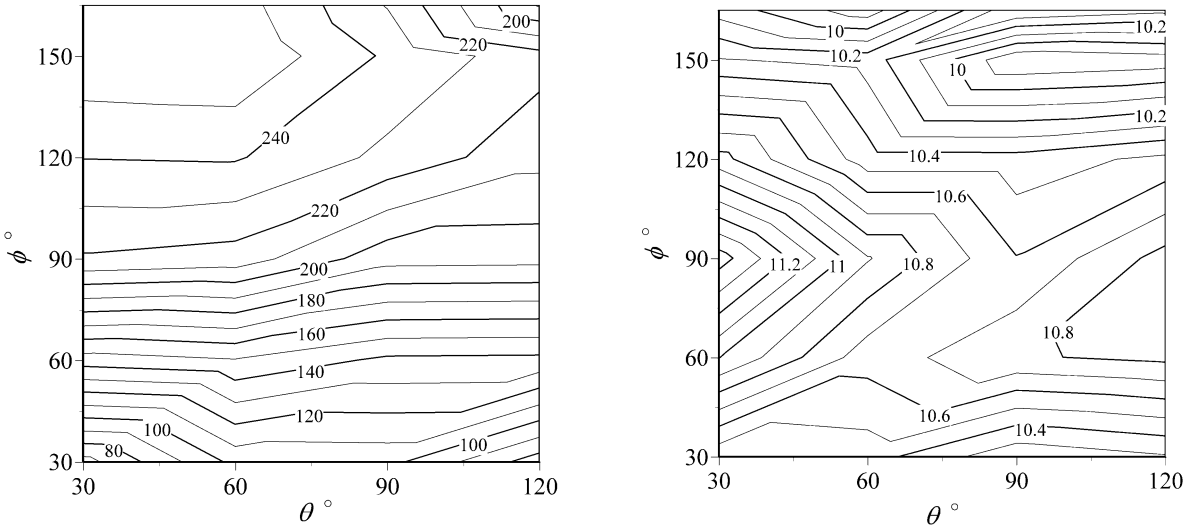

(a) Mean yarn suction force F_m [mN]

(b) Air mass flow rate G [g/s]

Figure 2.5 Effect of compressed-air inflow angle ϕ and passage diverging angle θ on the characteristics of yarn suction gun at D = 10 mm, α = 90°, L = 300 mm, v = 600 m/min and p = 0.5 MPa.

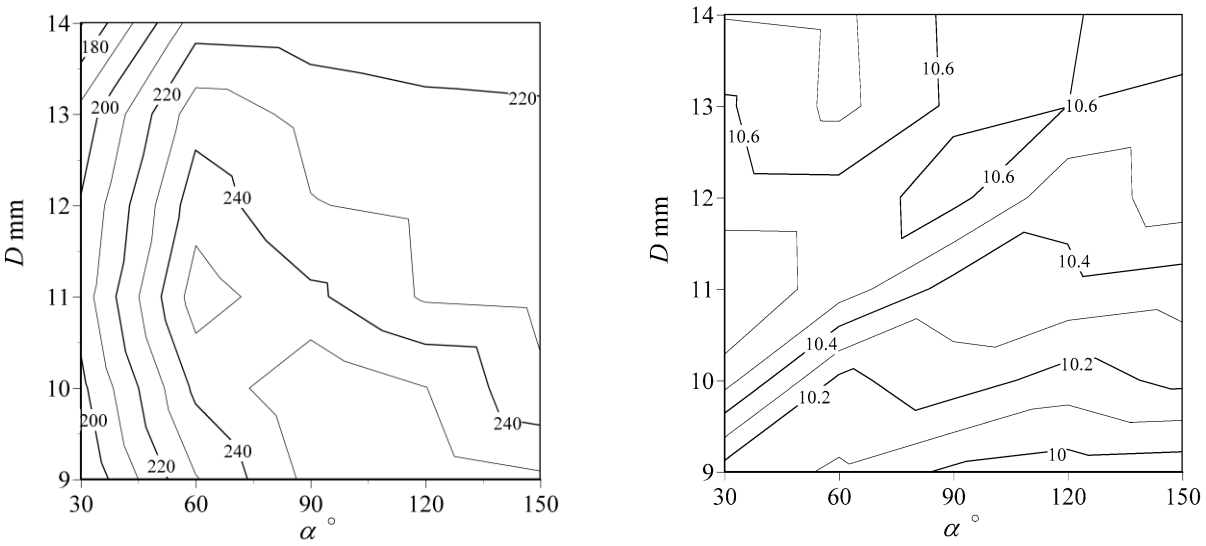

(a) Mean yarn suction force F_m [mN] (b) Air mass flow rate G [g/s]

Figure 2.6 Effect of throat diameter of de Laval tube D and converging angle of de Laval tube α on the characteristics of yarn suction gun at $\phi = 150°$, $\theta = 90°$, $L = 300$ mm, $v = 600$ m/min and $p = 0.5$ MPa.

10 mm. When D is fixed, F_m attains the maximum in the range of α from 60 to 90°. When α is fixed, G increases with D because of an increment of the cross-sectional area of flow region. The air mass flow rate G does not show a large dependency on α although it shows a little decrease with an increase in α. On the whole, G seems to reach the maximum near $\alpha = 60°$. The dependency of G on α is smaller than that on D.

Consumption of compressed air is proportional to the one of electricity. Producing a large yarn suction force F_m with a small amount of compressed air means high energy efficiency. The air mass flow rate G has a positive correlation with the consumption of compressed air. Therefore, the ratio of F_m to G can be used as an index to compare the yarn suction efficiency of yarn suction gun. In order to determine the optimum geometry of the yarn suction gun from the viewpoint of energy, the performance of the yarn suction gun is evaluated and compared by the ratio of F_m to G, named yarn suction efficiency denoted by η:

$$\eta = \frac{F_m}{G} \tag{1}$$

Therefore, the yarn suction gun with a high η is highly efficient from the viewpoint of energy. Figures 2.7 and 2.8 show isoplethic lines of the yarn suction efficiency η obtained from the data of Figs. 2.5 and 2.6.

Figure 2.7 shows the effect of the compressed-air inflow angle ϕ and passage diverging angle θ on the yarn suction efficiency η. When θ is fixed, η increases with ϕ and takes the maximum at ϕ = 150°. When ϕ is fixed, η attains the maximum near θ = 60° except in the case of small ϕ such as 30°. As a result, the optimum geometries of a yarn suction gun are ϕ = 150° and θ = 60° from the viewpoint of energy efficiency.

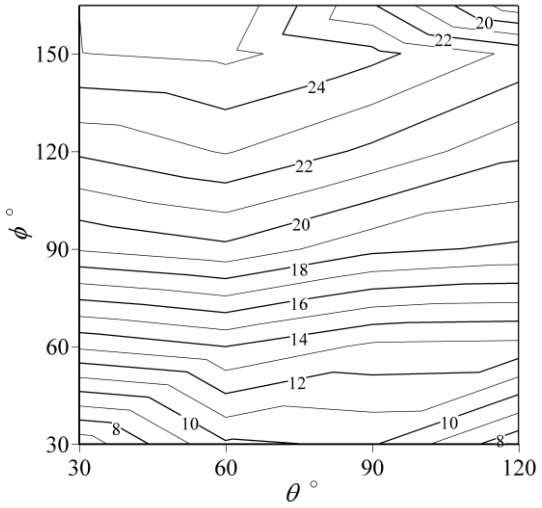

Figure 2.7 Effect of compressed-air inflow angle ϕ and passage diverging angle of nozzle θ on yarn suction efficiency η [N/(kg/s)] at D = 10 mm, α = 90°, L = 300 mm, v = 600 m/min and p = 0.5 MPa.

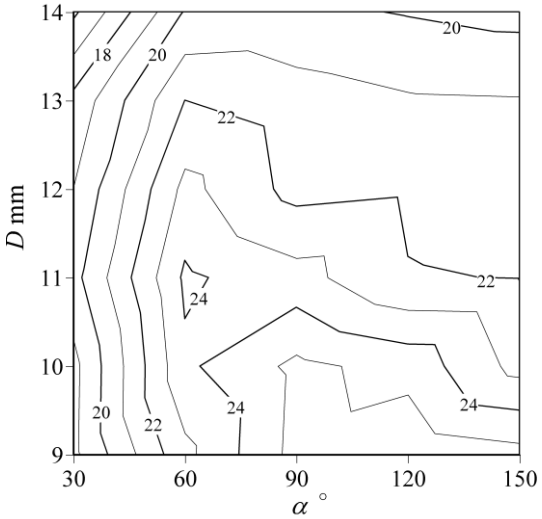

Figure 2.8 Effect of throat diameter of de Laval tube D and converging angle of de Laval tube α on yarn suction efficiency η [N/(kg/s)] at ϕ = 150°, θ = 60°, L = 300 mm, v = 600 m/min and p = 0.5 MPa.

Figure 2.8 shows the effect of the throat diameter of de Laval tube D and converging angle of de Laval tube α on the yarn suction efficiency η. When α is fixed, η takes the maximum near D = 11 mm for small α and near D = 10 mm for $\alpha > 75°$. When D is fixed, η attains the maximum in the α range from 60 to 90° and decreases a little with an increase in α for large α. As a result, the optimum geometries of a yarn suction gun are D = 10 mm and α = 90° from the viewpoint of energy efficiency.

From Figs. 2.5 ~ 2.8, η shows a distribution similar to F_m since G is hardly affected by the geometry of the yarn suction gun compared with F_m. This implies that it is possible to predict the tendency of η by using the measurement data of F_m.

We now obtained the optimum geometry of the yarn suction gun, which is the compressed-air inflow angle ϕ = 150°, the passage diverging angle of nozzle θ = 60°, the throat diameter of de Laval tube D = 10 mm and the converging angle of de Laval tube α = 90° when the yarn propulsion tube length L = 300 mm. Finally we will discuss the effect of the yarn propulsion tube length L on the yarn suction efficiency η. Figure 2.9 shows η as a function of L. The experiments were done at the running yarn speed v = 600 m/min and the supplied air pressure p = 0.5 MPa. As L increases, η increases to a maximum at L = 300 mm and then decreases. The dependency of η on L is comparatively small. Further details of the effect of L on η should be a future research topic.

The yarn suction force F increases with the length of the yarn in the airflow L_y. An increase in L will increase L_y so as to cause F to increase. However, F_m does not increase with L in the range L 〉 300 mm. It is a common practice that at the rear end of the straight tube is

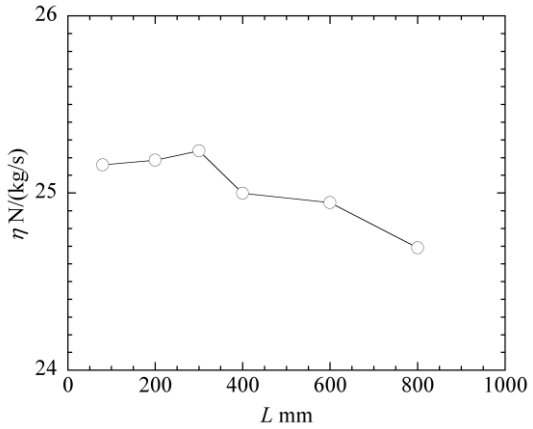

Figure 2.9 Yarn suction efficiency η as a function of yarn propulsion tube length L at ϕ = 150°, θ = 60°, D = 10 mm, α = 90°, v = 600 m/min and p = 0.5 MPa.

installed a hosepipe, a long tube reinforced with glass fiber, for discharging the entrained yarn into the waste yarn container. Therefore, the experiments will be carried out with the yarn suction gun with L = 300 mm thereafter because the experimental results at this condition are close to the real ones.

2.3.3 Proposal and Evaluation of Yarn Suction Gun with High Energy Efficiency

The geometry of the nozzle, de Laval tube and yarn propulsion tube constituting a yarn suction gun with high yarn suction efficiency was made clear from the experimental results as presented above. Table 2.2 shows the geometry of our proposing yarn suction gun with high yarn suction efficiency.

Table 2.2 Geometry of yarn suction gun with high efficiency. See detailed information on the geometrical parameters in Fig. 2.2.

Geometrical parameter	Value
Compressed-air inflow angle of nozzle ϕ	150°
Passage diverging angle of nozzle θ	60°
Throat diameter of de Laval tube D	10 mm
Converging angle of de Laval tube α	90°
Yarn propulsion tube length L	300 mm

2.4 Effect of Experimental Conditions on the Suction Characteristics of Yarn Suction Gun

Figures 2.10 and 2.11 show the mean yarn suction force F_m and yarn suction efficiency η of our proposing yarn suction gun as a function of the running yarn speed v at the supplied air pressures p = 0.4, 0.5 and 0.6 MPa. As shown in Fig. 2.10, when p is fixed, F_m decreases with an increase in v. This is because the air drag exerted on the yarn is small when the relative velocity of the air to the yarn is small. When p is high, F_m is large because of large air mass flow rate. η and F_m show a similar variation against v, as shown in Fig. 2.11. However, η in small v is higher at smaller p; the dependency of η on p decreases with an increase in v and vanishes completely at v = 1400 m/min.

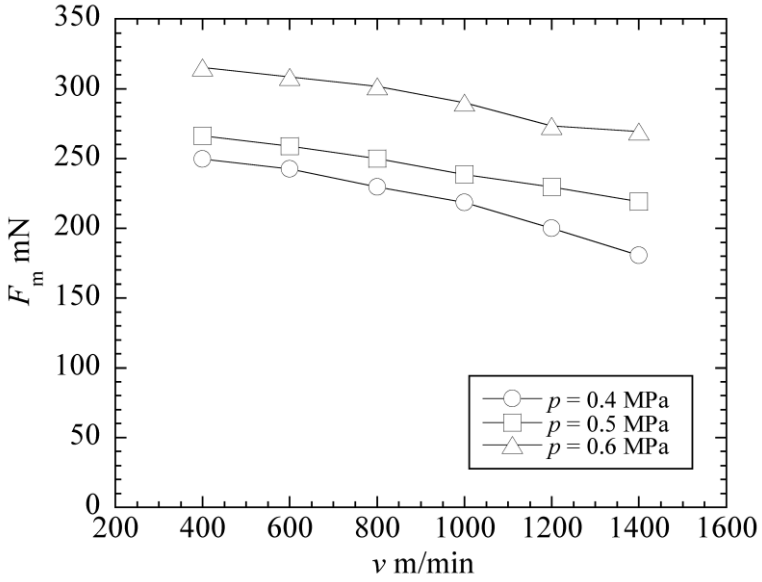

Figure 2.10 Mean yarn suction force F_m as a function of the yarn speed v at $\phi = 150°$, $\theta = 60°$, $D = 10$ mm, $\alpha = 90°$, $L = 300$ mm, and $p = 0.4$, 0.5 and 0.6 MPa.

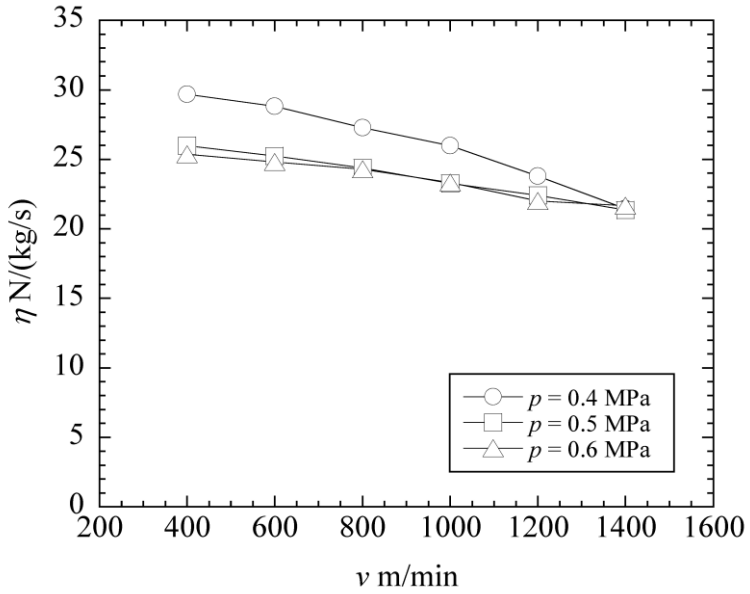

Figure 2.11 Yarn suction efficiency η as a function of the yarn speed v at $\phi = 150°$, $\theta = 60°$, $D = 10$ mm, $\alpha = 90°$, $L = 300$ mm, and $p = 0.4$, 0.5 and 0.6 MPa.

2.5 Conclusions

In this chapter we experimentally discussed the geometrical effect of a yarn suction gun on the characteristics of suction of running yarn. Results obtained are as follows:

(1) Yarn suction efficiency η, defined as the mean yarn suction force divided by the mass flow rate of compressed-air, is obviously affected by the converging angle of de Laval tube α and the throat diameter of de Laval tube D, especially it strongly depends on the compressed-air inflow angle ϕ. The passage diverging angle of nozzle θ has little effect on η. The optimum geometry of the yarn suction gun can be obtained from the point of view of energy efficiency.

(2) Increasing supplied air pressure raises yarn suction force F_m, but lowers η.

(3) F_m and η decreases with an increase in the speed of running yarn.

(4) There are two types of time dependency of the yarn motion and suction force even under the same experimental conditions.

For understanding the fundamental aspects of the yarn suction, working mechanism of the yarn suction gun will be analyzed in the following chapters.

References

[1] Chono S, Iemoto Y (1999) Study on interlaced yarn Part 7: Yarn motion and production mechanism of tangling part. *J Text Mach Soc Japan* (predecessor journal of *J Text Eng*), **45**, 108-112

[2] Iemoto Y (1997) Interlacing process of multiple filament yarns. *Japanese J of Multiphase Flow*, **11**, 23-29

Chapter 3

Numerical Simulation of Airflow Characteristics of a Yarn Suction Gun

List of Symbols

x, y, z	Cartesian coordinates
ϕ	Compressed-air inflow angle
θ	Passage diverging angle of nozzle
α	Converging angle of de Laval tube
D	Throat diameter of de Laval tube
ρ	Density of air
p	Static pressure of air
p'	Modified pressure
T	Static temperature
μ	Molecular (dynamic) viscosity
μ_t	Turbulent viscosity
μ_{eff}	Effective viscosity
h_{tot}	Specific total enthalpy
λ	Thermal conductivity
τ	Stress sensor
$\boldsymbol{S_M}$	Momentum source
$\boldsymbol{S_E}$	Energy source
k	Turbulent kinetic energy
ε	Rate of turbulence dissipation
C_μ, $C_{\varepsilon 1}$, $C_{\varepsilon 2}$	Turbulence model constant
σ_k, σ_ε	Turbulence model constant
P_k	Turbulence production
p_0	Supplied air pressure (absolute pressure of air in air tank)
T_0	Absolute temperature of air in air tank

ρ_0	Density of air in air tank
P^*	Absolute pressure of critical airflow
T^*	Absolute temperature of critical airflow
ρ^*	Density of critical airflow
R_g	Gas constant (for air R_g = 287)
k	Specific heat ratio = c_p/c_v [dimensionless] (for air k = 1.4)
c_p	Specific heat of gas at constant pressure
c_v	Specific heat of gas at constant volume
c	Sonic (acoustic) velocity
p_{in}	Absolute air pressure at entrance of compressed air inflow tube
T_{in}	Absolute temperature at entrance of compressed air inflow tube
v_{in}	Speed of air at entrance of compressed air inflow tube
p_{out}	Absolute pressure at outlet boundary of yarn suction gun
T_{out}	Temperature at outlet boundary of yarn suction gun
v_{out}	Air velocity at outlet boundary of yarn suction gun
p_a	Absolute pressure of the atmosphere
T_a	Temperature of the atmosphere
l_1	Lengths of outer region connected to yarn inhalation tube
l_2	Lengths of outer region connected to straight tube
R	Radius of straight tube
r	Radius of yarn inhalation tube
r_1	Radius of outer region connected to yarn inhalation tube
r_2	Radius of outer region connected to straight tube
v	Air velocity
v_z	Axial component of air velocity
v_c	Circumferential component of air velocity
v_y	Yarn feed speed
F_m	Suction force
C_f	Friction drag coefficient
L_y	Length of yarn in the airflow
d_y	Yarn apparent diameter

3.1 Introduction

A yarn suction gun is a kind of fluid machinery which sucks running yarns by both injection mechanism and friction between yarn surface and high-speed air. It is used for taking the running yarn to a winder at the beginning of yarn making and processing.

For designing the yarn suction gun with high performance using low energy, we have experimentally discussed effects of airflow geometries in a yarn suction gun on the suction characteristics of running yarn and obtained the optimum geometry from the viewpoint of energy efficiency, which is defined as the ratio of the yarn suction force to mass flow rate of supplied air, in Chapter 2. Yarn suction is a result of the interaction between high-speed airflow and yarn in a yarn passage. It is closely related to the airflow characteristics. A clear understanding of the airflow characteristics in the yarn suction gun is an important item for consideration of its performance. In the textile machinery subjects, several researchers have carried out actively researches on the characteristics of airflow in an interlacer in interlacing process [1-8], an air-jet nozzle in air-jet spinning or vortex spinning [9-12], an air-jet loom in weaving process [13-15], a yarn operation apparatus using both a circular jet and an angular jet [16]. However, the airflow in the yarn suction gun is different from those, and there is little literature on the study of the airflow.

It is difficult to measure the airflow patterns in the yarn suction gun experimentally because of very high speed of the airflow and limitation of operation space. Although some flow patterns can be directly measured by experimental method, it is impossible to know the flow patterns in detail, which prevents us to contact research deeply. A possibility of solving this problem is to use numerical simulation, a useful tool for investigating the flow patterns. The numerical simulation enables us to predict the performance of the prototype by figures of contour, vector, streamline, plot etc. and much more information can be obtained. Although the numerical simulation has many advantages, it cannot displace the experimental method completely because the simulated results are unbelievable if not verified by the experimental ones. Therefore, the simulated results will be verified by a few measurable experiments in this chapter.

The yarn suction gun is a fluid machinery sucking yarns using high-speed airflow. Therefore, the simulation of airflow in the yarn suction gun is based on CFD (Computational Calculation Fluid).

As for computational simulation method, four kinds of software packages FIDAP [4, 5], FLUENT [11, 17, 18], PHOENICS [10] and CFD-ACE+ have been commonly used. In this chapter the commercial software CFX 11.0 (ANSYS Inc.), which could show reasonable simulated results of the high-speed airflow pattern in the interlacer [6], is used for solving the governing equations. The method is a finite volume method.

In this chapter we investigate the characteristics of the airflow in a yarn suction gun with the optimum geometry obtained in Chapter 2 and the effects of supplied air pressure on the flow patterns by numerical simulation in order to understand the process of sucking yarn. The simulated results are verified by a few measurable experiments.

The primary purpose of simulating airflow in the yarn suction gun in this chapter is to explain the experimental results of yarn suction force F_m and yarn suction efficiency η obtained in Chapter 2 by using the simulated results, and then clarify the working mechanism of the gun.

Another purpose is to achieve a right and effective way to investigate the airflow patterns in the yarn suction gun using CFD.

It is a further purpose of this chapter to decide the appropriate operation condition by the simulated and experimental results.

3.2 Introduction to ANSYS CFX

ANSYS-CFX software is a commercial CFD program used to simulate fluid flow in a wide variety of applications, and delivers powerful CFD technology for simulations of all levels of complexity. It is a kind of software for analyzing thermal fluid using finite volume method and can be applied in resolving various engineering problems in various fluids, such as the fluid flow and thermal transition in general fluids. Moreover, ANSYS-CFX is an easy-to-use simulation software with good conservation property and high calculation accuracy, and has acquired a sound reputation for high product quality.

CFX consists of five parts: Workbench, CFX-Mesh, CFX-Pre, CFX-Solver, and CFX-Post. Figure 3.1 shows the working procedure of simulation by CFX.

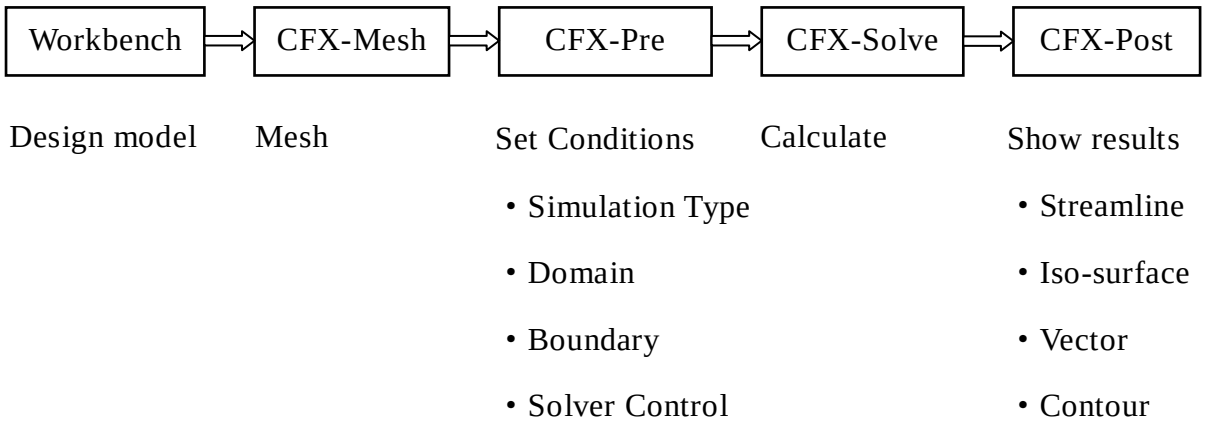

Figure 3.1 Working procedure of simulation by CFX.

3.3 Geometry and Size of Yarn Suction Gun

Figure 3.2 illustrates the yarn suction gun used in this study. It is mainly composed of yarn inhalation tube ①, nozzle including four compressed-air inflow tubes ②, and yarn propulsion tube consisting of de Laval tube ③ and straight tube ④. The working mechanism has been described in Chapter 2 and therefore its description is not given again here.

In this chapter we investigated the flow patterns of air in the yarn gun with compressed-air inflow angle ϕ = 150°, passage diverging angle of nozzle θ = 60°, converging angle of de Laval tube α = 90°, throat diameter of de Laval tube D = 10 mm,

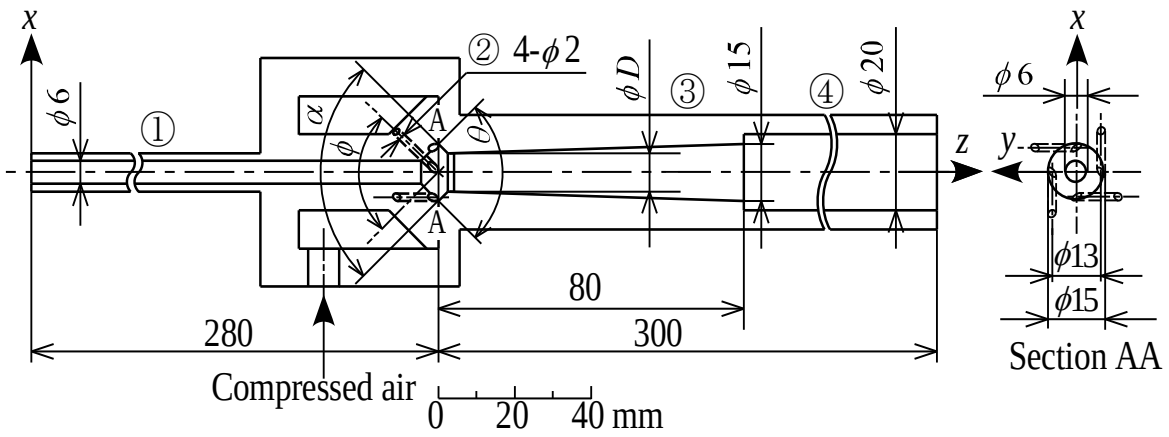

①Yarn inhalation tube ② Compressed-air inflow tube in nozzle ③ de Laval tube ④ Straight tube

Figure 3.2 Illustration of yarn suction gun.

propulsion tube length of 300mm and throat length of de Laval tube of 2 mm. This is because the largest suction efficiency can be obtained using the gun with above geometric parameters, as presented in Chapter 1.

Cartesian coordinate system was used to represent positions in the yarn suction gun. The origin of this coordinate system is located at the center of the entrance of yarn inhalation tube. *z* axis is the coordinate on the centerline of the gun and *xy* plane is perpendicular to the *z* axis.

3.4 Numerical Simulation

Numerical simulation was carried out under the condition without a yarn in the yarn passage because yarn apparent diameter is much smaller than the size of the yarn passage.

3.4.1 Geometry of Airflow

Figure 3.3 shows the three-dimensional computation regions composed of the yarn inhalation tube, nozzle with four compressed-air inflow tubes, de Laval tube, straight tube and two outside air regions. The two outside air regions were set to compute accurately the airflow patterns near the entrance of the yarn inhalation tube and the exit of the straight tube. Their size will be discussed in more detail in Sec. 3.4.8.

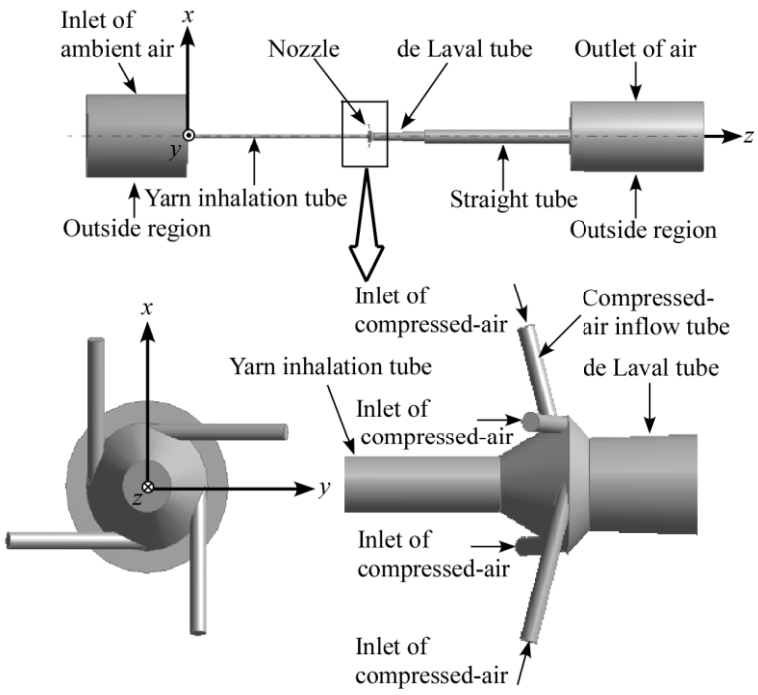

Figure 3.3 Computation regions for airflow simulation.

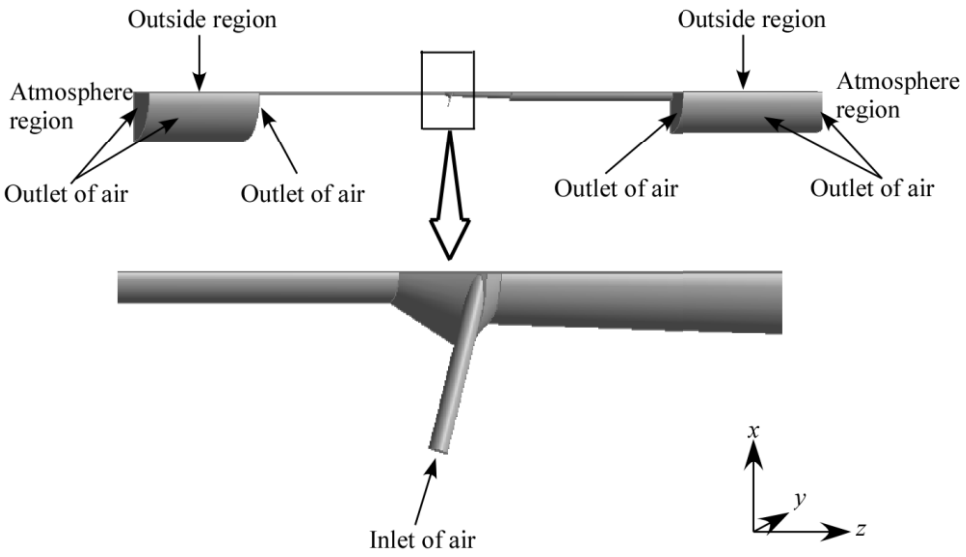

Figure 3.4 Computation regions in the simulation.

For shortening calculating time, the computation was done in a quarter of the computation regions in the circumferential direction as shown in Fig. 3.4 and periodic boundary conditions were set for periodic boundaries. The positions of inlet and outlet boundary are also shown in this figure.

3.4.2 Basic Assumption

For simplifying the modeling of airflow, air was treated as an ideal gas with viscosity. The governing equations under consideration were three-dimensional unsteady compressible Navier-Stokes equations. The equations of mass, momentum and energy conservation can be written as follows:

The continuity equation:

$$\frac{\partial \rho}{\partial t} + \nabla \bullet (\rho \boldsymbol{U}) = 0 \tag{3.1}$$

The momentum equation:

$$\frac{\partial \rho \boldsymbol{U}}{\partial t} + \nabla \bullet (\rho \boldsymbol{U} \otimes \boldsymbol{U}) - \nabla \bullet (\mu_{eff} \nabla \boldsymbol{U}) = -\nabla p' + \nabla \bullet (\mu_{eff} \nabla \boldsymbol{U})^T + \boldsymbol{B} \tag{3.2}$$

The total energy equation:

$$\frac{\partial (\rho h_{tot})}{\partial t} - \frac{\partial p}{\partial t} + \nabla \bullet (\rho \boldsymbol{U} h_{tot}) = \nabla \bullet (\lambda \nabla T) + \nabla \bullet (\boldsymbol{U} \bullet \tau) + \boldsymbol{U} \bullet \boldsymbol{S}_{\boldsymbol{M}} + \boldsymbol{S}_{\boldsymbol{E}} \tag{3.3}$$

where ρ is the density, $\boldsymbol{U}$ represents the velocity vector, p the static pressure, μ_{ff} the effective viscosity, p' the modified pressure, T the static temperature, $\boldsymbol{B}$ the sum of body

forces, h_{tot} the specific total enthalpy, λ the thermal conductivity, τ the stress tensor, $\boldsymbol{S_M}$ the momentum source, and $\boldsymbol{S_E}$ is the energy source.

The k-ε model was employed as a turbulence model for stable calculation of high-speed airflow because a characteristic Reynolds number of 2.6×10^5 is obtained roughly from the flow in the exit of de Laval tube as shown in Section 3.5, which is in the range of turbulent flow (above 2.3×10^3) in pipe flow. Turbulence was approximated using a classical k-ε model. k is turbulence kinetic energy and is defined as the variance of the fluctuation in velocity; ε is the turbulence dissipation rate (the rate at which the velocity fluctuations dissipate). The turbulent kinetic energy k and the turbulence dissipation rate ε are given by:

$$\frac{\partial(\rho k)}{\partial t} + \nabla \bullet (\rho \boldsymbol{U} k) = \nabla \bullet \left[\left(\mu + \frac{\mu_t}{\sigma_k} \right) \nabla k \right] + P_k - \rho\varepsilon \tag{3.4}$$

$$\frac{\partial(\rho \varepsilon)}{\partial t} + \nabla \bullet (\rho \boldsymbol{U} \varepsilon) = \nabla \bullet \left[\left(\mu + \frac{\mu_t}{\sigma_\varepsilon} \right) \nabla \varepsilon \right] + \frac{\varepsilon}{k} (C_{\varepsilon 1} P_k - C_{\varepsilon 2} \rho\varepsilon) \tag{3.5}$$

Where C_μ, $C_{\varepsilon 1}$, $C_{\varepsilon 2}$, σ_k and σ_ε are constants; P_k is the turbulence production due to viscous and buoyancy forces; μ the molecular (dynamic) viscosity; μ_t the turbulence viscosity.

In this research we used the k-ε model for the simulation of airflow. This model, one of the most prominent models, has been implemented in most general CFD codes and is considered the industrial standard model. It has proven to be stable and numerically robust and has a well established regime of predictive capability. For general simulations, the model offers a good compromise in terms of accuracy and robustness. The k-ε model has been used in the literatures [5, 10, 12, 15] listed in this chapter and many literatures which are not shown here.

The air travels through the yarn suction gun at high speed so that there is almost no time for any heat transfer. As a result, the flow was assumed as adiabatic and therefore the wall boundary was set as adiabatic and no-slip condition.

3.4.3 Inlet Boundary Conditions

As shown in Fig. 3.5, the compressed-air inflow tubes are assumed to be connected to a large volume reservoir of highly compressed air where absolute pressure is p_0 and absolute temperature is T_0 = 293 K.

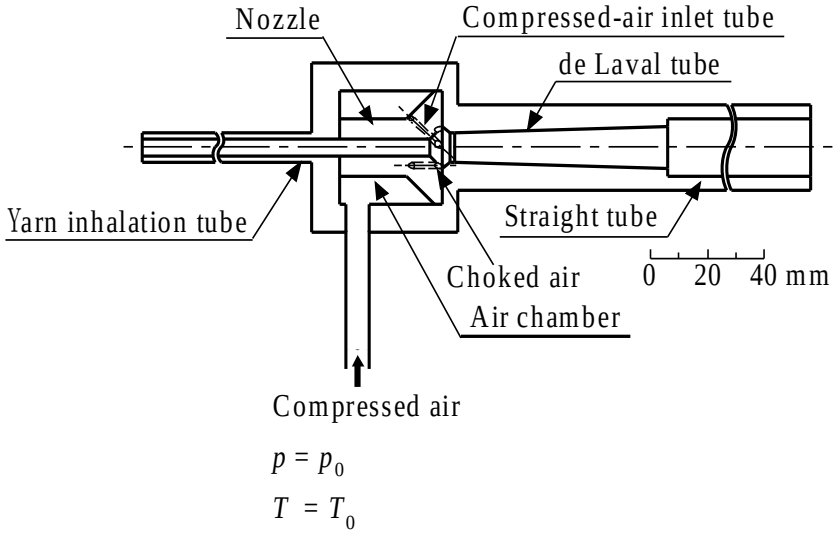

Figure 3.5 Illustration of air choke positon.

The airflow passage from the air chamber to the yarn passage through the compressed-air inflow tube is like a converging-diverging nozzle. Suppose that we gradually reduce the back pressure (pressure drop in the yarn passage) while the pressure in the air chamber remains constant. In such a case, the velocity of air in the compressed-air inflow tube increases until the limiting sonic velocity is reached. Namely, if there is a large enough pressure differential between the air chamber and the yarn passage, sonic velocity (the Mach number M = 1) will occur at a position in the compressed-air inflow tube. The flow at this point is called critical flow. At this time, i.e. M = 1, we obtain [19]

$$\frac{T^*}{T_0} = \frac{2}{k+1} = 0.833 \tag{3.6}$$

$$\frac{p^*}{p_0} = \left(\frac{2}{k+1}\right)^{k/(k-1)} = 0.528 \tag{3.7}$$

$$\frac{\rho^*}{\rho_0} = \left(\frac{2}{k+1}\right)^{k/(k-1)} = 0.634 \tag{3.8}$$

$$k = \frac{c_p}{c_v} = 1.4 \tag{3.9}$$

$$c^2 = kR_g T^* \tag{3.10}$$

Where the asterisks (*) identify critical properties

the subscript zeros ($_0$) identify air properties in air chamber (air tank)

T = absolute temperature in degrees Kelvin, K

p = absolute pressure, Pa

ρ = density, kg/m^3

R_g = a gas constant, m^2/ (s^2·K) (for air R = 287)

k = specific heat ratio = c_p/c_v [dimensionless] (for air k = 1.4)

$c_{p=}$ specific heat of gas at constant pressure, N•m/(kg•K)

$c_{v=}$ specific heat of gas at constant volume, N•m/(kg•K)

c = the sonic (acoustic) velocity, m/s

Hence a choked flow at the entrances of the compressed-air inflow tubes was employed as inflow boundary conditions of the compressed air. For example, when p_0 = 0.6013 MPa and T_0 = 293 K, using Eqs. (3.6), (3.7) and (3.10) we can determine the inlet boundary conditions:

$p_{in} = p_0 \times 0.528 \approx 0.3175$ MPa

$T_{in} = T_0 \times 0.833 \approx 244.1$ K

$$v_{in} = \sqrt{kR_gT_{in}} = \sqrt{1.4\times 287\times 244} = 313.1 \text{ m/s}$$

where p_{in}, T_{in} and v_{in} are the absolute pressure, absolute temperature and speed of air at the entrances of the compressed-air inflow tubes respectively.

The inlet boundary conditions for the simulations are shown in Table 3.1.

Table 3.1 Inlet boundary conditions

Compressed-air in reservoir			**Inlet boundary conditions**		
P_0, MPa	T_0, K	v_0, m/s	P_{in}, MPa	T_{in}, K	v_{in}, m/s
0.5013	293	0	0.2647	244	313.1
0.6013			0.3175		
0.7013			0.3703		

3.4.4 Outlet Boundary Conditions

Outflow conditions were imposed on the outside boundaries of the two outside air regions shown in Fig. 3.4. They were considered to be at normal temperature and atmospheric pressure. Therefore the atmosphere around the outside boundary is at an absolute pressure p_a of 0.1013 MPa and an absolute temperature of 293 K.

3.4.5 Initial Conditions

A steady-state calculation will typically require between 50 and 100 outer loop iterations to achieve convergence. If we expect that the actual flow being simulated would take a long time to reach a steady-state condition, then a greater number of outer loop iterations may be required. In this case, we can usually reduce the number of iterations required by setting initial conditions that more closely resemble the steady state flow.

In this research, the domain initial conditions were created according to a normal atmosphere with static steady and normal temperature, namely, with an absolute pressure of $p_{initial}$ = 0.1013 MPa, a temperature of $T_{initial}$ = 293K, a velocity along *x*-axis $U_{initail}$ = 0 m/s, a velocity along *y*-axis $V_{initial}$ = 0 m/s, and a velocity along *z*-axis $W_{initial}$ = 0 m/s.

3.4.6 Computation and Convergence

The residual is a measure of the local imbalance of each conservative control volume equation. It is the most important measure of convergence as it relates directly to whether the equations have been solved. ANSYS CFX presents the normalized residuals to judge convergence. A normalized residual of roughly 1^{-6} to 1^{-7} is always approaching machine round off (and therefore the computational limit of convergence) on a 32 bit (single precision) machine.

CFX-Solver will stop calculating when it reaches the set target RMS (Residual of Root Mean Square). The RMS is obtained by taking all of the residuals throughout the domain, squaring them, taking the mean, and then taking the square root of the mean. Considering RSM = 1^{-6} is approaching the computational limit of convergence and often not possible to achieve this level, the target RSM = 10^{-5} was set in the research.

3.4.7 Mesh

ANSYS CFX software uses a unique hybrid finite-element (finite-volume) approach to discretize Navier-Stokes equations. In this method, values are calculated at discrete places on a meshed geometry. The mesh influences the accuracy, convergence and speed of the solution. More importantly, the time it takes to create a mesh model is often a significant portion of the time it takes to get results from a CFX solution. A high quality mesh increases the accuracy of the CFD solution and improves convergence relative to a poor quality mesh. Coarse mesh leads to inaccurate result, whereas too fine mesh results in excessive time of calculation.

For investigating the effects of mesh quality on the simulated results, we performed the simulation of airflow in the yarn suction gun with ϕ = 150°, θ = 60°, α = 90°, D = 10 mm when the supplied air pressure p_0 is 0.6013 MPa. Thus an inlet boundary condition with p_{in} = 0.3175 MPa, T_{in} = 244.1 K and v_{in} = 313.1 m/s was created at the inlet of the compressed-air inflow tube.

The radial distribution of air velocity v in zx plane in five cross-sections of the yarn suction gun in Fig. 3.6 was used to examine the effect of mesh refinement and size of outside region on the simulated results.

The solution error decreases as the mesh is refined and appears to disappear when the number of total mesh element is 2,000,294, as shown in Fig. 3.7. The results of the numerical analysis do not change much if the element mesh is further refined. By considering the calculation accuracy, computation time and hardware requirement The mesh parameters in the case of No. ⑪ were selected as the reference one for discussing the effect of the sizes of the two outside calculation regions on the simulated results.

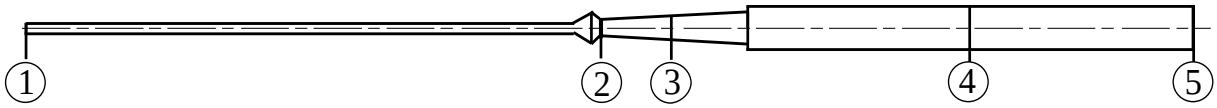

① Entrance of yarn inhalation tube (z = 0 mm)

② Throat of de Laval tube (z = 284.5 mm)

③ Middle section of de Laval tube (z = 320 mm)

④ Middle section of straight tube (z = 470 mm)

⑤ Exit of straight tube (z = 580 mm)

Figure 3.6 Position for examining the effect of mesh refinement on the simulated results.

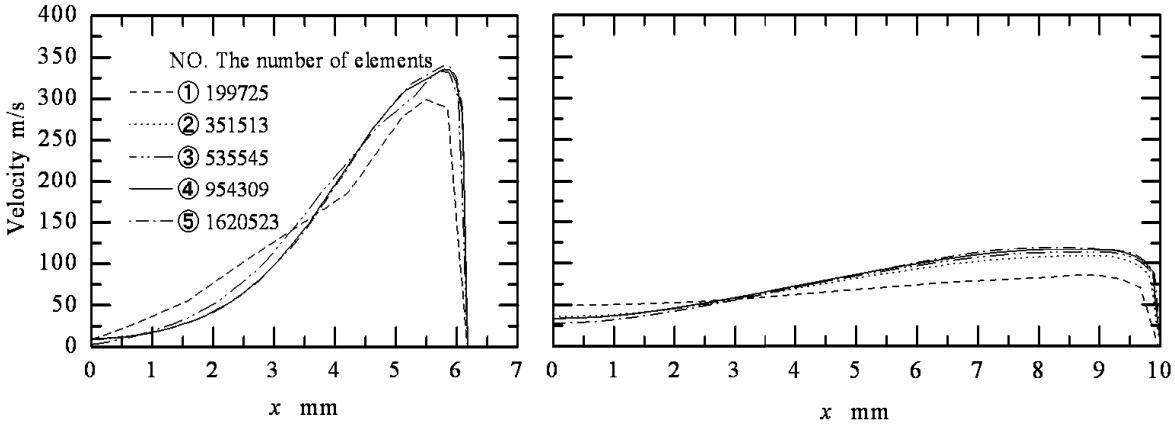

Middle section of de Laval tube (z = 320 mm) | Middle section of straight tube (z = 470 mm)

(a) Refine the whole region

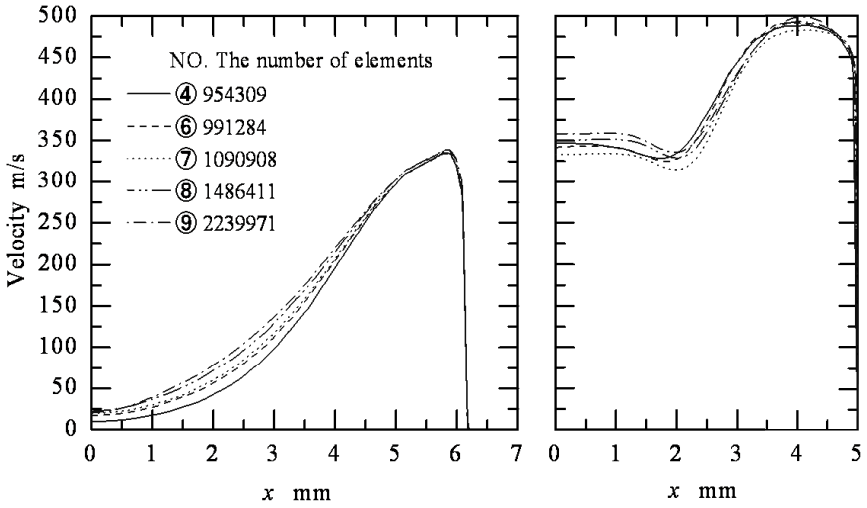

Middle section of de Laval tube (z = 320 mm) | Section of throat (z = 284.5 mm)

(b) Refine regions of nozzle and throat

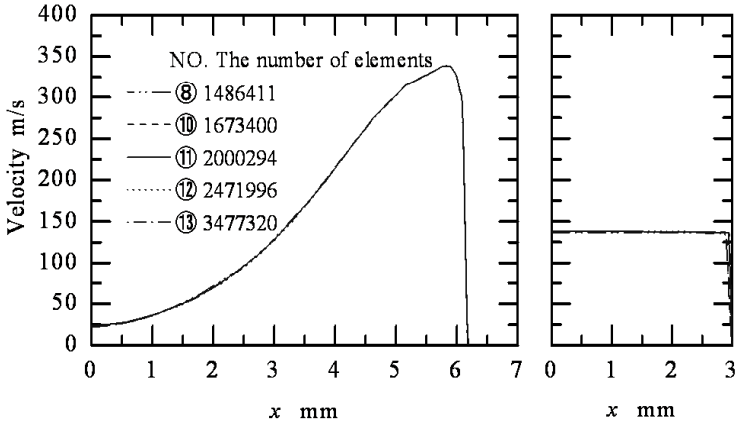

Middle section of de Laval tube (z = 320 mm) | Entrance of yarn inhalation tube (z = 0 mm)

(c) Refine yarn inhalation tube

Figrue 3.7 Effect of mesh refinement on the simulated results.

3.4.8 Discussion on the Size of Outside Regions

The size of two outside calculation regions (Fig. 3.8) may have some effects on the simulated results. We simulated the airflow in the yarn suction gun with the outside regions in different size. The inlet boundary condition with an absolute pressure of p_{in} = 0.3175 MPa, a temperature of T_{in} = 244.1 K and a flow velocity v_{in} = 313.1 m/s was created at the inlet of the compressed-air inflow tube. Radius and length of the outer regions (r_1, l_1, r_2 and l_2) were chosen as the multiples of the radii of the yarn inhalation tube and the straight tube (r and R) respectively. Figure 3.9 shows the results of the size of two outside regions on the simulated results.

We set the limit number of mesh element in each a quarter of the yarn suction gun about 2800000 according to the accuracy and the computation capacity of the computer. As a result, the radius (r_1) and the length (l_2) of the outer region connected to the yarn inhalation tube were decided to be twenty times (60 mm) and fifty times (150 mm) as large as the radius of the yarn inhalation tube r (= 3 mm) respectively. Likewise, the radius (r_2) and the length (l_2) of the outer region connected to straight tube were decided to be five times (50 mm) and twenty times (200 mm) as large as the radius of the straight tube R (= 10 mm) respectively.

The tetrahedral computational meshes used in this computation are shown in Fig. 3.10. This mesh system was selected after the detailed mesh refinement exercises as mentioned above, and the number of total elements is 2,720,390.

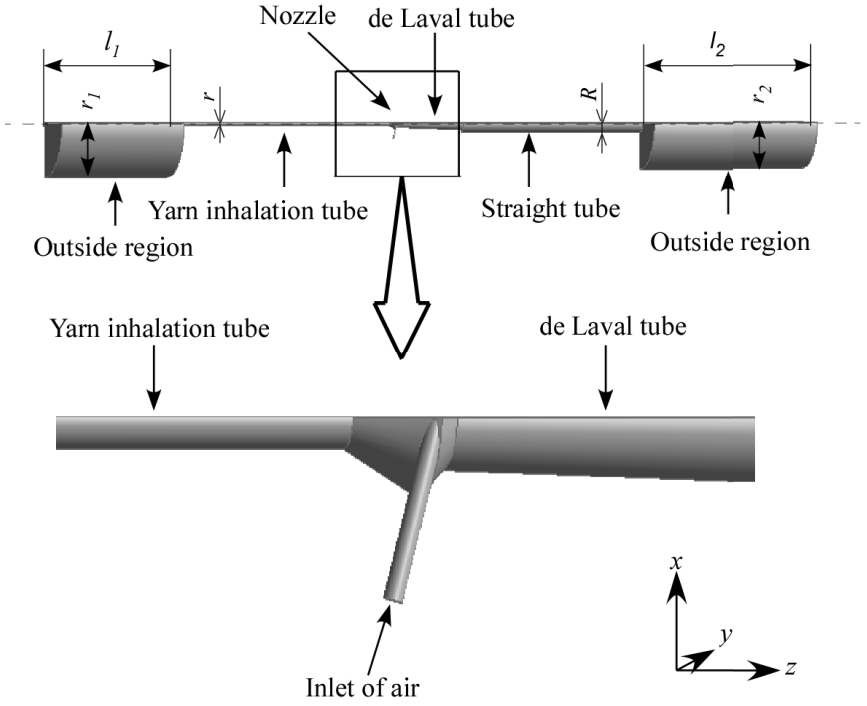

Figure 3.8 Size of the outside calculation regions.

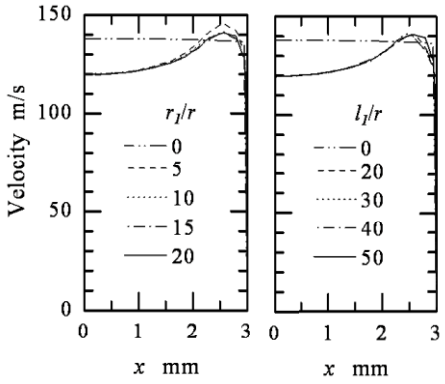

Radial distribution of air velocity in the entrance of yarn inhalation tube (z = 0 mm)

(a) Effect of the size of outside region connected to yarn inhalation tube on the simulated results

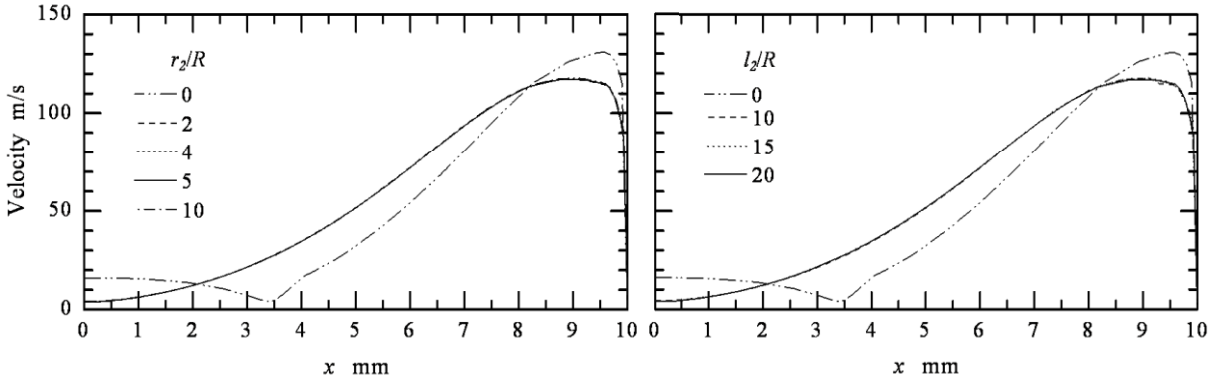

Radial distribution of air velocity in the exit of straight tube (z = 580 mm)

(b) Effect of the size of outside region connected to straight tube on the simulated results

Figure 3.9 Effect of outside calculation region size on the simulated results.

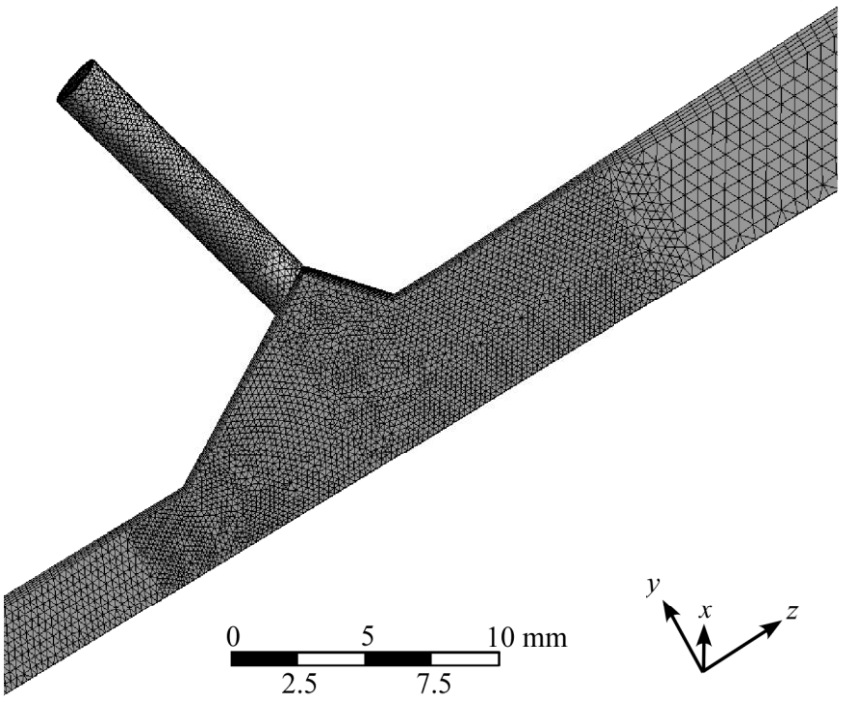

Figure 3.10 Three-dimensional view of the generated meshes in and near the nozzle.

3.4.9 Computer Performance and Calculation Time

Computer used for simulation has one CPU (Pentium 4, 3.8 GHz) and 3.5 GB RAM. The time needed for each simulation is decided by not only the performance of the computer but also the number of mesh elements, quality of the mesh, the boundary conditions and solver control set. Taking the yarn suction gun with the optimum geometry as an example, the geometry used for simulation is a quarter of the original. The geometry has 2,720,390 mesh elements. When the supplied air pressure p_0 = 0.6013 MPa, it required 51 h to converge the simulation.

3.5 Measurement of Wall Pressure

As shown in Fig. 3.11, thirty-three measuring holes of 0.8 mm in diameter were drilled in the *xz* longitudinal section of the yarn propulsion tube to measure static pressure on its inner wall. The description of the route of air from a compressor to the gun is omitted because it is the same as that in the previous research in Chapter 2. When the pressure was measured at a hole, the other holes were plugged.

The air pressure was measured with a strain gauge type pressure transducer under the condition without a yarn in the gun.

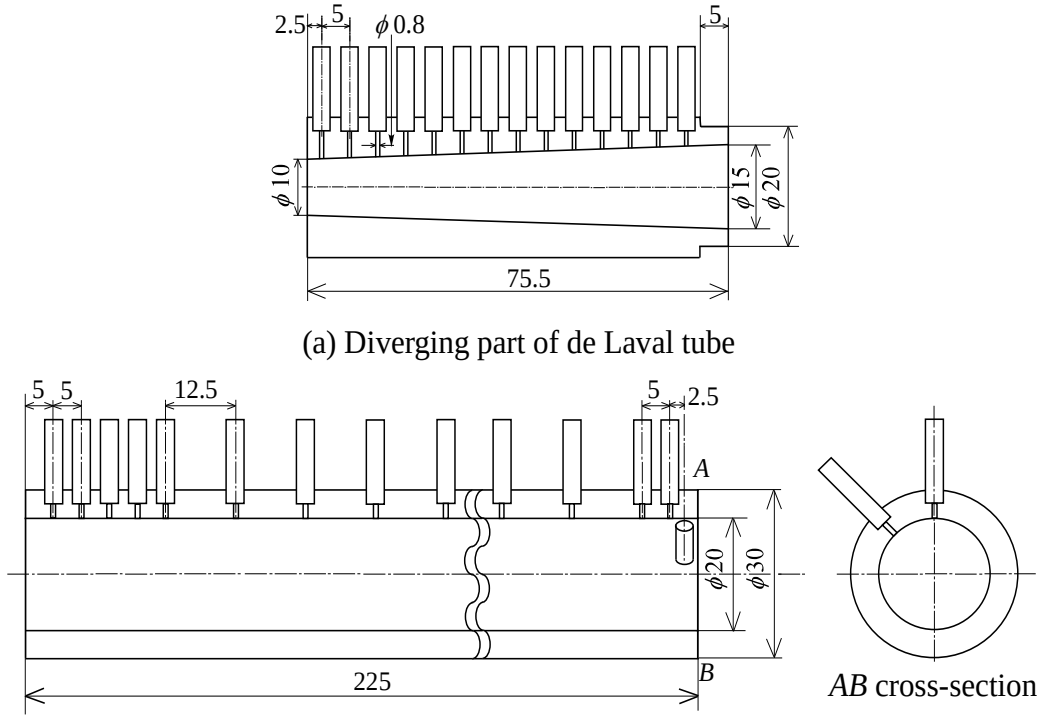

(a) Diverging part of de Laval tube

(b) Straight tube

Figure 3.11 Configuration and dimension of holes for measurement of pressure (unit: mm).

3.6 Results and Discussion

3.6.1 Airflow Characteristics of Yarn Suction Gun at Supplied Air Absolute Pressure of 0.6013 MPa

Firstly, we investigate the airflow patterns in the yarn suction gun at supplied air absolute pressure p_0 = 0.6013 MPa. At this pressure, i.e. gauge pressure of 0.5 MPa, yarn suction force and mass flow rate were measured in each experiment for clarifying geometrical effects in the Chapter 2. Therefore, the present simulation was done at p_0 = 0.6013 MPa for the sake of comparability with the previous study.

CFD can help us to understand flow patterns by visualizing simulated results. The absolute pressure contour in *xz* plane of the yarn suction gun is shown in Fig. 3.12. Figure 3.13 shows pressure distributions in *z* direction on the inner wall in the *xz* plane and on the centerline of the gun. The left ordinate shows the non-dimensional local absolute pressure *p* divided by the atmospheric pressure p_a of 0.1013 MPa. The right ordinate is wall position x_w to show the shape of yarn passage. In addition, the line of p/p_a = 1 is shown as the reference.

According to the simulated result, the region of an intense negative pressure, which causes the driving force for sucking the ambient air into the yarn inhalation tube, is located from the vicinity of the throat (*z* = 284.5 mm) of the de Laval tube to the position where *z* = 300 mm. The throat of the de Laval tube is called the throat hereafter. The pressure distributes uniformly in the radial direction in the yarn inhalation tube. It is higher near the wall than near the centerline in the yarn propulsion tube.

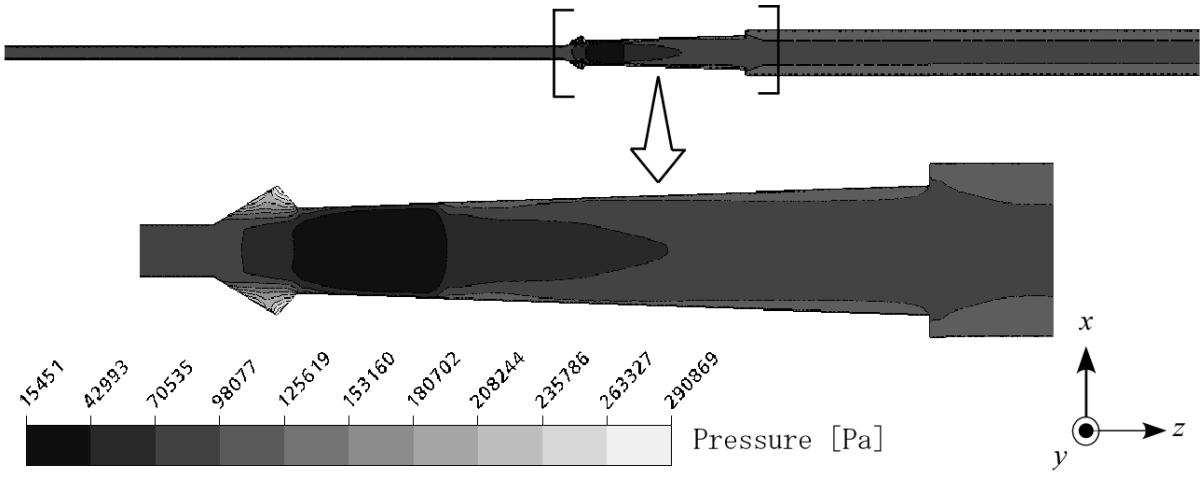

Figure 3.12 Contour map of pressure in *xz* plane (p_0 = 0.6013 MPa).

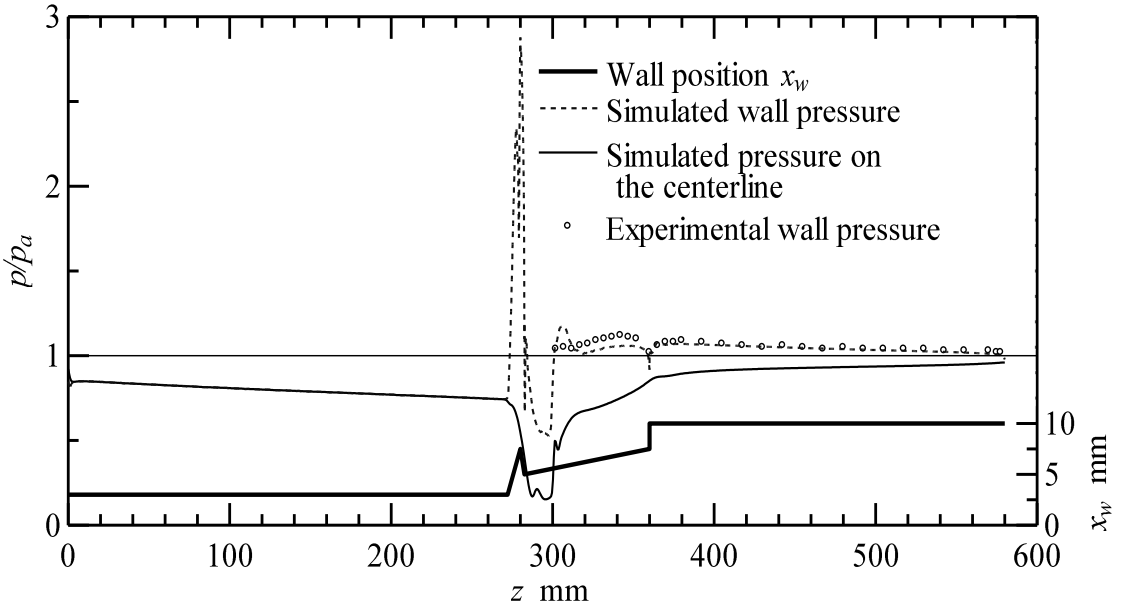

Figure 3.13 Simulated and experimental pressure distributions on the wall in the *xz* plane and on the centerline at p_0 = 0.6013 MPa, and shape of yarn passage.

The wall pressure distribution shows a sharp rise at the exits of the compressed-air inflow tubes and then a rapid drop due to both expansion wave near the exit and flow acceleration in the convergent part of the de Laval tube. The flow which reaches a critical state near the throat becomes supersonic in the divergent part of the de Laval tube, and the pressure decreases furthermore. However, since a normal shock wave occurs on the way (z = 300 mm) of the divergent part, the pressure is increased and a subsonic flow is generated. The pressure increases gradually with flow cross-sectional area. The wall pressure drops suddenly at a sudden enlargement part located at the entrance of the straight tube (z = 360 mm) because of decrement of circumferential velocity component due to conservation of angular momentum and decrement of centrifugal force. Then, it decreases gradually with an increase in distance from the entrance and finally attains the atmospheric pressure at the exit (z = 580 mm).

The ambient air sucked through the yarn inhalation tube flows near the centerline of the yarn propulsion tube and has lower pressure than that near the wall. The pressure on the centerline keeps decreasing from the nozzle to the position of the normal shock wave. Then, it rapidly rises owing to the generation of the shock wave, and gradually rises to the atmospheric pressure.

As shown in Fig. 3.13, the simulated wall pressure presents variations less than 11% around the experimental value which are in the expected range; especially both of

them in the yarn propulsion tube are in good agreement. However, the accuracy is not high in the region where shock wave occurs. The thickness of normal shock wave is wide and the overshoot of pressure is seen. On the whole, the present simulation provides the reasonable results.

The flow pattern varies according to cross-sections parallel to the *xy* plane in the yarn suction gun. Therefore, we select ten of them for research as shown in Fig. 3.14. Figure 3.15 shows the absolute pressure contours at the nine sections. There is no pressure distribution at sections ① and ② in the yarn inhalation tube, as shown also in Fig. 3.15. The maximum pressure is located at the four exits (section ④) of compressed-air inflow tubes. There is a spatially large vacuum core, where air pressure and density are extremely low, in the de Laval tube. The result of density distribution will be shown later. The pressure is biased and very high near the wall around the vacuum core. It implies that the helical flow produced by the yarn suction gun has a higher focusing ability for sucking a yarn. The vacuum core in the straight tube becomes small gradually. The pressure becomes axisymmetric with respect to the centerline in the downstream region from the middle (z = 320 mm) of the de Laval tube.

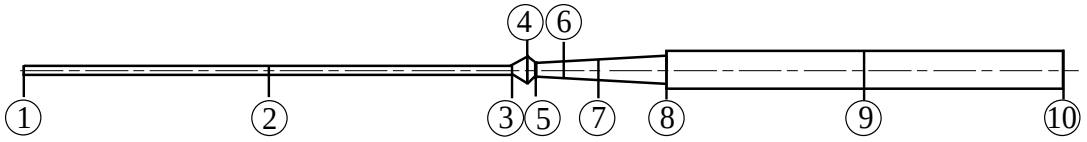

① Entrance of yarn inhalation tube (z = 0 mm)

② Middle section of yarn inhalation tube (z = 140 mm)

③ Entrance of passage diverging area (z = 272 mm)

④ Entrance of de Laval tube (z = 280 mm)

⑤ Throat of de Laval tube (z = 284.5 mm)

⑥ Position of normal shock wave (z = 300 mm)

⑦ Middle section of de Laval tube (z = 320 mm)

⑧ Entrance of straight tube (z = 360 mm)

⑨ Middle section of straight tube (z = 470 mm)

⑩ Exit of straight tube (z = 580 mm)

Figure 3.14 Selected cross-sections.

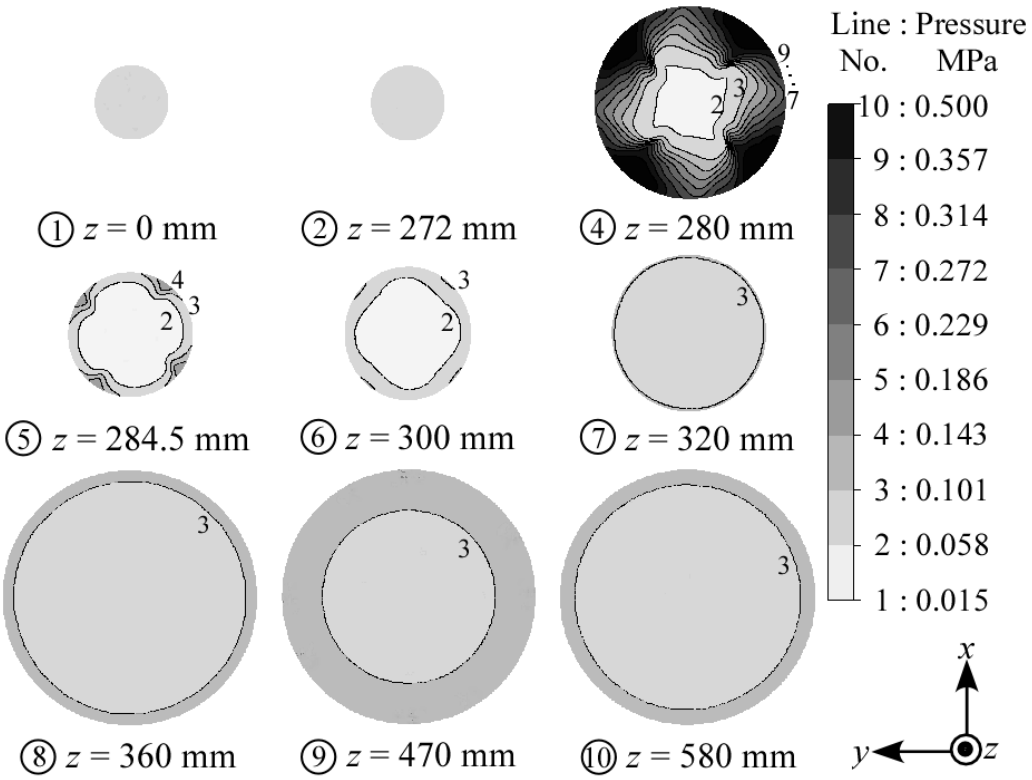

Figure 3.15 Pressure contours at the cross-sections at p_0 = 0.6013 MPa.

Figure 3.16 shows air density distributions in *z* direction on the inner wall in *xz* plane and on the centerline of the yarn suction gun. The density distribution is very similar to the pressure one shown in Fig. 3.13. The density near the wall is higher than that near the centerline in the yarn propulsion tube, and the flow is biased toward the vicinity of the wall.

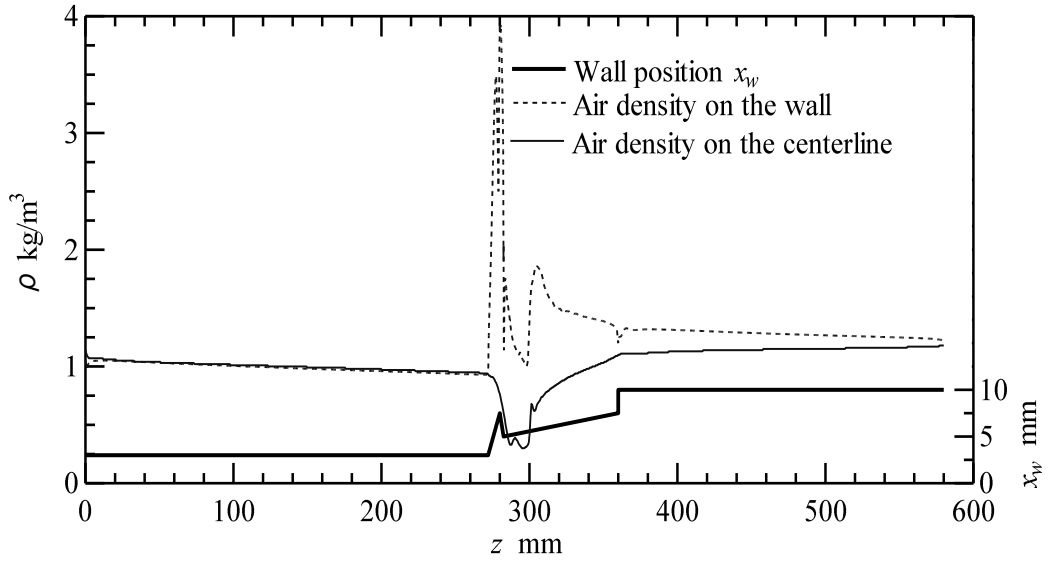

Figure 3.16 Simulated air density distributions on the wall in the *xz* plane and on the centerline at p_0 = 0.6013 MPa.

The density ρ of a gas depends on the absolute pressure p and absolute temperature T of the gas; the relationship between these properties is closely defined by the perfect (ideal) gas law [19]:

$$\rho = \frac{p}{R_g T} \tag{3.11}$$

For a prefect gas undergoing an isentropic process, pressure p is related to density by

$$p = C\rho^k \tag{3.12}$$

where C is dimensionless coefficient. Therefore, air density distribution pattern is similar to that of pressure distribution, as shown in Figs 3.13 and 3.16.

Figure 3.17 shows the absolute values of velocity in and near the nozzle and de Laval tube. The contour is in *xy* plane. Figure 3.18 shows the velocity vectors in and near the nozzle and de Laval tube. Arrows represent the direction and magnitude of air velocity. A large arrow denotes a large velocity. As shown in these figures, a high-speed airflow in a helix is generated in the yarn propulsion tube. The air issued from the compressed-air inflow tubes, which is supersonic, accelerates in the converging part of the de Laval tube, and keeps accelerating in the diverging part. However, a normal shock wave occurs near z = 300 mm and then the pressure suddenly rises and the subsonic flow is generated. As the subsonic flow proceeds downstream in the yarn propulsion tube, it decelerates owing to the enlargement of passage, mixing with the sucked ambient air and friction of tube wall. The sucked ambient air is entrained by the issued compressed air, accelerates toward the de Laval tube from the yarn inhalation tube, and decreases owing to the decrease of the velocity near the wall.

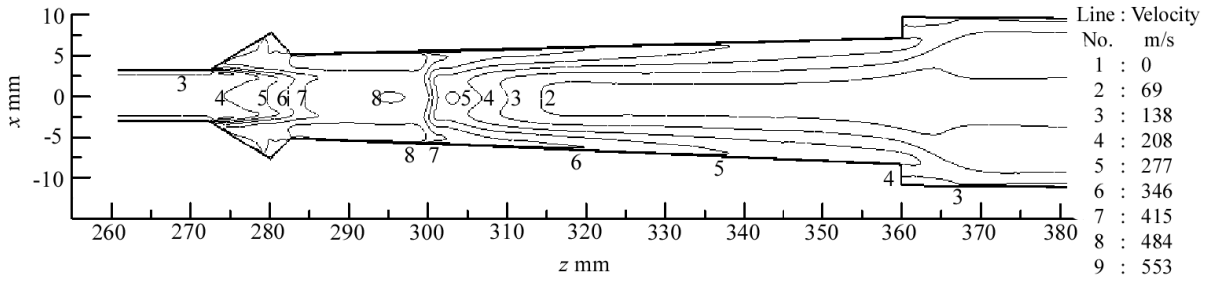

Figure 3.17 Contours of absolute value of velocity in the *xz* plane at p_0 = 0.6013 MPa.

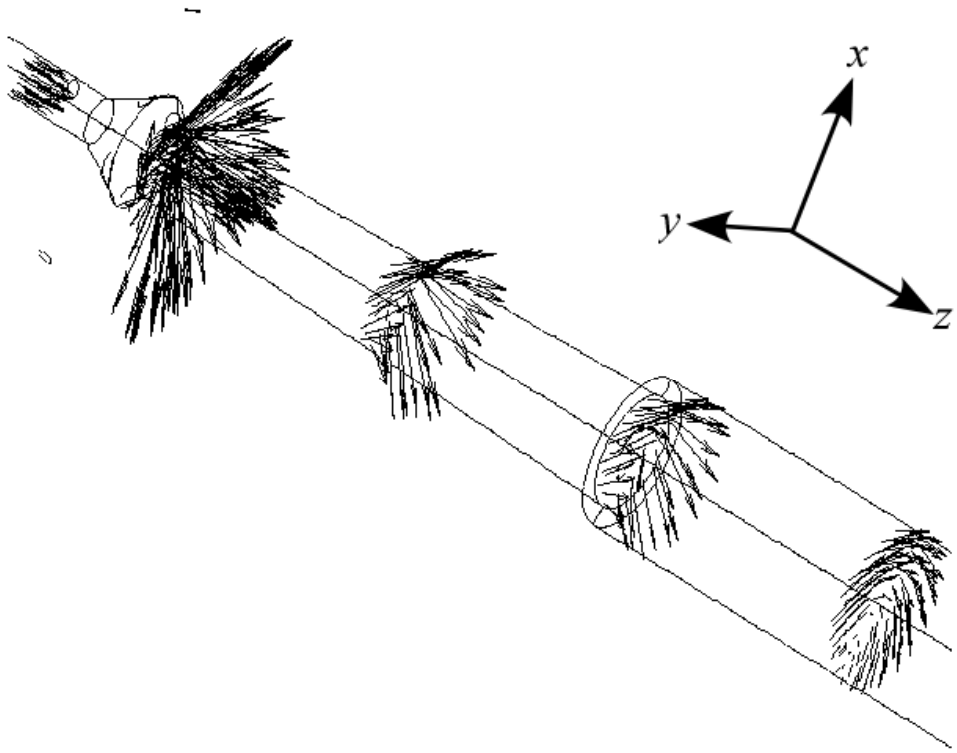

Figure 3.18 Three-dimensional view of velocity vectors in and near the nozzle and the de Laval tube at p_0 = 0.6013 MPa.

Figure 3.19 shows radial distributions of axial velocity component v_z and circumferential velocity component v_c at the cross-sections illustrated in Fig. 3.14. It is characterized by the circumferential velocity v_c and axial velocity v_z. Although the flow has radial, axial and circumferential velocity components, the radial velocity component is omitted because it is very small compared with v_z and v_c.

As shown in Fig. 3.19(a), v_c is close to zero and the air flows without pre-rotation only in the axial direction in the yarn inhalation tube. This is also shown in Fig. 3.18. When a yarn is sucked into the yarn propulsion tube, it is strongly propelled by high-speed helical airflow. However, since the airflow through the yarn inhalation tube sucks a yarn to the yarn propulsion tube, it has a substantial effect on the performance of the yarn suction gun at the beginning of yarn sucking operation. This flow rate depends on the pressure difference at both ends of the yarn inhalation tube, that is, the negative pressure in the vacuum core.

As shown in Fig. 3.19(b), the airflow in the converging part of the de Laval tube has great axial and circumferential velocity components. The air having the two velocity components issued from the compressed-air inflow tubes flows along the inner wall of

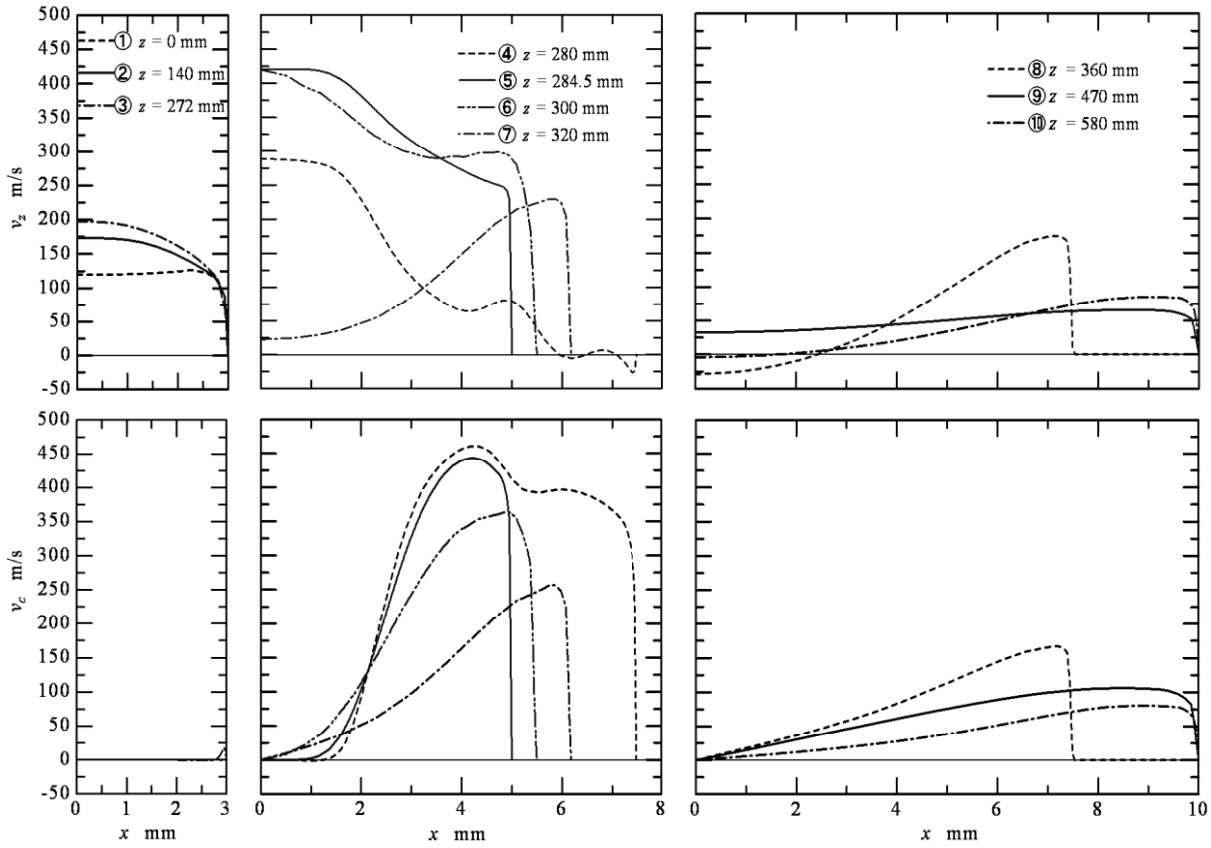

(a) Yarn inhalation tube (b) de Laval tube (c) Straight tube

Figure 3.19 Radial distributions of axial velocity component v_z and circumferential one v_c at various cross-sections at p_0 = 0.6013 MPa.

the converging part owing to a centrifugal force and develops into high-speed helical flow. v_z and v_c near the wall at the throat (section ⑤ : z = 284.5 mm) are larger than those at the entrance (section ④ : z = 280 mm) of the de Laval tube, respectively. v_z and v_c increase with z, i.e. a decrease in the tube diameter. It can be explained according to mass conservation and angular momentum conservation although variation in density will also influence the velocity. The angular momentum of a moving particle is

$$L = mv_c r \tag{3.13}$$

where m is its mass, v_c is the circumferential velocity, and r is its radial distance from the axis. Therefore, v_c varies inversely as r. The speed and rate of rotation of the airflow decrease progressively with distance from the center. Thus, v_c increases as the radius of tube is decreased. v_z increases when the tube narrows because the mass flow rate is constant. Therefore, the converging part of the de Laval tube is designed to accelerate the helical flow.

v_z near the wall in the diverging part just after the throat increases to a supersonic value. However, this velocity is rapidly brought again to subsonic level by the normal shock wave generated near z = 300 mm. The subsonic speed decreases with an increase in z, i.e. enlargement of flow passage, owing to mass conservation, angular momentum conservation and mixing with the sucked ambient air. v_z near the centerline in the diverging part just after the throat rapidly increases to a supersonic value near 500 m/s. The air pressure and density near the centerline are close to zero in the region of z = 285-300 mm as shown in Figs. 3.13 and 3.16. Then, v_z and v_c decrease owing to the generation of the normal shock wave. The sucked air develops into a helical flow. The diverging part of the de Laval tube is a yarn propulsion region where the yarn develops into a helical motion.

As shown in Fig. 3.19(c), the airflow still maintains the helical motion in the straight tube although the speed of helical flow decreases with an increase in z. The vortex core exhibits a dip in the axial velocity or even reverse flow. Air is sucked near the centerline at the exit of the straight tube, that is, reverse flow occurs.

Figure 3.20 shows the Mach number in and near the nozzle and de Laval tube. The contour is in xy plane. The compressed air issued from the four compressed-air inflow tubes flows along the wall at high Mach number up to 2.2. The air sucked through the yarn inhalation tube accelerates and attains sonic speed (Mach number of unity) at the throat. The generation of the normal shock wave is confirmed because the Mach number rapidly drops near z = 300 mm although the Mach number is not uniform in the radial direction at the cross-section of the yarn passage. The Mach number is confirmed to be larger near the wall than near the centerline.

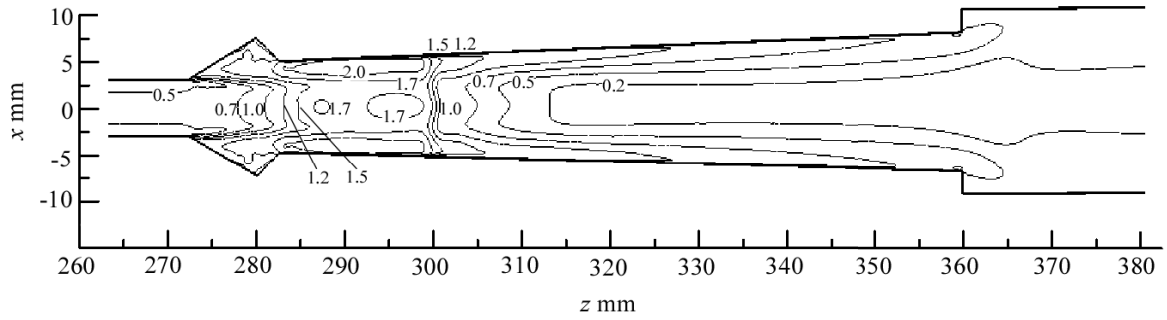

Figure 3.20 Contours of Mach number in the xz plane at p_0 = 0.6013 MPa.

Figure 3.21 shows the streamlines of airflow in the yarn suction gun. One is a streamline through the centerline of the compressed-air inflow tube and another is a streamline through a point (x, y, z) = (1 mm, 0 mm, 0 mm). The issued compressed air forms a conical helix with a varying radius in the de Laval tube. The sucked air shows a straight streamline parallel to the centerline in the yarn inhalation tube. After entering the de Laval tube, the flow is gradually changed to a helical flow with smaller helical diameters than that of the compressed air. The issued compressed air and the sucked ambient air mix together in the yarn propulsion tube.

From the airflow characteristics obtained by the numerical simulation, we can get a basic understanding of yarn motion in the yarn suction gun. Because of the propulsion force created by the friction between the air and yarn surface, a yarn is sucked into the yarn inhalation tube, moved forward by the sucked ambient air, developed into helical motion owing to the rotation of the issued compressed air in the yarn propulsion tube, and finally discharged into the atmosphere with the issued compressed air and the sucked ambient air together.

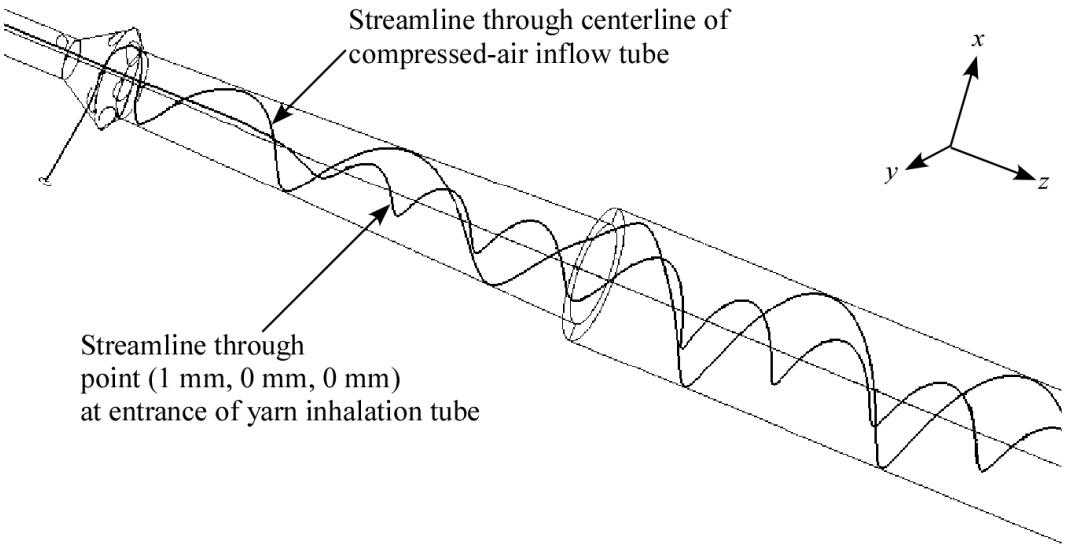

Figure 3.21 Three-dimensional view of streamlines in and near the nozzle and de Laval tube at p_0 = 0.6013 MPa.

3.6.2 Relation between Yarn Suction Performance and Airflow Characteristics

When we assume that a yarn is on a streamline of airflow, the entraining of yarn occurs by virtue of the surface friction between the yarn and high-speed airflow. Here gravity and pressure drag do not enter the problem because the friction drag would be more amenable to a theoretical approach than pressure drag [19]. Yarn suction force F_m, i.e., frictional force between the yarn and air, can be represented by the following equation:

$$F_m = C_f \frac{\rho}{2}(v - v_y)^2 \cdot \pi d_y L_y \tag{3.14}$$

where C_f is frictional drag coefficient, ρ air density, v airflow speed, v_y yarn speed, d_y yarn apparent diameter and L_y length of yarn in the airflow. Thus, the yarn suction force F_m exerted on a yarn running at the same speed will depend on v, ρ and L_y.

When being supplied with the compressed air, the yarn suction gun produces a helical airflow rotating cyclonically in the yarn propulsion tube with high speed and density near the wall. The high speed rotation of airflow causes the sucked yarn to run in the helical airflow, also in a helical motion. Therefore, a strong frictional force is exerted on the sucked yarn owing to large v and ρ according to Eq. (3.14). This high focusing ability greatly promotes the suction efficiency.

L_y is another major factor involved in the yarn suction force. This helical motion of airflow causes L_y to increase greatly because a contact area between air and a yarn is larger in a helix than in a straight line. From Eq. (3.14), a larger F_m is produced owing to a larger L_y. This implies that the yarn should be made to run near the wall of the yarn propulsion tube.

The present yarn suction gun is characterized by a high-speed helical flow, which exerts a strong suction force on the yarn because of a high suction efficiency generated by high air velocity, large air density and wide contact area.

From observation above, we get a basic understanding of working mechanism of the present yarn suction gun. When being supplied with compressed air, the yarn suction gun produces a helical airflow in passage direction with high speed and large air density near the wall. A running yarn is sucked into the gun due to the intense low pressure caused by the high speed of helical airflow. The airflow rapid rotation causes the yarn to run in the helical airflow. Thus, the contact length or area between the yarn and the air increases greatly. The friction force between the yarn and the air increases greatly due to the high air velocity, large air density and contact area. As a result, a high suction efficiency is produced.

3.6.3 Effect of Supplied Air Pressure on the Airflow Pattern

Simulated results of airflow in the yarn suction gun at various supplied air pressures p_0 (absolute pressure) are discussed in the following. We keep both geometrical parameters and boundary conditions except for p_0 constant, varying p_0 from 0.5013 MPa to 0.7013 MPa.

Figure 3.22 shows the simulated static pressure on the wall in the *xz* plane and on the centerline. The pressure in the yarn inhalation tube ($z \leqq 272$ mm) rises with an increase in p_0. This causes a decrease in the sucked air velocity in the yarn inhalation tube, which decreases the yarn suction force. However, magnitude of negative pressure generated from the vicinity of the throat becomes large with p_0. Also, the area of negative pressure presents the same trend because the position of the normal shock wave is shifted downstream.

In the straight tube, both the positive pressure on the wall and the absolute value of the negative pressure on the centerline increase with p_0. However, the changes of them are indistinctive. Therefore, the change of p_0 mainly influences the air velocity distributions in the yarn inhalation tube and the de Laval tube.

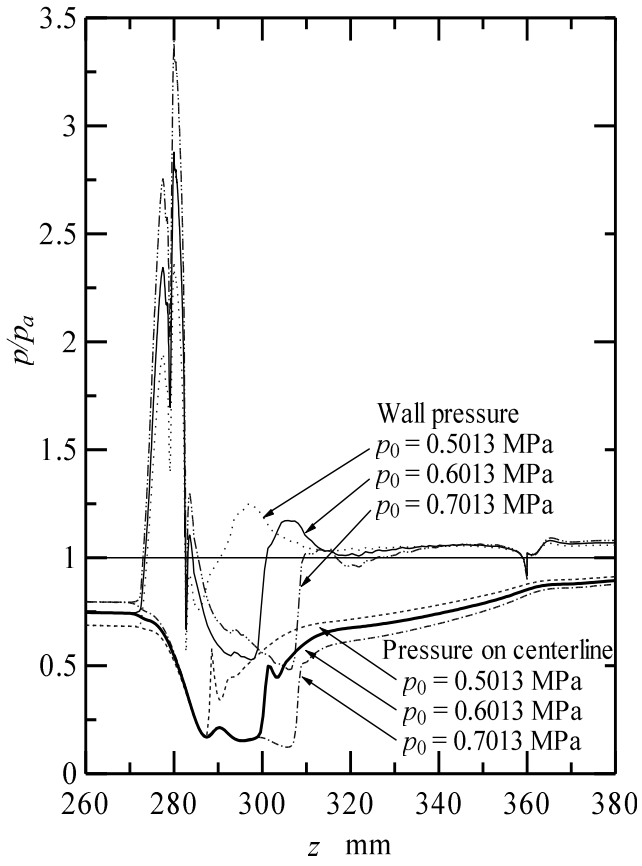

Figure 3.22 Pressure distributions on the wall in the *xz* plane and on the centerline at different supplied air pressure p_0.

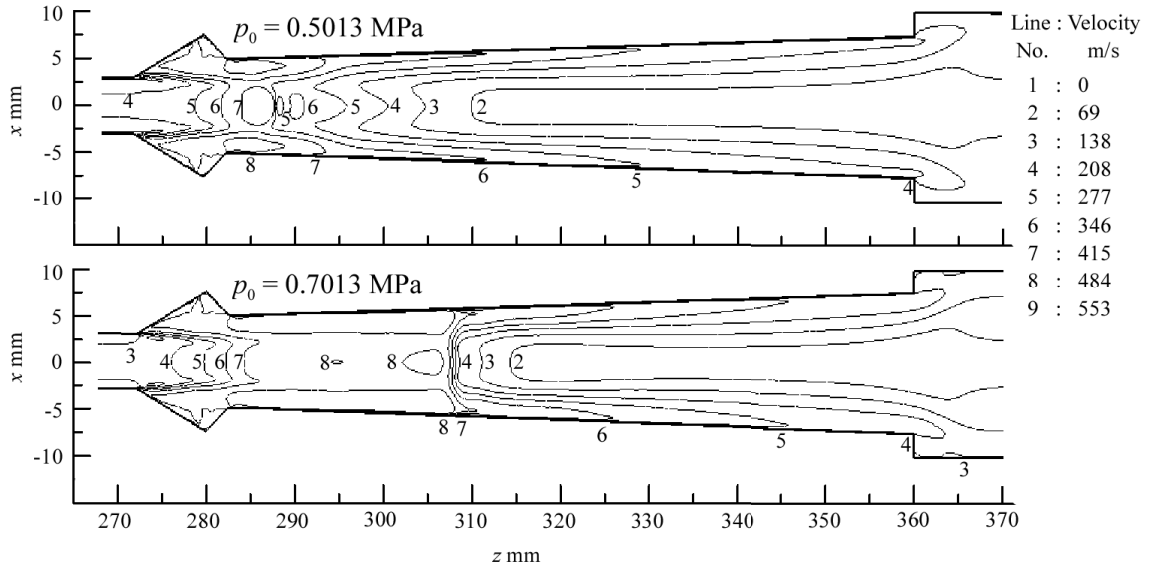

Figure 3.23 Contours of absolute value of velocity in the *xz* plane at different supplied air pressure p_0.

Velocity contours in the *xz* plane at different p_0 are shown in Figs. 3.23 and 3.17. As p_0 is increased, the velocity in the yarn inhalation tube is confirmed to become small and the supersonic flow area is enlarged in the de Laval tube.

Figure 3.24 shows the radial distributions of velocity components and density at the throat in the *xz* plane at different p_0 of 0.5013 ~ 0.7013 MPa. The velocity components v_z and v_c seem not to change so much with an increase in p_0. However, the air density ρ increases greatly. The airflow with critical speed increases ρ to satisfy the law of mass conservation. The extending high-speed region with increasing ρ results in an increment of yarn suction force F_m when p_0 is increased. This is the reason why F_m increases with p_0 in Chapter 2. Here the influence of air compressibility on the airflow distribution is fairly large because of high Mach numbers.

According to the above results, when being operated at higher supplied air pressure, the present gun is not good from the point of view of fluid mechanics because the stronger normal shock wave is generated on the way of the divergent part of the de Laval tube. We experimentally obtained the maximum suction efficiency when the yarn suction gun was operated at p_0 = 0.5013 MPa in Chapter 2. The reason may be that the strong normal shock wave does not occur in this case as shown in Fig. 3.23. In addition, since the air in the yarn passage of the gun flows together with a yarn, the airflow will be a little different from that without a yarn.

Figure 3.25 shows radial distributions of velocity components and density at the

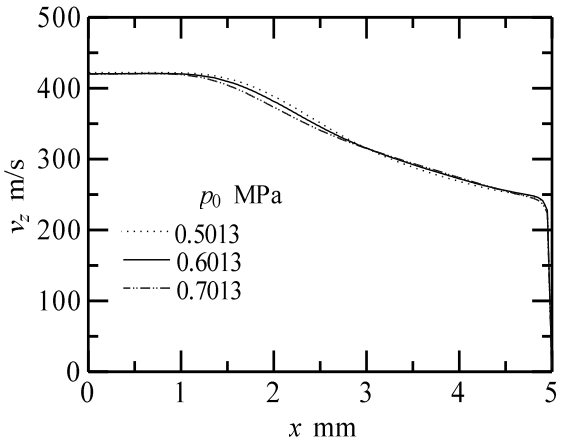

(a) Axial velocity component

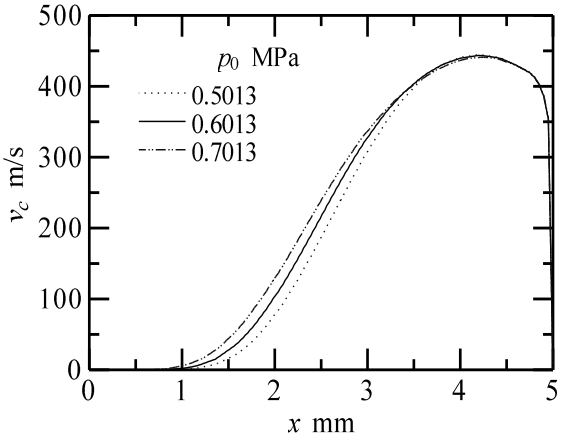

(b) Circumferential velocity component

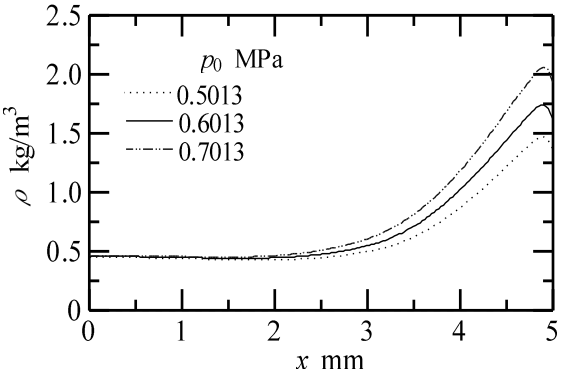

(c) Density

Figure 3.24 Radial distributions of axial velocity component v_z, circumferential one v_c and density ρ at the throat (z = 284.5 mm) of de Laval tube at different supplied air pressure p_0.

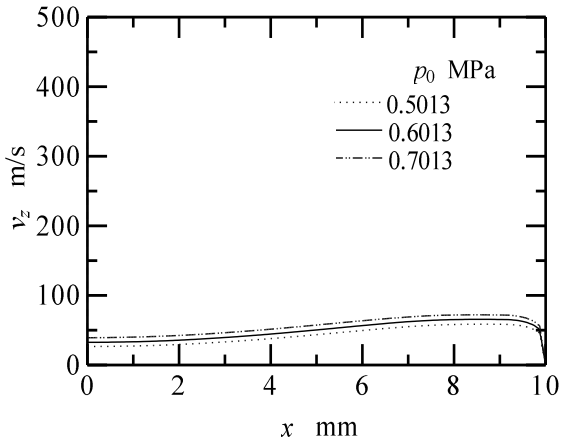

(a) Axial velocity component

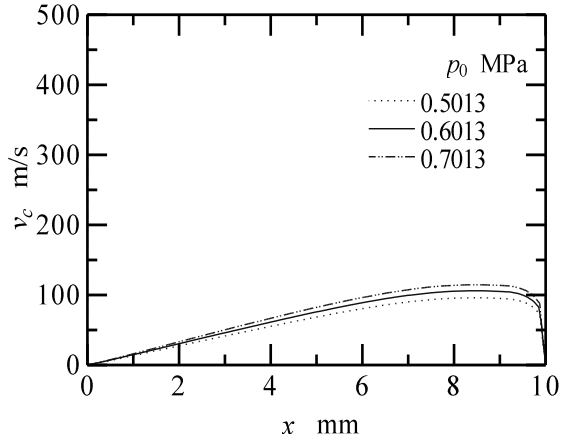

(b) Circumferential velocity component

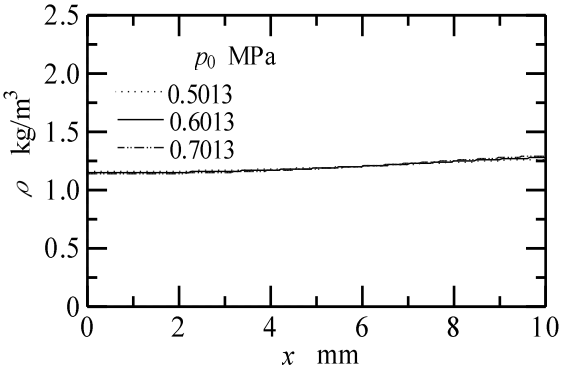

(c) Density

Figure 3.25 Radial distributions of axial velocity component v_z, circumferential one v_c and density ρ at the middle section (z = 470 mm) of straight tube at different supplied air pressure p_0.

middle section of the straight tube in the *xz* plane at different p_0 of 0.5013 ~ 0.7013 MPa. In the straight tube, both v_z and v_c increase with p_0, but p_0 influences v_c more strongly than v_z, and successively raising p_0 has a negligible effect on changing the air density ρ.

Finally, an increase in p_0 to enhance F_m will also produce an increased negative impact such as increasing energy, noise pollution etc. Therefore, increasing p_0 to too high value is not a superior solution.

3.7 Conclusions

In this chapter flow patterns in a yarn suction gun and effect of supplied air pressure on the flow patterns were investigated. Results obtained are as follows:

(1) There is a vacuum core in the yarn propulsion tube. The intense negative pressure region is located in the de Laval tube.

(2) Compressed air issued from the compressed-air inflow tubes to the yarn passage accelerates with entraining the sucked ambient air through the yarn inhalation tube, attains a supersonic speed near the throat of the de Laval tube and keeps accelerating. The supersonic flow generates a normal shock wave on the way of the divergent part of the de Laval tube. The air becomes subsonic and then is discharged into the atmosphere.

(3) The compressed-air issued with a circumferential component proceeds helically in the yarn propulsion tube. The velocity and density of helical airflow near the wall are larger than those near the centerline. This high focusing ability and a large yarn length in the airflow greatly promote the suction efficiency.

(4) Successively raising supplied air pressure causes a decrease in the air velocity in the yarn inhalation tube. However, it causes the extension of the supersonic flow area with increasing density after airflow reaching a critical speed near the throat of the de Laval tube. Since a contact area between air and yarn and air density near the wall are large in the yarn propulsion tube, the successively raising supplied air pressure causes an increase in yarn suction force although it has no great effect on the increase in velocity.

We will numerically investigate the airflow in the yarn suction gun with different geometry in the next chapter.

References

[1] Iemoto Y (1997) Interlacing process of multiple filament yarns. *Japanese J of Multiphase Flow*, **11**, 23-29

[2] Chono S, Iemoto Y (1999) Study on interlaced yarn Part 7: Yarn motion and production mechanism of tangling part. *J Text Mach Soc Japan* (predecessor journal of *J Text Eng*), **45**, 108-112

[3] Iemoto Y, Chono S, Qin H, Lou W (2000) Size effect of interlacer Part 2: Pressure distribution of air flow in interlacers. *J Text Eng*, **46**, 11-19

[4] Murakami K, Tokunaga K, Nomura S, Naito S, Abe M (2006) Characteristics of incompressible air flow in an interlacer. *J Text Eng*, **52**, 73-79

[5] Tokunaga K, Murakami K, Kitamura M, Nomura S, Naito S (2006) Characteristics of compressible air flow in an interlacer and yarn entanglement. *J Text Eng*, **52**, 121-129

[6] Iemoto Y, Tanoue S, Qiu H (2010), Numerical simulation of effects of size of circular yarn duct of interlacer on airflow patterns. *J Text Eng*, 56, 87-96

[7] Iemoto Y, Tanoue S (2008) Interlacing process of multiple filament yarn. *J Text Eng*, **54**, 207-215

[8] Iemoto Y, Tanoue S, Lu J, Takano T (2009) Effects of size of interlacer on air flow in a yarn duct. *J Text Eng*, **55**, 111-118

[9] Yu C, Zhang W (1996) Pressure and velocity distribution of jet-flow field in the air-jet spinning nozzle. *Journal of China Textile University*, **22**(4), 47-57

[10] Zeng Y, Yu C (2003) Numerical simulation of air flow in the nozzle of an air-jet spinning machine. *Text Res J*, **73**, 350-356

[11] Guo H, An X, Yu C (2007) Numerical study on the principle of yarn formation in Murata air-jet spinning. *J Text Eng*, **53**, 173-178

[12] Bergada J, Valencia E, Coll L (2007) Flow characterization in cylinders for pneumatic spinning. *Text Res J*, **77**, 67-76

[13] Ishida M, Okajima A (1994) Flow characteristic of the main nozzle in an air-jet loom Part I: measuring flow in the main nozzle. *Text Res J*, **64**, 10-20

[14] Adanur S, Bahfiyarov S (1996) Analysis of air flow in single nozzle air-jet filling insertion: corrugated channel model. *Text Res J*, **66**, 401-406

[15] Shintani R, Okajima A (2002) Air flow through a weft passage of profile reed in air-jet looms. *J Text Eng*, **48**, 56-63

[16] Hatta K, Kinari T, Shintaku S (2006) Air drag force on a yarn and use of a coaxial jet for yarn operation. *J Text Eng*, **52**, 217-226

[17] Rewi S, Pai H, Wang I (2001) Fluid Simulation of the Airflow in Interlacing Nozzles. *Text Res J*, **71**, 630-634

[18] Rewi S, Pai H, Wang I (2002) Fluid Simulation of the Airflow in Texturing Jets. *Text Res J*, **72**, 520-525

[19] Finnemore E. J, Franzini J. B (2003) *Fluid Mechanics with Engineering Applications (10th ed)*, pp356-357, 515-516, 591-597, McGraw-Hill Companies, Inc., New York, USA

Chapter 4

Numerical Analysis of the Geometrical Effects on the Airflow Characteristics of Yarn Suction Gun

List of Symbols

x, y, z	Cartesian coordinates
ϕ	Compressed-air inflow angle
θ	Passage diverging angle of nozzle
α	Converging angle of de Laval tube
D	Throat diameter of de Laval tube
η	Yarn suction efficiency
F_m	Yarn suction force
G	Mass flow rate of supplied air
p_0	Supplied air pressure
F_a	Yarn capture force
ρ	Air density
v_{ie}	Air velocity at the center of the entrance of yarn inhalation tube
v_z	Axial component of air velocity
v_c	Circumferential component of air velocity
k	Turbulence kinetic energy
ε	Turbulence dissipation rate

4.1 Introduction

A yarn suction gun, an indispensable part of spinning machine for producing fibers, is used to pick up a running yarn at high speed at the beginning of spinning or yarn breakage and take it to a bobbin; and also to transfer the yarn from a full bobbin to an empty one during the bobbin exchange step [1].

For designing a yarn suction gun with high performance at low energy consumption, we have experimentally discussed effects of airflow geometries on the suction characteristics of running yarn and obtained the optimum geometry according to yarn suction efficiency η, which is defined as the ratio of yarn suction force F_m to mass flow rate of supplied air G in Chapter 2. Furthermore, we have clarified the basic working mechanism by investigating the characteristics of airflow in a yarn suction gun and the dependence of flow patterns on supplied air pressure by numerical simulation in Chapter 3.

The yarn suction occurs by virtue of the friction between the yarn and the high-speed airflow. Hence the yarn suction efficiency of the yarn suction gun is closely related to the airflow patterns, which are strongly affected by the airflow geometry. In this chapter we will investigate the airflow patterns in the yarn suction gun with different geometrical parameters by numerical simulation with the aim of clarifying the relation between the flow patterns and the yarn suction efficiency, which facilitates a more reasonable geometrical design of the gun. The simulated results will be used to explain the experimental ones in Chapter 2 and the optimum geometrical parameters will be decided by combining the simulated and experimental results. The simulated results will be discussed by focusing more on the features of helical flow such as distributions of axial and circumferential velocity components, in particular the most significant attention will be paid to the flow patterns in the de Laval tube because it plays the most important role in sucking yarns. We will focus discussion on the relation between the airflow characteristics and yarn suction force, which, indicated by yarn tension, refers to a force with which the compressed air entrains a yarn into a yarn suction gun and can be used to evaluate the yarn suction efficiency η because mass flow rate of supplied air G is hardly affected by the geometry of the yarn suction gun compared with F_m as described in Chapter 2.

4.2 Geometry and Size of Yarn Suction Gun

Figure 4.1 is a schematic diagram of the yarn suction gun used in this study. Descriptions of the basic working mechanism and the route of air from a compressor to the gun are omitted because they are the same as those in Chapter 2.

The variable parameters for numerical simulations of airflow in the yarn suction gun are shown in Table 4.1.

Cartesian coordinate system shown in Fig. 4.1 is used to represent positions in the yarn suction gun. The origin of this coordinate system is located at the center of the entrance of yarn inhalation tube. The *z* axis coincides with the centerline of the gun. Axes of two compressed-air inflow tubes are in planes parallel to the *xz* plane and axes of the other two ones are in planes parallel to the *yz* plane.

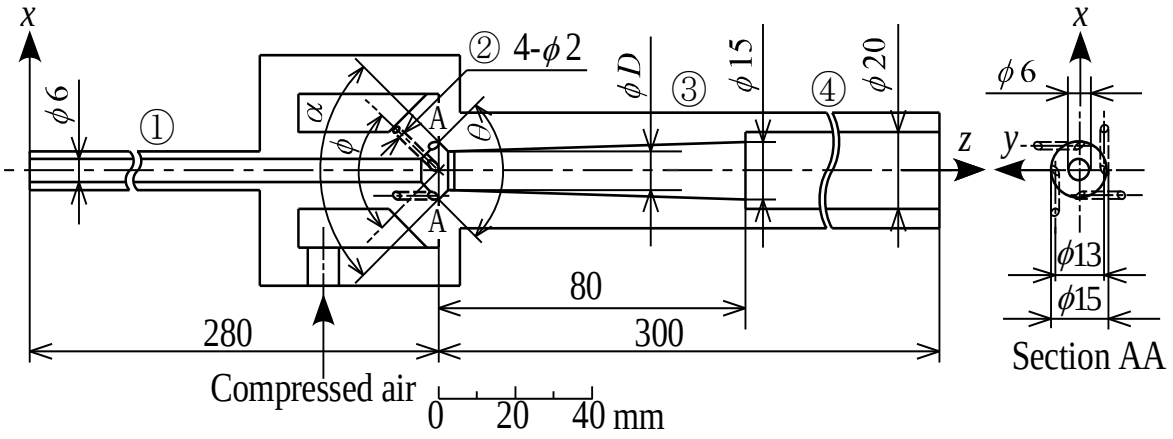

① Yarn inhalation tube ② Compressed-air inflow tube in nozzle ③ de Laval tube ④ Straight tube

Figure 4.1 Schematic diagram of yarn suction gun.

Table 4.1 Geometrical parameters of yarn suction gun

Geometrical parameter	Value
Compressed-air inflow angle ϕ	30, 60, 90, 120, 150, 165°
Passage diverging angle of nozzle θ	30, 60, 90, 120°
Converging angle of de Laval tube α	30, 60, 90, 120, 150°
Throat diameter of de Laval tube D	9, 10, 11, 12, 13, 14 mm

4.3 Numerical Simulation

Numerical simulation was carried out under the condition without a yarn in the yarn passage because yarn apparent diameter is negligibly small compared with the size of the yarn passage.

Figure 4.2 illustrates the three-dimensional calculation domain. The domain is composed of the yarn inhalation tube, the nozzle with four compressed-air inflow tubes, the yarn propulsion tube consisting of the de Laval tube and the straight tube, and two outside air regions connected to the entrance of yarn inhalation tube and the exit of straight tube. The diameter and length of the outside air region on the left are 20 and 50 times the diameter of the yarn inhalation tube respectively. The diameter and length of the outside air region on the right are 5 and 20 times as long as the diameter of the straight tube respectively. They have been decided after sufficiently investigating the effect of their values on the simulated results, as presented in Chapter 3. For shortening the calculating time, computation was performed in a quarter of the domain in the circumferential direction and periodic boundary conditions were set for periodic boundaries.

Air was assumed as an ideal gas with viscosity. This chapter deals with the fluid without considering the yarn involved, which gives a tremendous simplification of the simulation. The governing equations were three-dimensional unsteady compressible Navier-Stokes equations. Turbulence was approximated using a k-ε model. The wall boundary was set as adiabatic and no-slip condition.

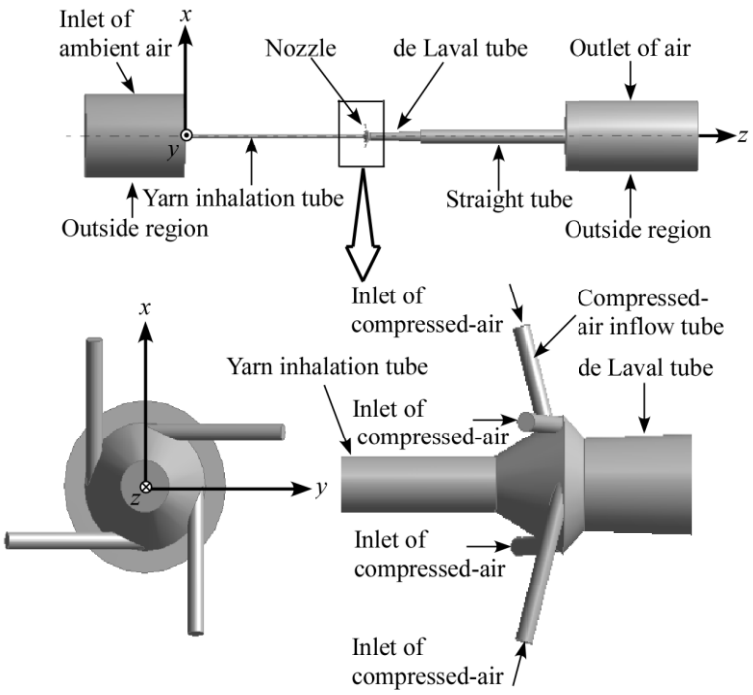

Figure 4.2 Calculation domain for airflow simulation.

The compressed-air inflow tubes were assumed to be connected to a large volume reservoir of highly compressed air where absolute pressure is p_0 and absolute temperature is 293 K, and hence a choked airflow condition at the entrances of the compressed-air inflow tubes was employed as inflow boundary conditions of the compressed air. At absolute pressure p_0 = 0.6013 MPa, i.e. gauge pressure of 0.5 MPa, yarn suction force and mass flow rate were measured in each experiment for clarifying geometrical effects in Chapter 2. Therefore, the present simulations were done at p_0 = 0.6013 MPa for the sake of comparability with the previous study in Chapter 2. The two outside air regions were set to accurately calculate the airflow near the entrance of yarn inhalation tube and the exit of straight tube. Outflow conditions were imposed on the outside boundaries of the two outside air regions. The atmosphere around the outside boundary is at an absolute pressure of 0.1013 MPa and an absolute temperature of 293 K.

We have given the details about the above assumptions in Chapter 3 and thus they are omitted in this chapter.

The CFD software CFX 11.0 (ANSYS Inc.), which has been used for calculating the airflow in the yarn suction gun in Chapter 3 and interlacer [2], was used for solving the governing equations. Computer used for simulation has one CPU (Pentium 4, 3.8 GHz) and 3.5 GB RAM. For the simulation of airflow in the yarn suction gun with ϕ = 150°, θ = 60°, α = 90° and D = 10 mm, the total mesh element number of which is 2,720,390, it requires 51 h to converge the simulation to a level of RSM = 10^{-5}.

4.4 Results and Discussion

4.4.1 Effect of Compressed-air Inflow Angle ϕ on Airflow Patterns

Figure 4.3 shows contours of velocity magnitude and density ρ in and near the nozzle and de Laval tube of the yarn suction gun with different ϕ. These contours are in xz plane. Only half the section is shown because of symmetry. The other three parameters are fixed at passage diverging angle of nozzle θ = 60°, converging angle of de Laval tube α = 90° and throat diameter of de Laval tube D = 10 mm.

The air flows at high speed in the de Laval tube in the case of ϕ = 30°, while the flow pattern is entirely different from other cases and does not show a bias of high-speed and high-density flow towards the vicinity of the wall in the yarn propulsion tube, which is an important characteristic of the yarn suction gun in this study as depicted in Chapter 3. It is

considered because the injected compressed air hardly moves with a rotation along the inner wall in the de Laval tube owing to too small circumferential velocity component. In this case, the air jet in the gun is similar to that in an air-jet loom based on Venturi effect [3-6].

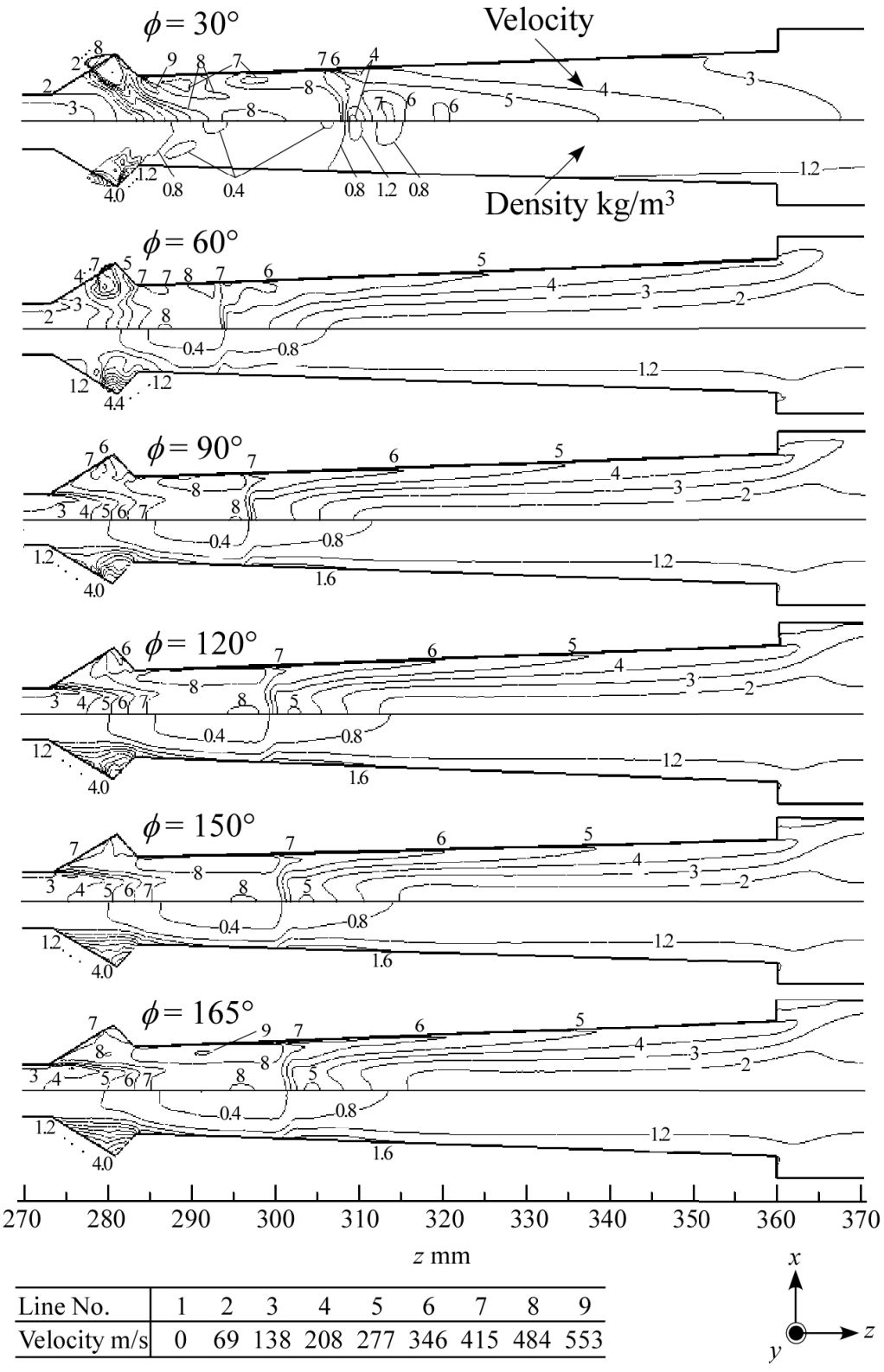

Line No.	1	2	3	4	5	6	7	8	9
Velocity m/s	0	69	138	208	277	346	415	484	553

Figure 4.3 Contours of velocity magnitude and density in *xz* plane at different compressed-air inflow angle ϕ (θ = 60°, α = 90° and D = 10 mm).

When $\phi \geqslant 60°$, the supersonic flow area shown by isovelocity lines Nos. 6-9 in the de Laval tube is elongated along the wall with increasing ϕ and higher density flow (ρ > 1.2 kg/m^3) distributes near the wall. There appears a biased flow towards the vicinity of the wall in the yarn propulsion tube and this bias becomes more noticeable with increasing ϕ. It indicates that helical flow has developed and becomes strong with increasing ϕ. With further increase in ϕ, the normal shock wave [7] is pushed downstream.

In this chapter, the air velocity at the center of the entrance of yarn inhalation tube v_{ie} is used to investigate the effect of geometrical parameters on yarn capture force of yarn suction gun F_a, which refers to a force with which a yarn is attracted to the entrance of yarn inhalation tube and increases with v_{ie}. Like yarn suction force F_m, F_a is also an important characteristic of the gun.

The effect of ϕ on v_{ie} is shown in Fig. 4.4. v_{ie} decreases and then increases with increasing ϕ from 30° to 165°. Before the helical flow is generated effectively at ϕ = 60°, v_{ie} increases as ϕ decreases. A small ϕ may help to improve the Venturi effect. As ϕ increases beyond a certain value, for example ϕ = 60°, a helical flow becomes strong and then draws more ambient air into the yarn suction gun, and therefore causes v_{ie} to increase.

A large yarn capture force F_a can be obtained at ϕ = 30° because v_{ie} increases to a relatively high level, which increases the friction force between the yarn and the air. In this case, however, the yarn suction force F_m is low as shown in Fig. 4.5, which is obtained from Fig. 2.5(a) and shown again in this chapter. Hence an attainment of large F_a does not necessarily mean a large F_m. The yarn suction gun with a large F_a and a large F_m is expected.

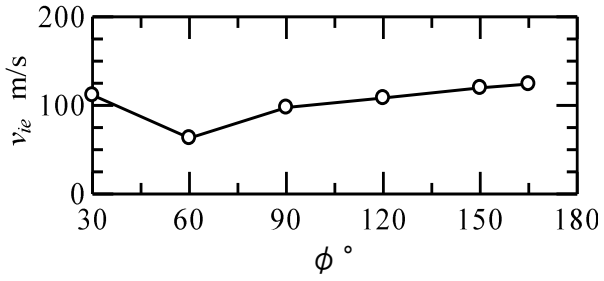

Figure 4.4 Effect of compressed-air inflow angle ϕ on air velocity at center of entrance of yarn inhalation tube v_{ie} (θ = 60°, α = 90° and D = 10 mm).

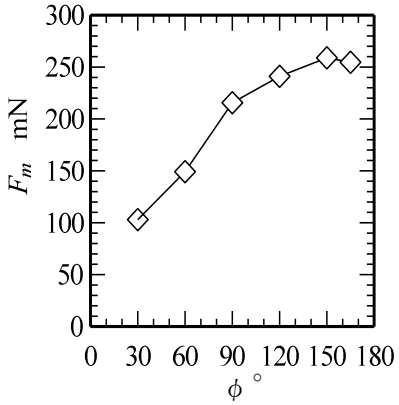

Figure 4.5 Effect of compressed-air inflow angle ϕ on yarn suction force F_m (θ = 60°, α = 90° and D = 10 mm). F_m is the same as at θ = 60° in Fig. 2.5(a).

The circumferential velocity component of airflow is obtained by controlling the incline angle of the compressed-air inflow tube. Therefore, it is important to find the optimum geometry of the compressed-air inflow tube by investigating the effects of ϕ on the axial and circumferential velocity distributions of the airflow in the yarn suction gun.

Figure 4.6 shows the radial distributions of axial and circumferential velocity components of airflow in three cross-sections of the yarn suction gun with different ϕ. The distributions at ϕ = 30° are markedly different from those in other cases. In the range of ϕ from 60° to 165°, both axial velocity component v_z and circumferential velocity component v_c attain large values near the wall; from the profiles of v_c the flow has an obvious three-region structure consisting of wall, annular and core regions [8], which shows the typical

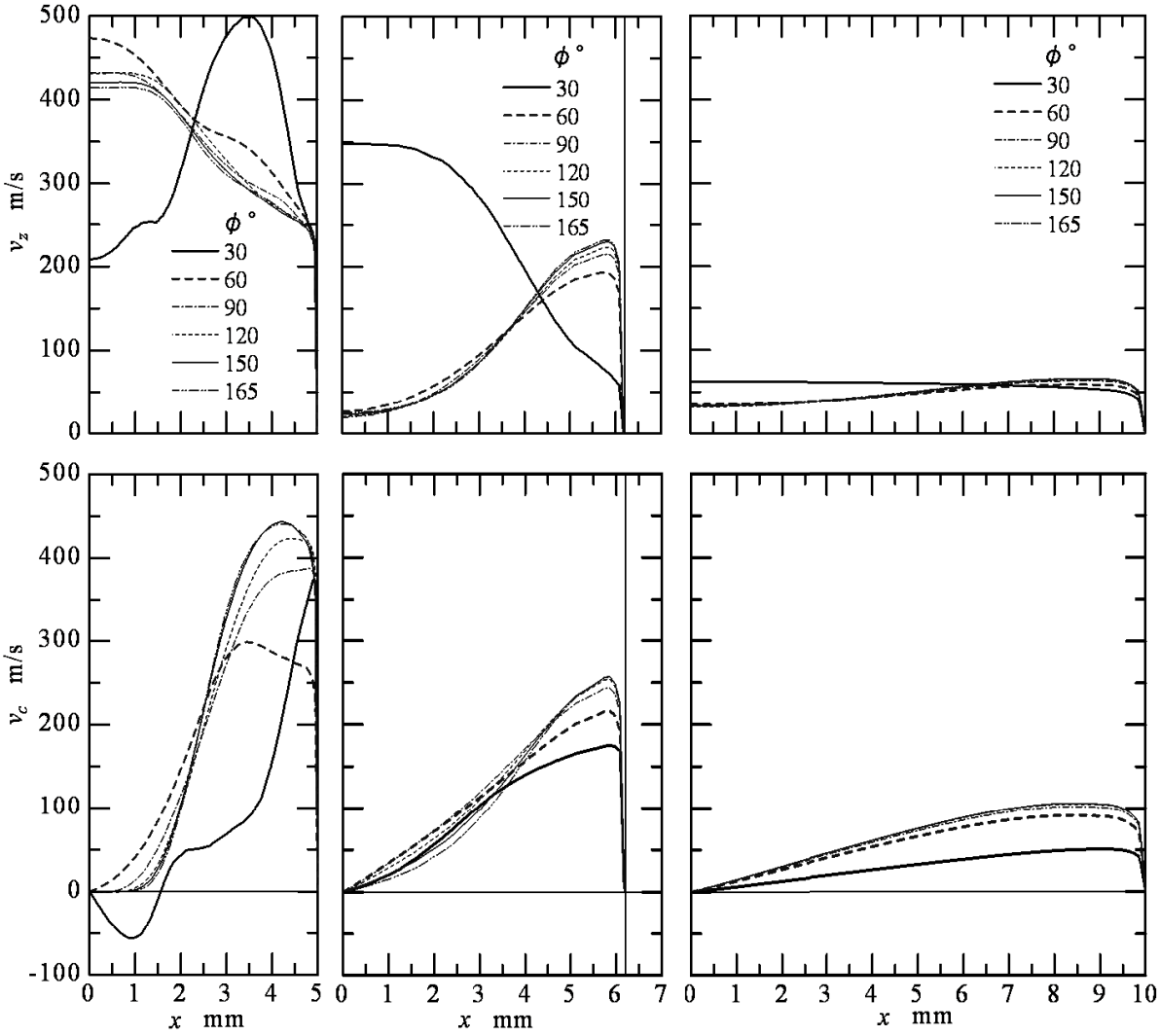

(a) End of throat (z = 284.5 mm) (b) Middle section of de Laval tube (z = 320 mm) (c) Middle section of straight tube (z = 470 mm)

Figure 4.6 Radial distributions of axial and circumferential velocity components in *xz* plane at different compressed-air inflow angle ϕ (θ = 60°, α = 90° and D = 10 mm).

characteristics of strong helical flow. In the wall region the velocity gradient is quite steep. It is clear that the air is in a strong helical motion in the yarn propulsion tube.

ϕ has a small effect on v_z at the end of the throat of the de Laval tube (hereafter called the throat) except for $\phi = 30°$ as shown in Fig. 4.6(a). In the middle of the de Laval tube, both v_z and v_c increase with ϕ near the wall as shown in Fig. 4.6(b). Beyond $\phi = 150°$, their changes tend to be ignorable. At too large ϕ such as 165°, more vortices or backflows are found in the converging part of the de Laval tube according to velocity vector map, which is not given in this chapter. They hinder the increase in v_c. In the middle of the straight tube, v_z becomes nearly constant in radial direction and v_c is small at $\phi = 30°$, as shown in Fig. 4.6(c). The boundary between the core and annular region becomes obscure, and thus a very weak helical motion dominates the whole section. In the range $\phi = 60\text{-}165°$, v_c increases with ϕ and is hardly affected by ϕ when $\phi \geqslant 90°$; the effect of ϕ on v_z is negligibly small.

On the whole, the increase in ϕ causes v_z and v_c to become large, but their changes are very small when $\phi \geqslant 150°$. Therefore, it is not necessary to increase ϕ above 150° according to the simulated results.

Now we will discuss the relation between the flow patterns and yarn suction force F_m. The yarn suction force F_m exerted on a yarn running at the same speed depends on air velocity, air density and length of the yarn in the airflow. It is impossible for us to quantitatively analyze the relation between flow patterns and F_m in the present study. Therefore, only a qualitative analysis can be given. In our discussion we will emphasize the air velocity distribution because the effect of ϕ on ρ is much smaller than on the air velocity in the range $\phi \geqslant 60°$ and the variation in F_m due to variation in ρ is also very small compared with that caused by variation in air velocity.

An increase in ϕ mainly causes v_c to increase in the yarn propulsion tube and the effect of ϕ on v_z is small. As ϕ increases, F_m increases to the maximum value at $\phi = 150°$ and then decreases, as shown in Fig. 4.5. v_c and F_m present the similar trend with variation of ϕ. Therefore, F_m may be affected significantly by v_c in the yarn propulsion tube, and shows less relationship to v_z. The reason is considered as follows: As v_c increases, the helical pitch of a running yarn in the airflow becomes small and the yarn length in the yarn propulsion tube becomes long, and as a result, frictional force between the air and the yarn will become large. At the same time, the air velocity near the wall increases with ϕ. These lead to an increase in F_m. However, the promotion of F_m will be hindered when $\phi > 150°$ because of the

aforementioned reason. F_m is small at ϕ = 30° owing to small v_c and low air density near the wall of the yarn propulsion tube, although relatively high value of v_{ie} can be obtained. It implies that F_m is under little influence of airflow in the yarn inhalation tube.

The yarn suction gun with ϕ = 150° gives an appropriate yarn capture capacity and good flow patterns with long high-speed and high-density flow area near the tube wall and minimal turbulent condition, which produce the largest value of F_m.

From above discussions, an increase in ϕ from 30° to 150° dominantly causes increases in v_c and ρ near the wall of the yarn propulsion tube and the air velocity in the yarn inhalation tube; this improves the yarn suction capacity.

4.4.2 Effect of Passage Diverging Angle of Nozzle θ on Airflow Patterns

Figure 4.7 shows contours of velocity magnitude and density ρ in and near the nozzle and de Laval tube at different θ. Values of ϕ, α and D are fixed at 150°, 90° and 10 mm, respectively. An increase in θ from 30° to 90° causes an enlargement of the supersonic flow area generated near the throat accompanied by a slight increase in ρ. Increasing θ to 120°, the flow exhibits a complicated pattern near the throat. An over-large θ causes, therefore, a highly turbulent condition near the throat. This is because more backflows are produced in the converging part of the de Laval tube than in other cases since the outlets of the compressed-air inflow tubes are too close to the inner wall of the converging part. This will cause F_m to decrease because increased dissipation resides in the air kinetic energy diverted to the strong turbulent motion which results from nonuniformity of the flow; this kinetic energy is finally dissipated by friction of air [9], and is therefore ineffective in producing increases in F_m. Hence the nozzle should be shaped to avoid the highly turbulent condition. Changing θ has little effect on the distribution of velocity and density in the rest of the yarn propulsion tube downstream from the normal shock wave.

At the entrance of yarn inhalation tube, air velocity v_{ie} attains relatively large values in the range of θ from 60° to 90° as shown in Fig. 4.8. This means that a large F_a can be obtained in this rather wide range of θ.

Near the wall, v_c becomes highest at θ = 60°, as shown in Fig. 4.9. In general, however, changing θ from 30° to 120° has no distinctive effect on the distribution of velocity in the de Laval tube.

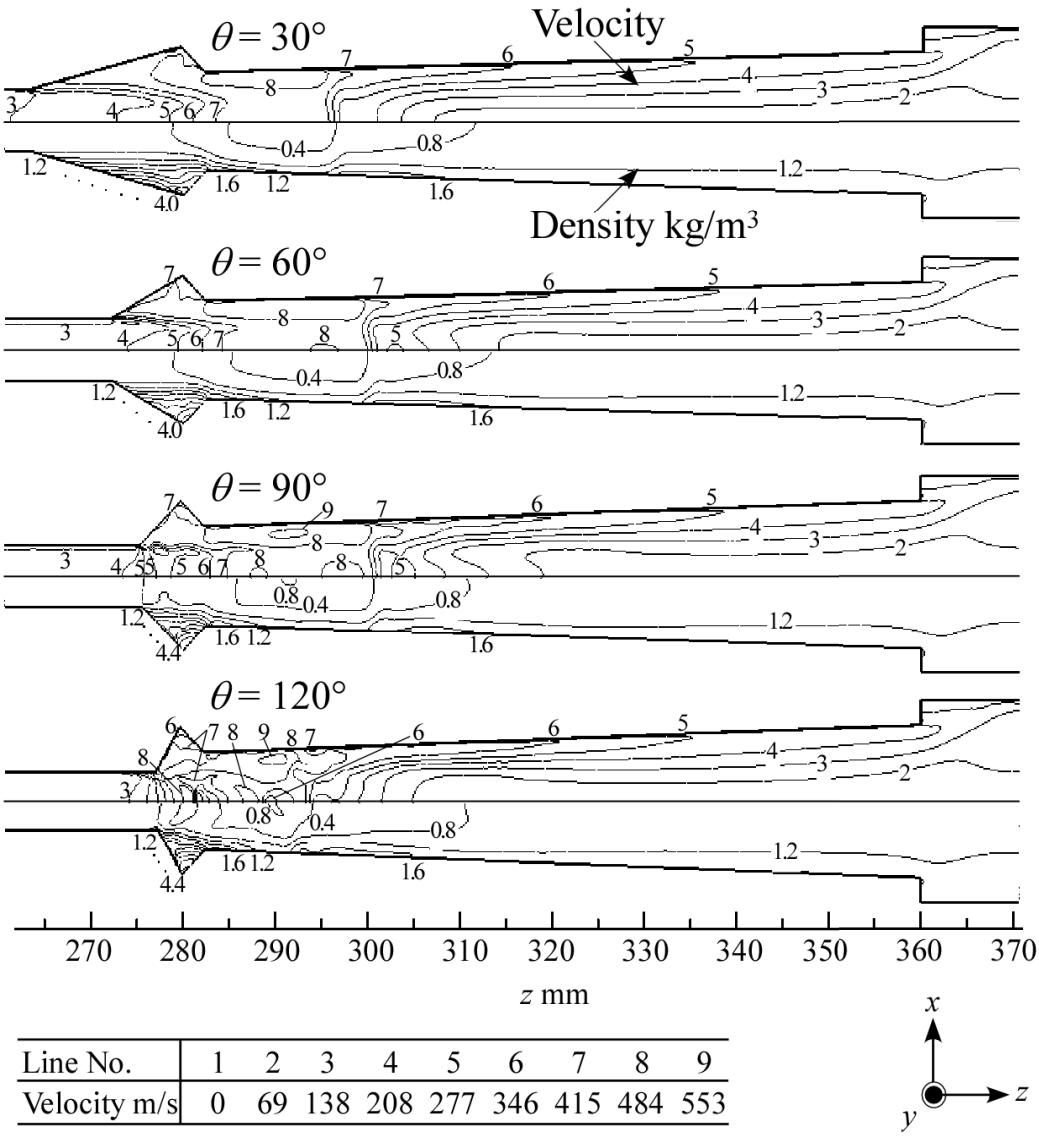

Line No.	1	2	3	4	5	6	7	8	9
Velocity m/s	0	69	138	208	277	346	415	484	553

Figure 4.7 Contours of velocity magnitude and density in *xz* plane at different passage diverging angle of nozzle θ (ϕ = 150°, α = 90° and D = 10 mm).

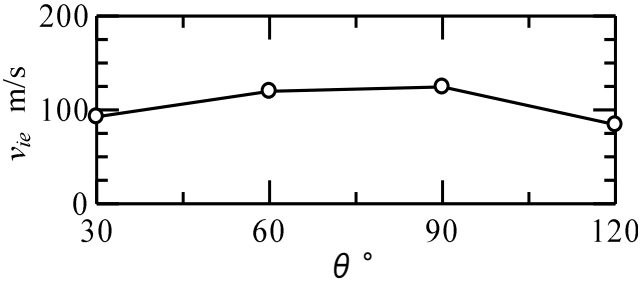

Figure 4.8 Effect of passage diverging angle of nozzle θ on air velocity at center of entrance of yarn inhalation tube v_{ie} (ϕ = 150°, α = 90° and D = 10 mm).

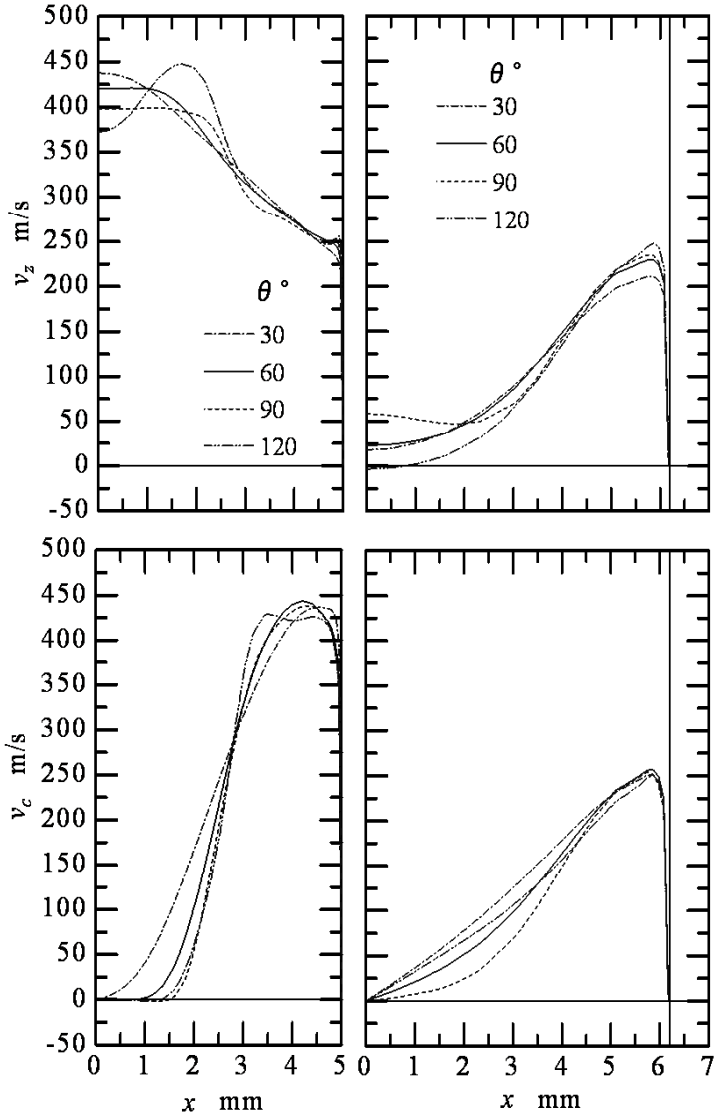

(a) End of throat (b) Middle section of de Laval tube

(z = 284.5 mm) (z = 320 mm)

Figure 4.9 Radial distributions of axial and circumferential velocity components in *xz* plane at different passage diverging angle of nozzle θ (ϕ = 150°, α = 90° and D = 10 mm).

In the middle section of the straight tube, the profiles of v_z and v_c at various θ are similar to those at ϕ = 150°, θ = 60°, α = 90° and D = 10 mm in Fig. 4.6(c). Therefore, they are not presented here.

The diverging part of the nozzle is designed not only to provide surface to generate a tangential velocity component of the injected airflow, but also to hinder the backflow from the outlets of the compressed-air inflow tubes produced owing to the expansion of the injected compressed air. A reduction of θ results in an increase in the backflows; this causes the velocity of entrained ambient air in the yarn inhalation tube to decline. For example, this

occurs at $\theta = 30°$ as shown in Fig. 4.8. On the other hand, too large θ may also lead to a rise in pressure in the yarn inhalation tube owing to the strong turbulence near the throat. The strong turbulence also reduces the velocity of the helical flow. More backflows are found to happen in the nozzle diverging part because of too small space near the outlets of the compressed-air inflow tubes for the expansion of the injected compressed air. As a result, the air velocity in the yarn inhalation tube is decreased. For instance, this happens at $\theta = 120°$.

The yarn suction gun with $\theta = 60°$ gives good flow patterns, and has the maximum value of v_c near the wall in the yarn propulsion tube; this enhances the yarn suction force F_m. It agrees well with the measured data in Chapter 2 that F_m reaches the maximum value at $\theta = 60°$ (Fig. 4.10). In this case, a large yarn capture force can also be obtained as discussed above. Thus it is considered to be rational that θ is about 60°.

From the discussion above, however, θ has a small effect on the flow patterns in the yarn propulsion tube, which plays a major role in controlling F_m. This is the reason why the change of F_m with respect to θ is small as presented in Fig. 4.10, which is obtained from Fig. 2.5(a).

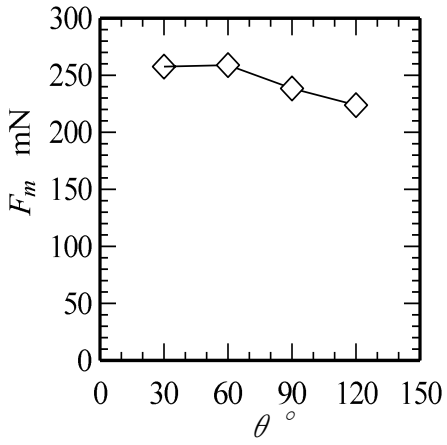

Figure 4.10 Effect of passage diverging angle of nozzle θ on yarn suction force F_m ($\phi = 150°$, $\alpha = 90°$ and $D = 10$ mm). F_m is the same as at $\phi = 150°$ in Fig. 2.5(a).

4.4.3 Effect of Converging Angle of de Laval Tube α on Airflow Patterns

The general flow behavior at various α is similar except for the high-speed flow area near the throat, which becomes large with α, and the distribution of air density is almost unchanged, as shown in Fig. 4.11.

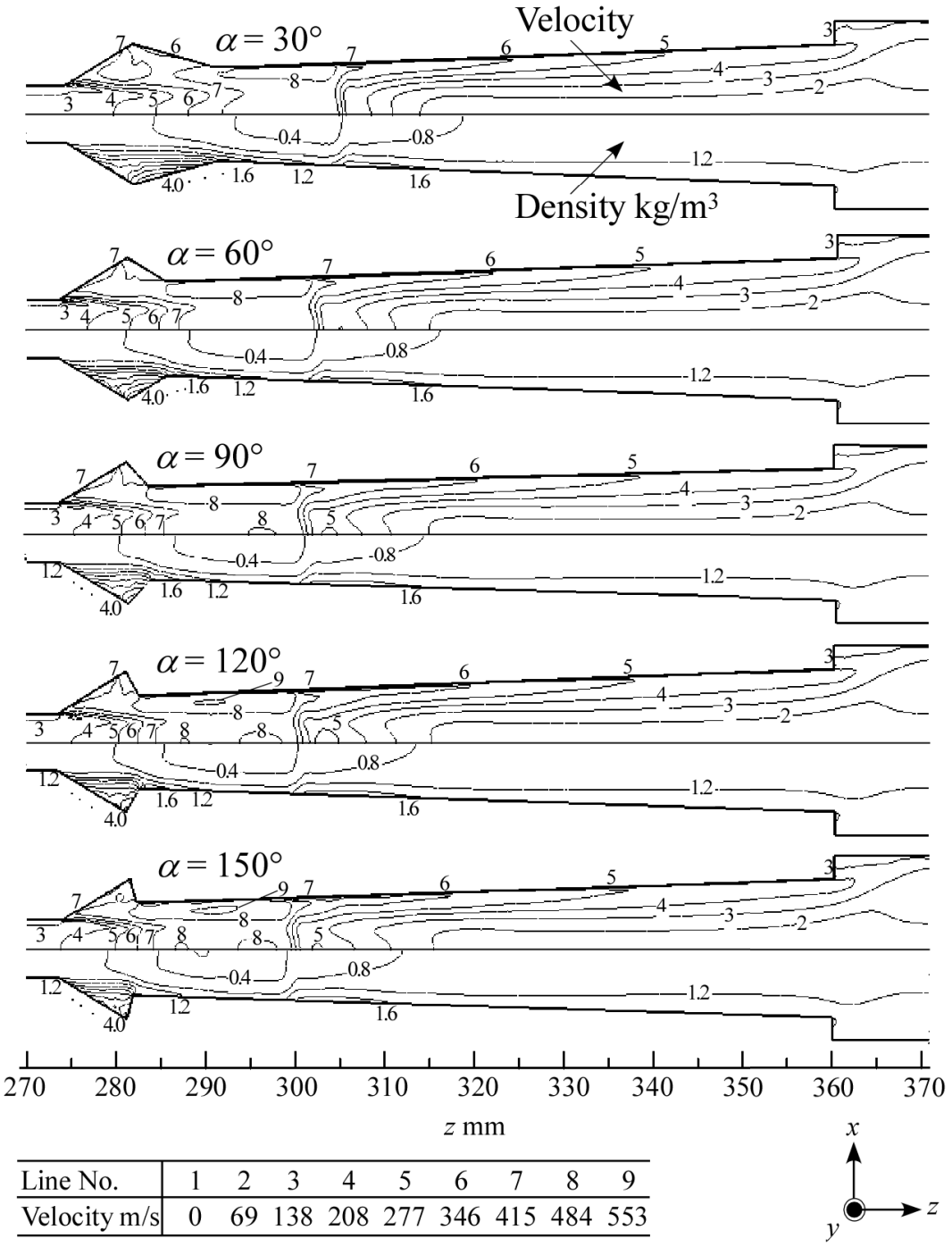

Line No.	1	2	3	4	5	6	7	8	9
Velocity m/s	0	69	138	208	277	346	415	484	553

Figure 4.11 Contours of velocity magnitude and density in *xz* plane at different converging angle of de Laval tube α ($\phi = 150°$, $\theta = 60°$ and $D = 10$ mm).

At the entrance of yarn inhalation tube, v_{ie} keeps nearly constant in the range α = 30-150° as shown in Fig. 4.12. Therefore, α has a negligible influence on F_a.

In the de Laval tube, the effect of α on v_z can be neglected as shown in Fig. 4.13. Here the position of the throat depends on the value of α. v_c near the wall of throat increases with α, which may result in an increase in F_m, and turns out nearly constant in the range of α from

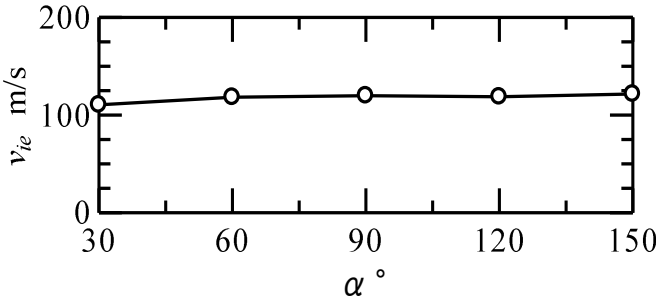

Figure 4.12 Effect of converging angle of de Laval tube α on air velocity at center of entrance of yarn inhalation tube v_{ie} (ϕ = 150°, θ = 60° and D = 10 mm).

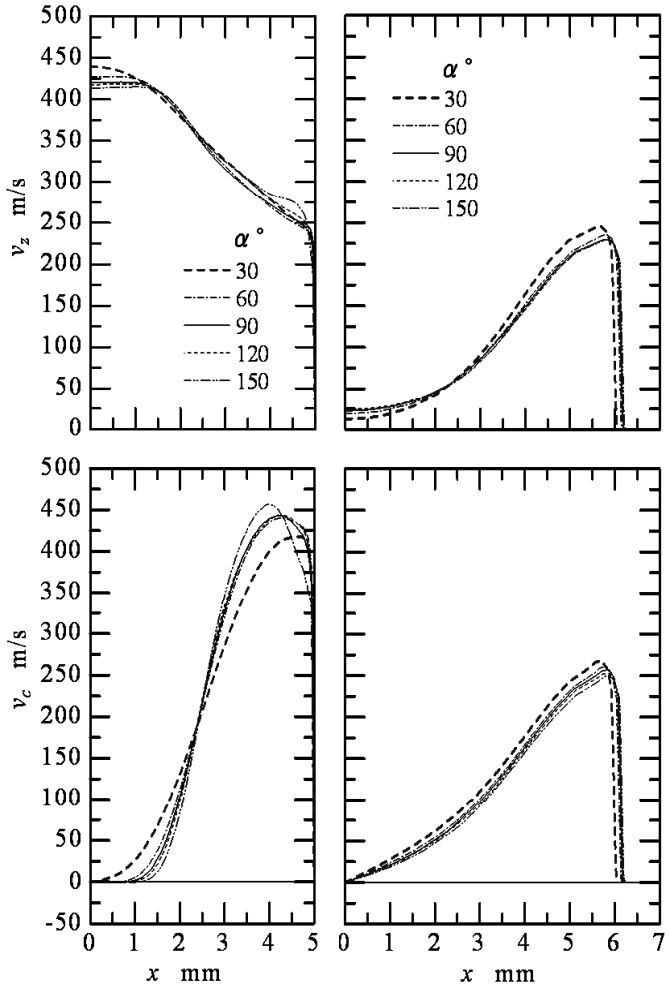

(a) End of throat (b) Middle section of de Laval tube (z = 320 mm)

Figure 4.13 Radial distribution of axial and circumferential velocity components in xz plane at different converging angle of de Laval tube α (ϕ = 150°, θ = 60° and D = 10 mm).

60° to 120°. When α is varied, there is also little difference in the distributions of v_c in the middle of the de Laval tube.

In the middle section of the straight tube, the profiles of v_z and v_c are also almost identical to those at ϕ = 150°, θ = 60°, α = 90° and D = 10 mm in Fig. 4.6(c). Therefore, they are not shown here.

A good match between ϕ and α should be taken into consideration to allow the injected compressed air to flow smoothly along the inner wall of the converging part of the de Laval tube. For example, a relatively small v_c near the wall is found in the case of α = 30° because of poor ability to direct the injected airflow. Likewise, too large α causes the development of backflow. These bad effects lead to a decline in F_m.

F_m increases to the maximum value at α = 90° and then decreases as α increases; however it shows a relatively small variation with α as described in Fig. 4.14, which is obtained from Fig. 2.6(a). This agrees with the flow behavior observed in this study. Thus the rational value of α is about 90° from the results of simulations and experiments.

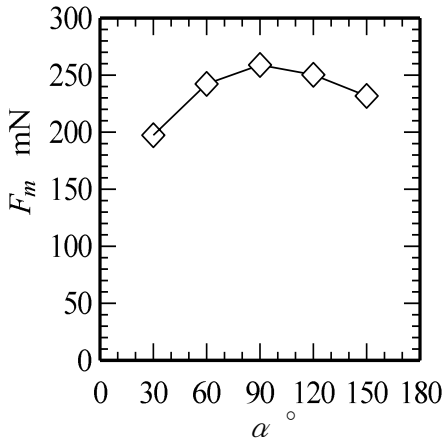

Figure 4.14 Effect of converging angle of de Laval tube α on yarn suction force F_m (ϕ = 150°, θ = 60° and D = 10 mm). F_m is the same as at D = 10 mm in Fig. 2.6(a).

4.4.4 Effect of Throat Diameter of de Laval Tube *D* on Airflow Patterns

Simulated results of airflow in the yarn suction gun with different D are discussed in the follows. We fix ϕ, θ and α at 150°, 60° and 90° respectively, varying D from 9 to 14 mm in increments of 1 mm.

Contours of velocity magnitude and density ρ in and near the nozzle and de Laval tube at different D are shown in Fig. 4.15. The flow pattern differs significantly for each case. As D decreases, the supersonic flow area in the de Laval tube shows a rapid extension

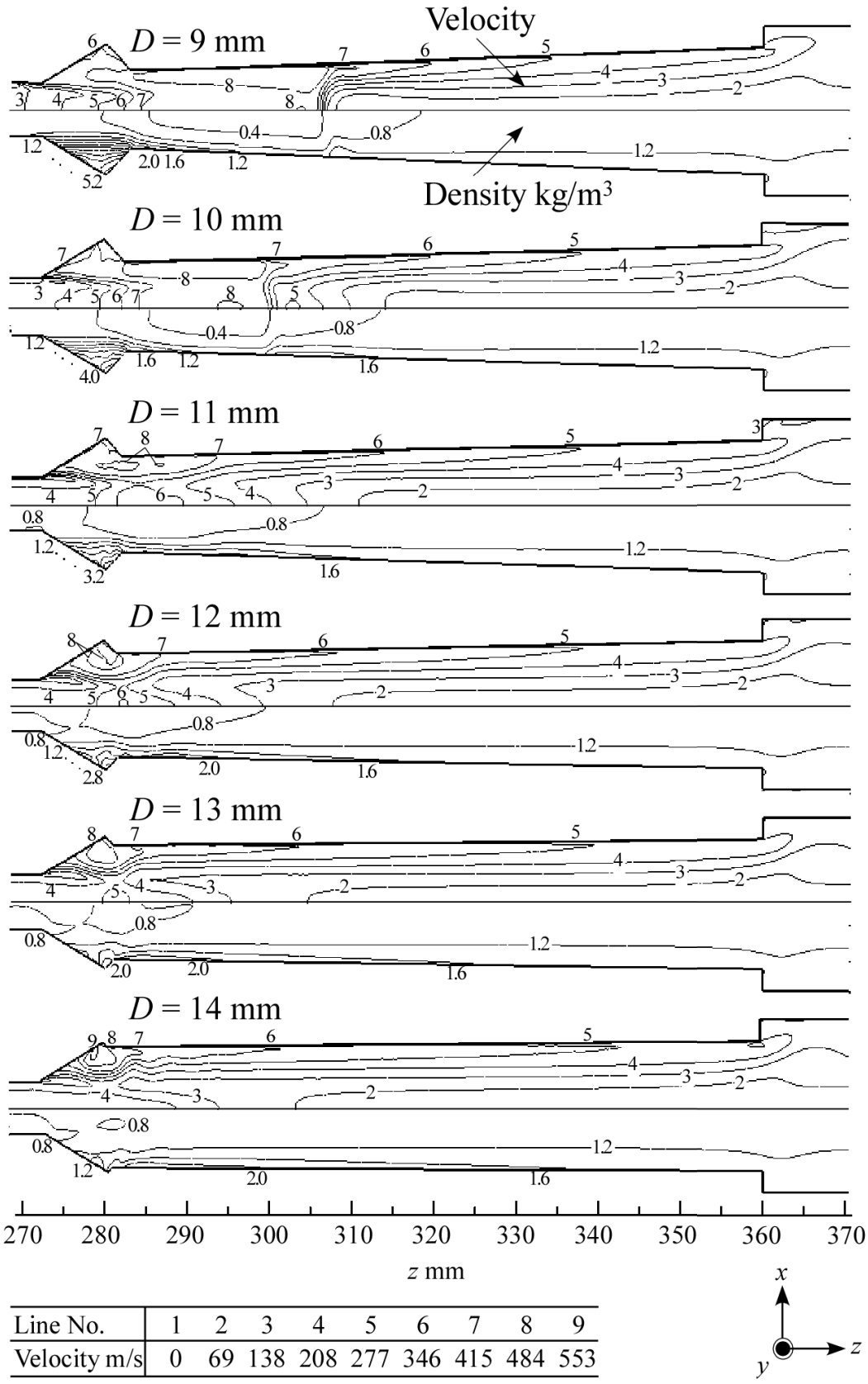

Line No.	1	2	3	4	5	6	7	8	9
Velocity m/s	0	69	138	208	277	346	415	484	553

Figure 4.15 Contours of velocity magnitude and density in *xz* plane at different throat diameter of de Laval tube D ($\phi = 150°$, $\theta = 60°$ and $\alpha = 90°$).

accompanied by a corresponding increase in speed. This demonstrates that the accelerating effect of the converging part of the de Laval tube [7] increases with decreasing D. However, ρ decreases with decreasing D in the vicinity of the wall in the divergent part of the de Laval tube; this may hinder the increase in yarn suction force F_m, which strongly depends on the speed and density of airflow near the wall in the present yarn suction gun. When D is decreased to a certain value of 10 mm, a complete normal shock wave followed by a subsonic region exists in the diverging part of the de Laval tube.

At the entrance of yarn inhalation tube, v_{ie} increases with D, and remains unchanged in the range D = 12-14 mm, as shown in Fig. 4.16. It is so small at D = 9 mm that poor yarn capture force occurs.

Air velocity in the de Laval tube can be improved considerably through reducing D so that F_m is maintained, but the pressure in the yarn inhalation tube will rise, which will bring on a difficulty in capturing a yarn because of the low yarn capture force.

The profiles of v_z and v_c in three cross-sections of the yarn suction gun with different D are plotted in Fig. 4.17. The position of the throat also varies with D. As shown in Figs. 4.17 (a) and (b), v_z increases roughly with decreasing D in the de Laval tube owing to conservation of mass and, moreover, its fluctuation becomes less. v_c near the wall of the throat shows little relation to D. The reason may that the change of v_c due to conservation of angular momentum is indistinctive because of small variation in the radius of the throat. In the middle section of the de Laval tube, v_c near the wall increases slightly with D. In the middle section of the straight tube, both v_z and v_c increase with D near the wall, and the variation of v_z with D, however, can be neglected.

The high-speed flow area can be enlarged by decreasing D so that F_m increases, but F_m takes the maximum at D = 10 mm as presented in Fig. 4.18, which is obtained from Fig. 2.6(a). Therefore, other factors concerning F_m should be considered. One is the yarn drag

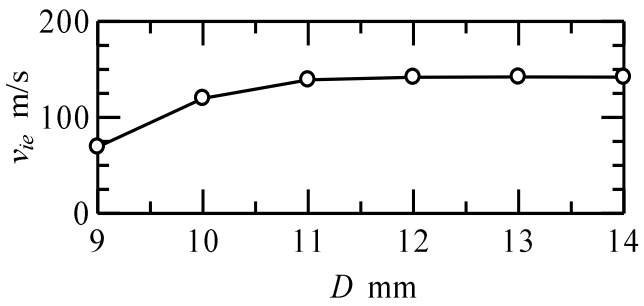

Figure 4.16 Effect of throat diameter of de Laval tube D on air velocity at center of entrance of yarn inhalation tube v_{ie} (ϕ = 150°, θ = 60° and α = 90°).

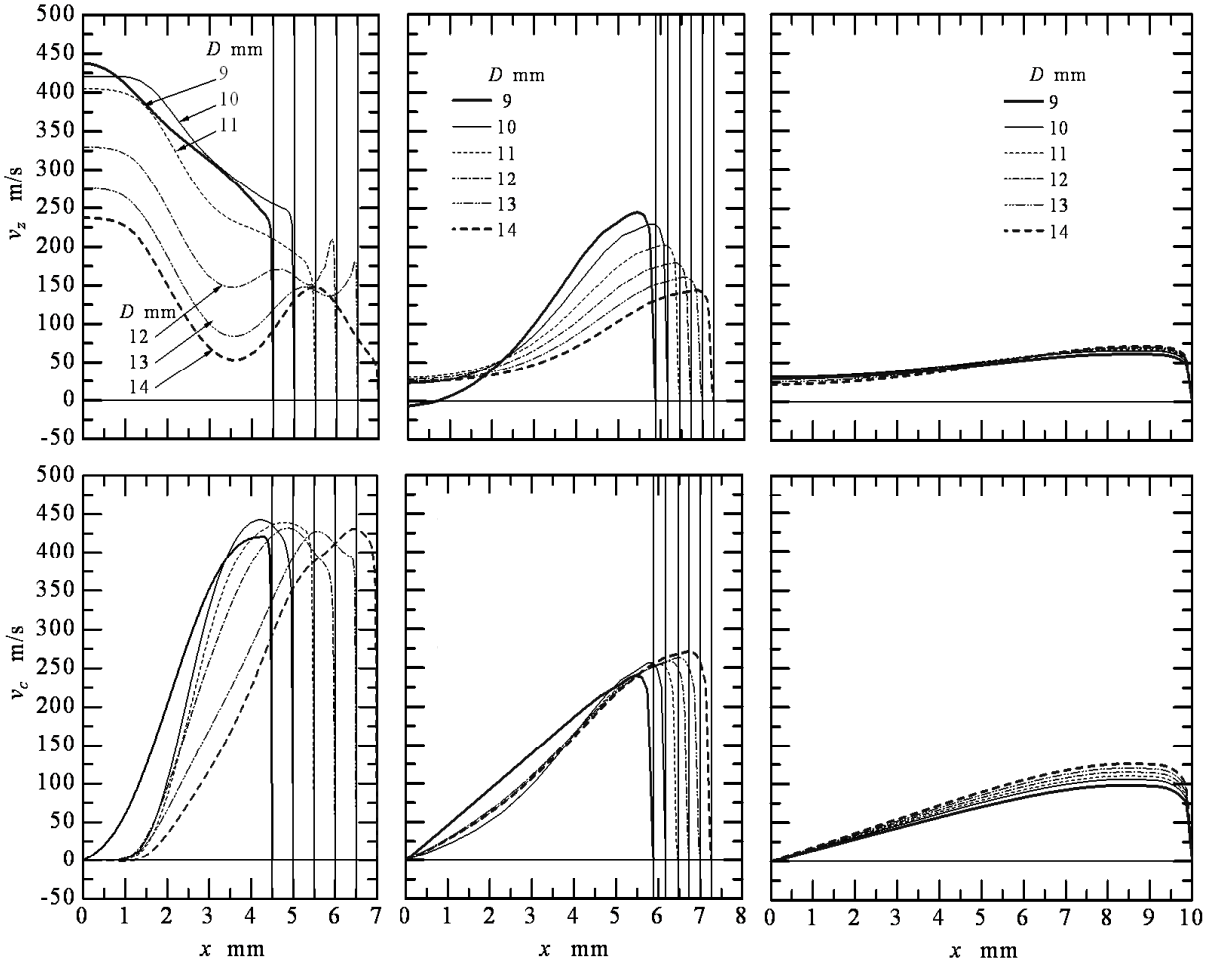

(a) End of throat (b) Middle section of de Laval tube (z = 320 mm) (c) Middle section of straight tube (z = 470 mm)

Figure 4.17 Radial distributions of axial and circumferential velocity components in xz plane at different throat diameter of de Laval tube D (ϕ = 150°, θ = 60° and α = 90°).

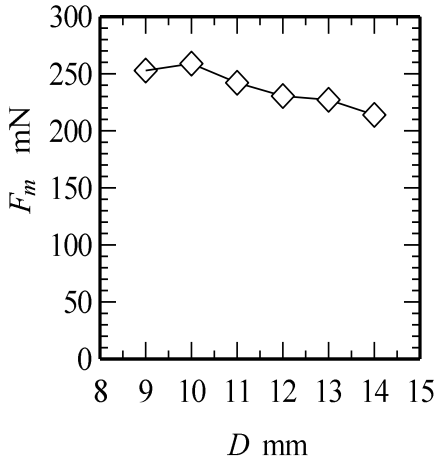

Figure 4.18 Effect of throat diameter of de Laval tube D on yarn suction force F_m (ϕ = 150°, θ = 60° and α = 90°). F_m is the same as at α = 90° in Fig. 2.6(a).

force produced in the yarn inhalation tube, which decreases with D because of lower air velocity. Another factor under consideration is the distributions of v_z and v_c in the yarn propulsion tube. As D is decreased, the increase in v_z brings about a rise in F_m, but the corresponding decrease of v_c results in a decline in F_m. F_m is closely related to not only the magnitudes of v_c and v_z but also the ratio between them, and depends strongly on v_c. F_m will decrease when the above bad influences increase to a certain extent. For example, this case occurs at D = 9 mm. In addition, the decrease of ρ near the wall of the de Laval tube with decreasing D hinders the increase in F_m as discussed above. Thus the results of simulations and experiments suggest that the optimum value of D is 10 mm.

Generally, the dependency of flow pattern on D is large in comparison with ϕ, θ and α. However, D has a smaller influence on F_m than ϕ as mentioned in Chapter 2 (Figs. 4.5 and 4.18) because ϕ has a significant effect on v_c. Hence more attention should be paid to the distribution of velocity, especially v_c, than that of pressure in the study of the yarn suction gun.

4.5 Conclusions

In this chapter, the geometrical effects of yarn suction gun on the flow characteristics have been investigated numerically. Results obtained are as follows:

(1) The compressed-air inflow angle ϕ dominantly determines the circumferential velocity component v_c in the yarn propulsion tube. v_c has the maximum effect on the yarn suction capacity.

(2) The diverging angle of nozzle θ mainly affects the airflow near the throat of the de Laval tube and in the yarn inhalation tube.

(3) The converging angle of de Laval tube α nearly has no effect on the airflow patterns in the yarn suction gun except for throat area.

(4) A reduction in the throat diameter of de Laval tube D causes a rapid extension of supersonic flow area accompanied by an increment in axial velocity component v_z in the de Laval tube. However, it leads to decreases in v_c in the yarn propulsion tube, the air velocity in the yarn inhalation tube and the air density near the wall of the de Laval tube, which hinders the promotion of yarn suction force F_m.

(5) F_m has a close relationship to the distribution of airflow velocity, and depends strongly on v_c.

References

[1] Takenaka Y, Hori K (1975) Spinning apparatus with retractable suction gun. US Patent 4043718

[2] Iemoto Y, Tanoue S, Qiu H (2010), Numerical simulation of effects of size of circular yarn duct of interlacer on airflow patterns. *J Text Eng*, 56, 87-96

[3] Mohamerd M, Salama M (1986) Mechanics of a single nozzle air-jet filling insertion system Part I: Nozzle design and performance. *Text Res J*, **56**, 683-690

[4] Ishida M, Okajima A (1994) Flow characteristic of the main nozzle in an air-jet loom Part I: Measuring flow in the main nozzle. *Text Res J*, **64**, 10-20

[5] Adanur S, Bahfiyarov S (1996) Analysis of air flow in single nozzle air-jet filling insertion: corrugated channel model. *Text Res J*, **66**, 401-406

[6] Shintani R, Okajima A (2002) Air flow through a weft passage of profile reed in air jet looms. *J Text Eng*, **48**, 56-63

[7] Finnemore E. J, Franzini J. B (2003) *Fluid Mechanics with Engineering Applications (10th ed)*, pp600-601, McGraw-Hill Companies, Inc., New York, USA

[8] Kitoh O (1991) Experimental study of turbulent swirling flow in a straight tube. *J Fluid Mech*, **225**, 445-479

[9] Emmons H (1958) *Fundamentals of Gas Dynamics*, p172, Princeton University Press, Princeton, New Jersey, USA

Chapter 5

Yarn Posture in Yarn Suction Gun

List of Symbols

x, y, z	Cartesian coordinates
ϕ	Compressed-air inflow angle
θ	Passage diverging angle of nozzle
α	Converging angle of de Laval tube
D	Throat diameter of de Laval tube
p	Supplied air pressure (gauge pressure)
F_m	Yarn suction force
v	Feed speed of yarn
v_{yc}	Circumferential component of yarn velocity
v_{yz}	Axial component of yarn velocity
v_c	Circumferential component of air velocity
v_z	Axial component of air velocity
L_y	Length of yarn in airflow
δ	Photographing angle
l	Distance from camera lens to yarn

5.1 Introduction

Yarn suction gun is a kind of fluid machinery sucking yarns using high-speed helical airflow. The yarn suction is the result of interaction between the high-speed airflow and the yarn in a yarn passage. Yarn behavior in the airflow has a considerable influence on the yarn suction efficiency because it decides the position and the length of the yarn in the helical airflow with radius-dependent density and velocity. Therefore, clarifying the relation between the yarn behavior and yarn suction force and then controlling the yarn motion appropriately is important for designing new types of the yarn suction gun with high performance. Although the relation can be inferred partly from the information in the previous chapters, they are not satisfying and complete yet. Then it becomes the task of this chapter to clarify them.

As a fundamental experiment to clarify the yarn behavior, in this chapter we will deal with the yarn postures in a yarn passage by analyzing photographs of a running yarn taken with a still camera. Here, the yarn posture means a shape of the yarn centerline in the yarn suction gun. The geometrical effects of the gun on the yarn posture will be investigated. The relation between the yarn posture and the yarn suction force will be also discussed.

5.2 Experiments

5.2.1 Dimension of Yarn Suction Gun and Processing Condition

Figure 5.1 shows the illustration of the yarn suction gun used in this study. The yarn

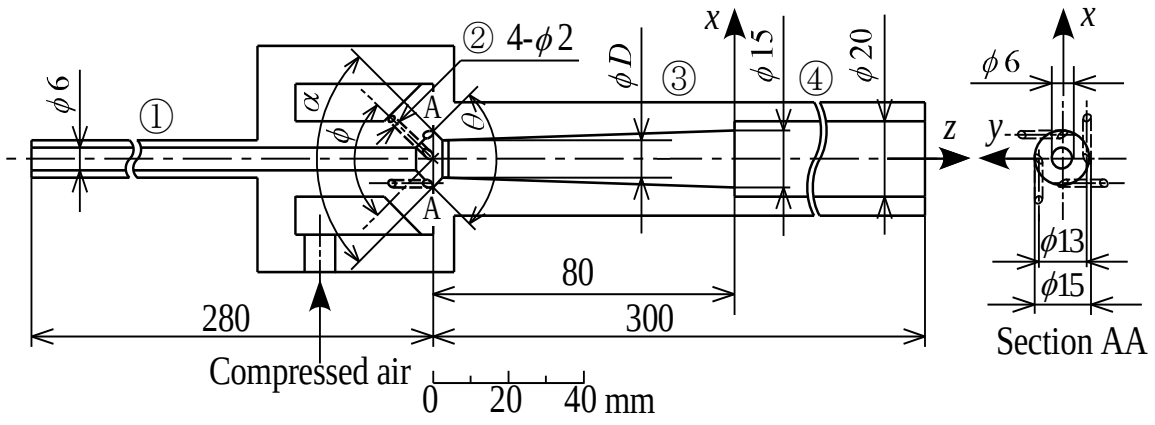

① Yarn inhalation tube ② Four compressed-air inflow tubes in nozzle ③ de Laval tube ④ Straight tube

Figure 5.1 Illustration of yarn suction gun.

propulsion tube, which consists of de Laval tube ③ and straight tube ④, is made of transparent acrylic for measurement of yarn positions. The basic working mechanism and the route of air from a compressor to the suction gun have been described in Chapter 2 and therefore the descriptions of them are omitted here.

In this chapter, the focused geometrical parameters of the yarn suction gun for analysis of the yarn posture are compressed-air inflow angle ϕ, passage diverging angle of nozzle θ, converging angle of de Laval tube α and throat diameter of de Laval tube D shown in Fig. 5.1. Values of the geometrical parameters are shown in Table 5.1. For the purpose of comparability with the previous study in Chapter 2, polyester filament yarn of 166.7 dtex/48 f was used; feed speed of the yarn v and supplied air pressure p were set at 600 m/min and 0.5 MPa (gauge pressure) respectively.

Table 5.1 Geometrical parameters of yarn suction gun

Geometrical parameter	Value
Compressed-air inflow angle ϕ	30, 60, 90, 120, 150, 165°
Passage diverging angle of nozzle θ	30, 60, 90, 120 °
Converging angle of de Laval tube α	60, 90, 120, 150 °
Throat diameter of de Laval tube D	9, 10, 11, 13 mm

5.2.2 Photographing Method

The method of photographing the running yarn in the yarn propulsion tube is shown in Fig. 5.2. The z axis coincides with the centerline of the yarn suction gun, and its origin is located on the boundary between the de Laval tube and the straight tube. A yarn moves in the z direction. It is shot simultaneously form x and y axes with a still camera ⑥ by combination of four mirrors ② ③ ④ ⑤. Since a photograph of two images of the running yarn in xz and yz planes can be obtained, the three-dimensional yarn postures can be measured. This method was used to investigate the yarn motion in an interlacer in interlacing process [1-4].

Figure 5.3 gives an example of the photograph of the running yarn in the yarn suction gun. The yarn position shown in the photograph differs from the real one because of photographing angle and refraction of light passing through the acrylic tube wall. Correcting the measured data eliminated these errors. The detailed method is described in the following section.

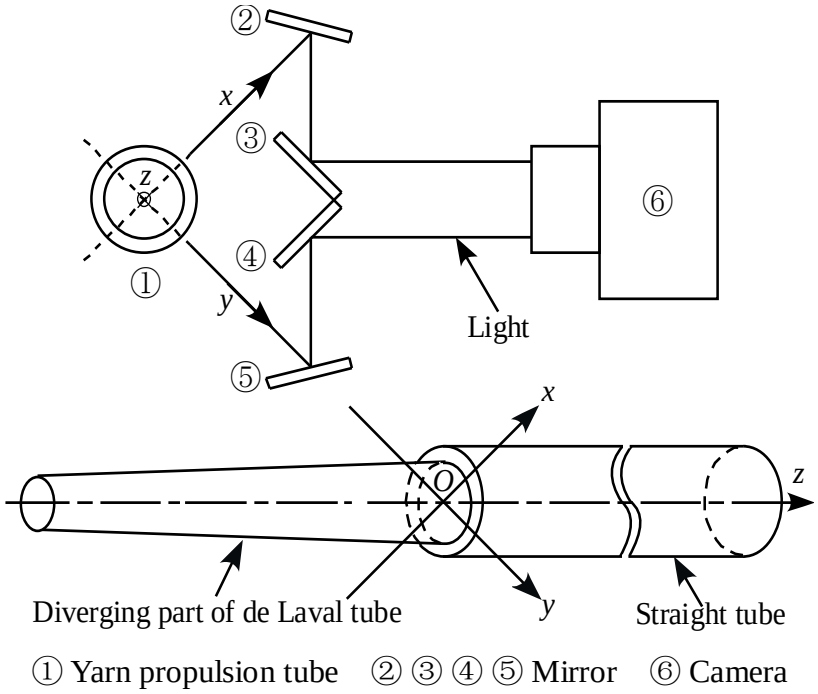

Figure 5.2 Method of photographing the running yarn in yarn suction gun.

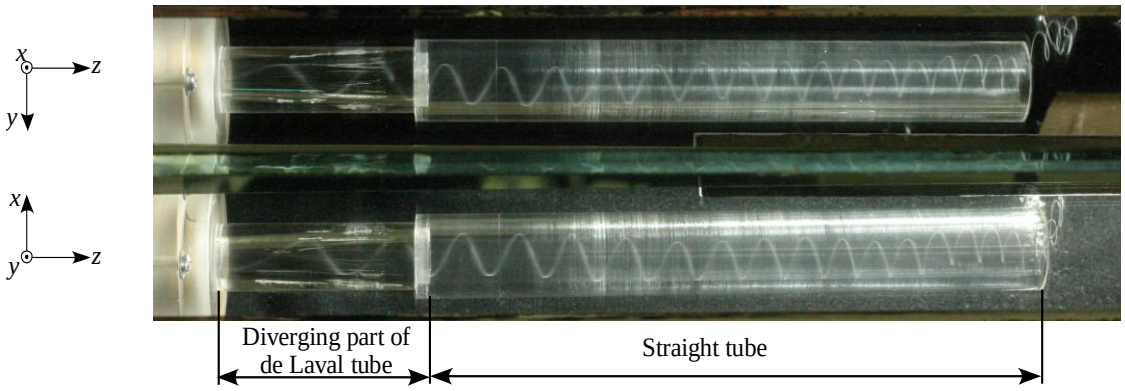

Figure 5.3 Example of photograph of the running yarn in yarn suction gun (ϕ = 150º, θ = 60º, α = 90º and D = 10 mm).

5.2.3 Measurement of Yarn Position

As shown in Fig. 5.4, the left part of an acrylic sheet has the same size as the inner longitudinal section of the yarn propulsion tube through the axis from the throat (z = -77..5 mm) to the exit (z = 220 mm), and was pasted with a graph paper (1×1 mm) so as to keep the graph paper in one plane. This graph paper, therefore, could be inserted into the yarn propulsion tube and rotated on the central axis of the tube. It was kept in *zx* and *zy* planes respectively, and photographed. The two photographed images of graph paper in *zx* and *zy* planes in Fig. 5.5 were used as grid reference.

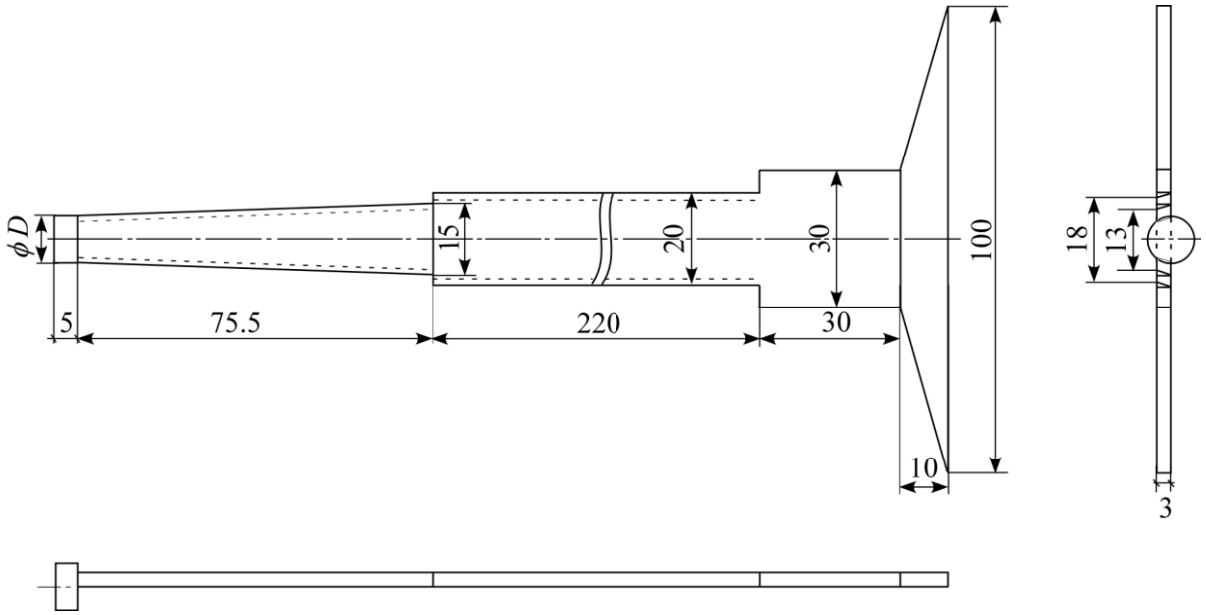

Figure 5.4 Figure scale (unit: mm).

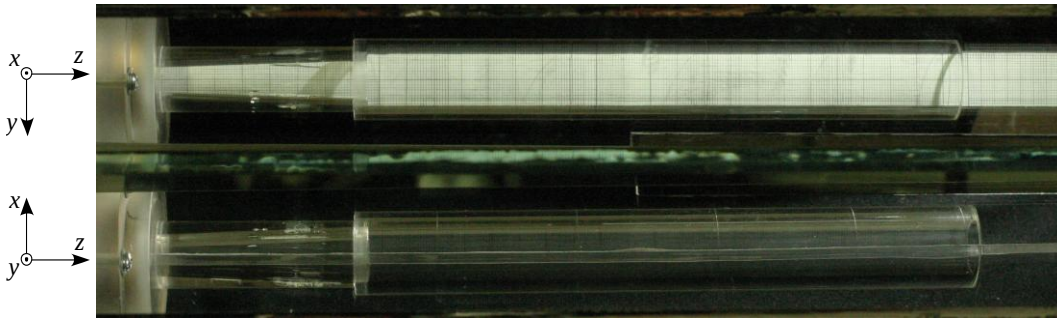

(a) Grid reference in *yz* plane

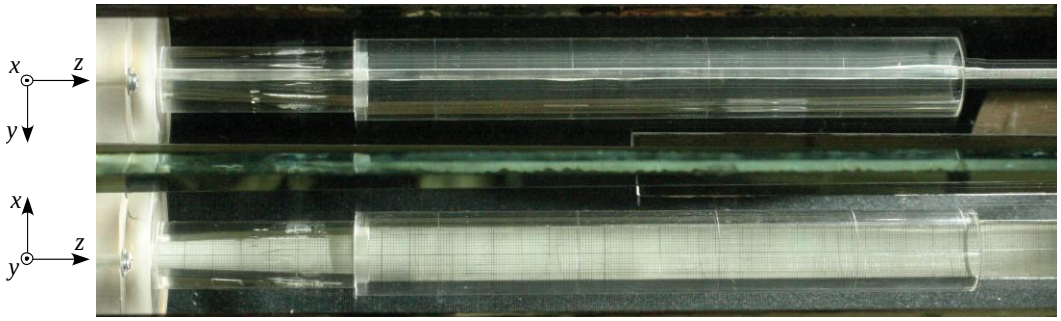

(b) Grid reference in *xz* plane

Figure 5.5 Reference samples.

Superimposing images of the yarn in Fig. 5.3 on the corresponding grid reference in Figs. 5.5(a) and 5.5(b), we got the images shown in Fig. 5.6. Then we can read the coordinates of any segment of the yarn, and therefore eliminate the errors caused by the refraction of light. However, the measured data still have some errors caused by the photographing angle, and the reason is analyzed in the following paragraphs.

As shown in Fig. 5.7, the image of graph paper is in *xz* plane and there exits a photographing angle δ when $z \neq 20$ mm. It is assumed that two short segments of a yarn A and B lie at points A (0, 10, z_1) and B (0, -10, z_1) respectively in *xy* plane at $z = z_1$. Their positions is changed to points A' (0, 0, z_A) and B' (0, 0, z_B) respectively in the photograph owing to δ. Now we can understand why the measured data are different from the actual ones.

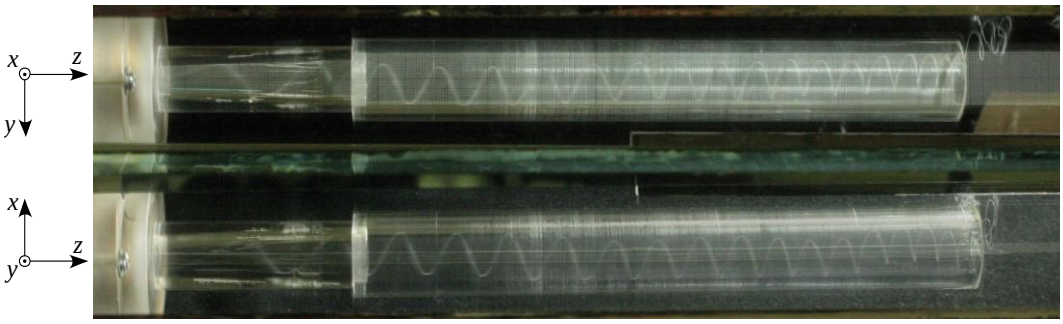

(a) Measure yarn posture in *yz* plane

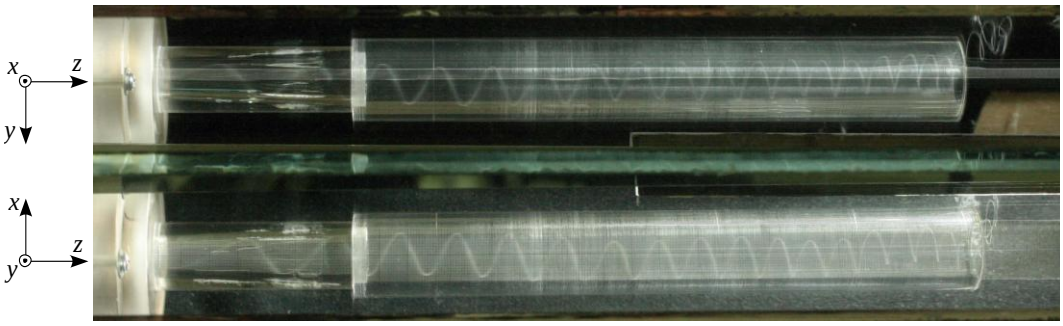

(b) Measure yarn posture in *xz* plane

Figure 5.6 Image after superimposition.

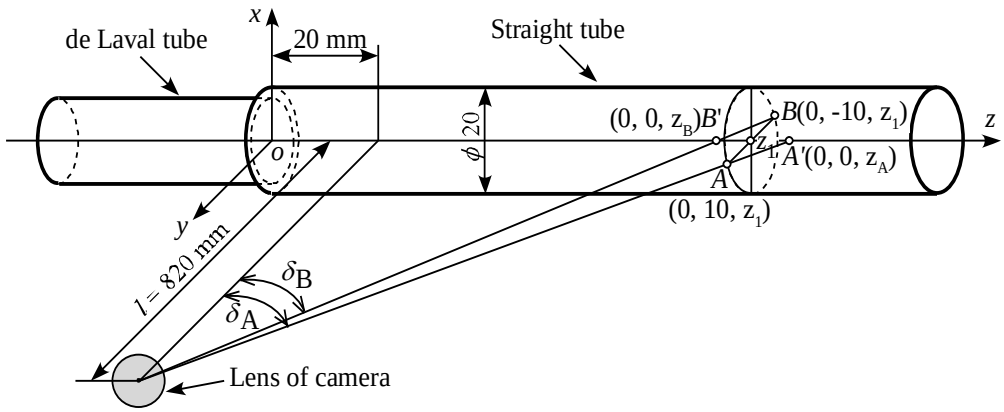

Figure 5.7 A diagrammatic sketch showing the measurement errors.

We give an example to illustrate the correction method for the measured values of yarn position. It is assumed that a short segment of the yarn is located at point A (x, y, z). Its position is changed to point A' (x', y', z'), namely measured position, in the image because of the photographing angle. The distance from the lens center of camera to the z axis is l. Both values of x' and y' are less than the corresponding radius of tube (5-10 mm), which is very small compared with l (= 820 mm). Thus errors of x' and y' can be ignored because of small photographing angle ($\leqslant$ 0.7°). Then, we can get

$$x = x' \tag{5.1}$$

$$y = y' \tag{5.2}$$

Only the effect of the photographing angle on the measured value of z' is considered. Normal line of the camera lens is through the point (0, 0, 20 mm) and there exits a photographing angle δ when $z \neq 20$ mm, as shown in Fig. 5.8. The yarn is photographed from the y direction and then we can get an image of the yarn posture in zx plane, where $y' = 0$ mm. When $y > 0$ mm and $z > 20$ mm,

$$\frac{l}{z'-20} = \frac{y}{z'-z}$$

Rearranging: $z = (1-\frac{y}{l}) \cdot z' + 20\frac{y}{l}$

Using $y = y'$, we obtain

$$z = (1-\frac{y'}{l}) \cdot z' + 20\frac{y'}{l} \tag{5.3}$$

Likewise, we can get the same equation as Eq. (5.3) when $y < 0$ mm and $z > 20$ mm.

It has been proved that Eq. (5.3) is also suitable when $z < 0$.

Therefore, the actual coordinates of a small segment of the running yarn can be obtained by correcting the measured ones using Eqs. (5.1), (5.2) and (5.3).

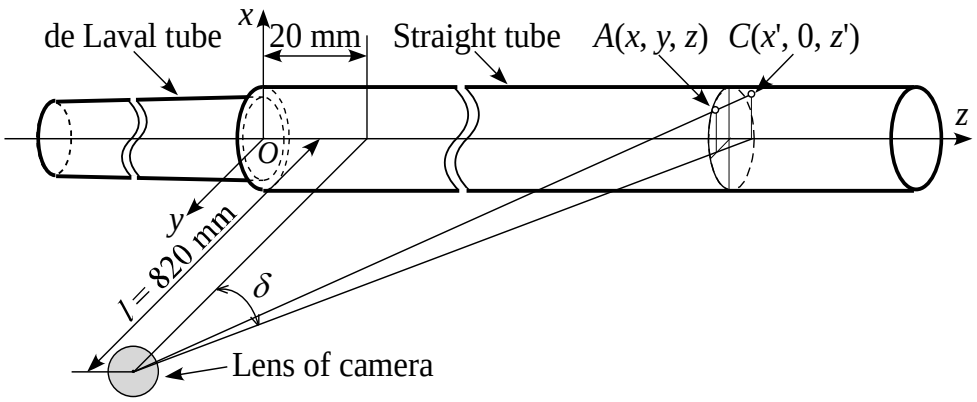

Fig. 5.8 Correction of measured position values.

Figure 5.9 illustrates the difference between the measured and corrected data. It can be seen that the measurement error increases with z. The yarn posture in a photograph slightly differs from the real one.

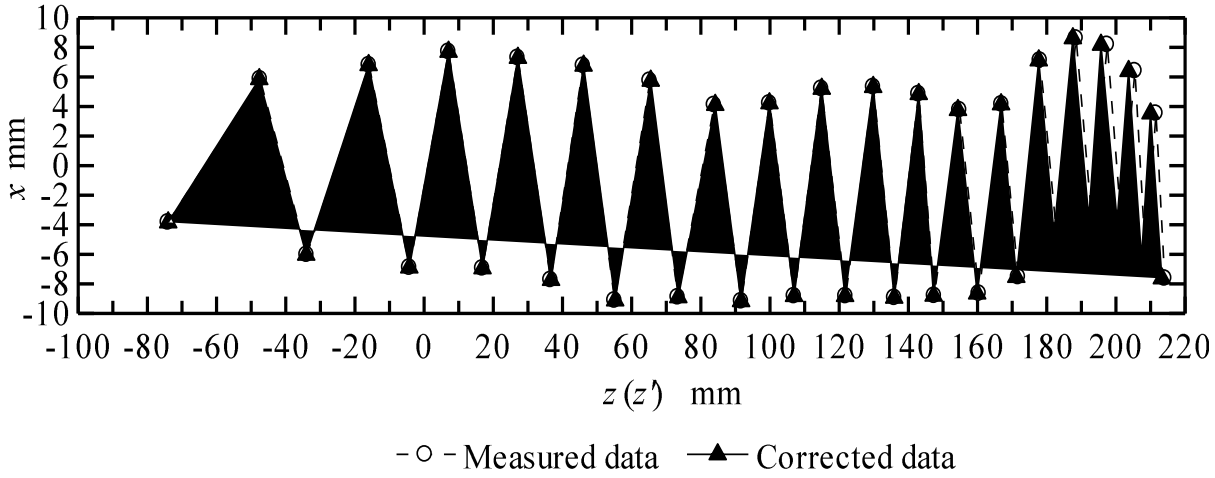

Figure 5.9 Measured and corrected data.

5.3 Results and Discussion

An example of the photograph of the running yarn in the yarn suction gun has been given in Fig. 5.3. Experiments were conducted with the gun with $\phi = 150^{\circ}$, $\theta = 60^{\circ}$, $\alpha = 90^{\circ}$ and $D = 10$ mm, with which the largest suction efficiency was obtained in Chapter 2. The yarn moves in a helix in the yarn propulsion tube as shown in Fig. 5.3. It is similar to the streamline of the compressed air injected into the yarn propulsion tube (see Fig. 3.21). Such airflow causes the entrained yarn to possess an axial component of motion directing towards the rear of the straight tube, as well as a circumferential component of motion along the wall of the yarn propulsion tube. In particular, it has higher density and higher speed near the wall than near the center so as to efficiently produce air drag on the yarn. This is a characteristic of the yarn suction gun used in the present research. With this design, only a small amount of compressed air is needed to produce high propulsion force to effectively suck and discharge a yarn running at high speed. A large amount of energy can therefore be saved.

We can determine the position of any segment of the running yarn in the yarn propulsion tube using such photographs. Helix diameter d_y and helix pitch p_y of yarn posture defined in Fig. 5.10 will be used to characterize the yarn posture in this study. As shown in Fig. 5.10, d_y is the helix diameter at $z = z_d$ where the helix peak B is located; p_y is the distance

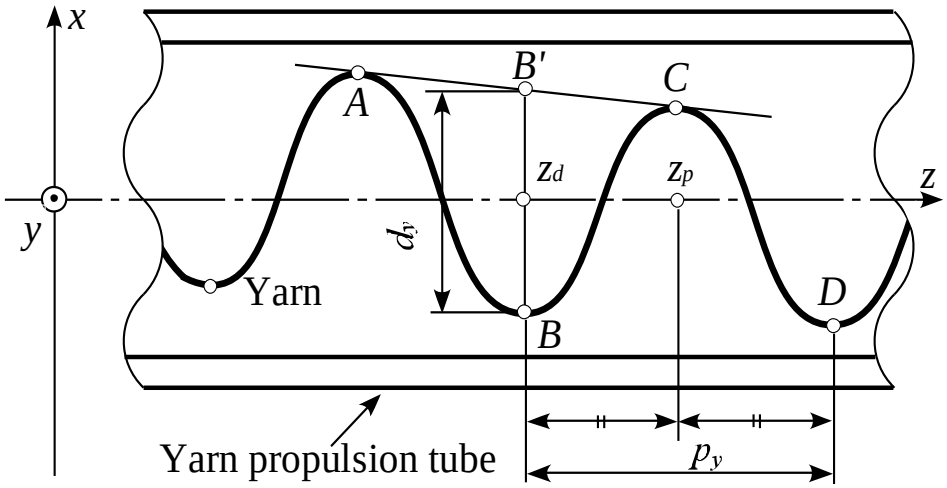

Figure 5.10 Definitions of helix diameter of yarn posture d_y and helix pitch of yarn posture p_y.

in the z direction between two adjacent helix peaks B and D, where $z = z_p$ is at the axial mid-position of two peaks B and D. For one case, five photographs were taken at about 1 s intervals. d_y and p_y were determined using average values of the helix diameter and helix pitch of yarn posture in these five photographs respectively.

5.3.1 Effect of Compressed-air Inflow Angle ϕ on Yarn Posture

Figure 5.11 shows the results of yarn postures in the yarn suction guns with different compressed-air inflow angle ϕ. The other three geometrical parameters are fixed at $\theta = 60^o$, $\alpha = 90^o$ and $D = 10$ mm.

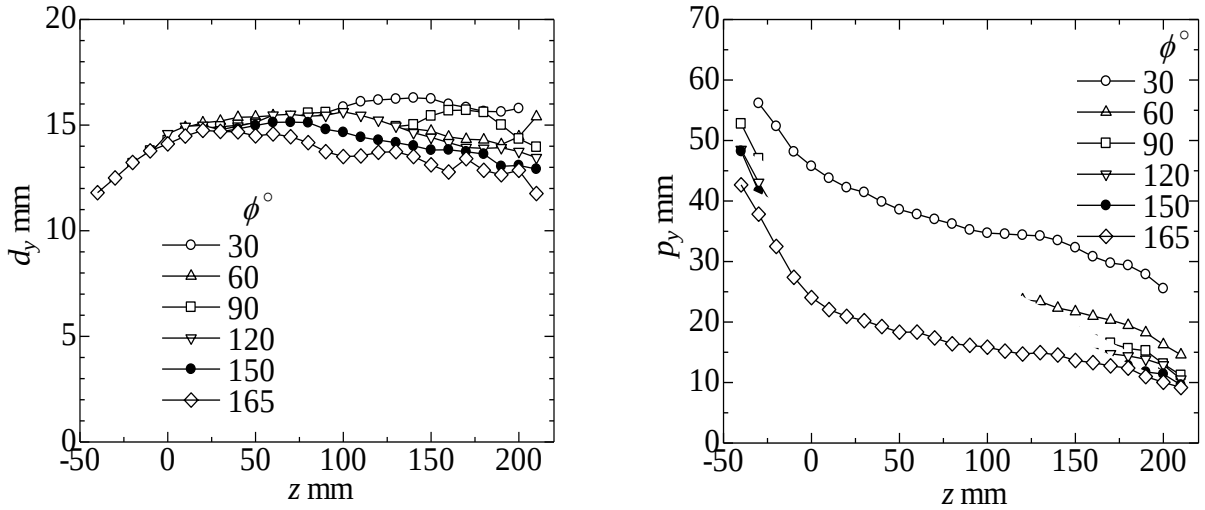

(a) Helix diameter of yarn posture d_y (b) Helix pitch of yarn posture p_y

Figure 5.11 Yarn postures in yarn suction guns with different compressed-air inflow angle ϕ ($\theta = 60^o$, $\alpha = 90^o$ and $D = 10$ mm).

Firstly, we discuss the yarn posture in the yarn suction gun according to Fig. 5.3 and the profiles at ϕ = 150º shown in Fig. 5.11. Helix diameter of yarn posture d_y increases with z in the de Laval tube (z < 0 mm), keeps nearly constant in the upstream region of the straight tube, and decreases with increasing z in the downstream region. Helix pitch of yarn posture p_y decreases with increasing z in the yarn propulsion tube, especially undergoing a rapid, large reduction in the de Laval tube, because the airflow swirl intensity [5, 6], which indicates the intensity of swirling motion, decays gradually. In the de Laval tube, the air drag exerted on the yarn is large enough to make the yarn move along the wall. Therefore, the value of d_y with respect to z is equal to the corresponding inner diameter of the de Laval tube. The yarn does not keep moving along the inner wall of the straight tube when d_y is smaller than the tube inner diameter of 20 mm. This is because the strength of the helical flow decreases as the air goes downstream in the straight tube, and this weak helical flow cannot keep the yarn moving forward with rotation along the tube wall any more, as well as easily suffering the disturbance from the running yarn. Hence the yarn running condition becomes worse, which is marked by the fluctuation, i.e. an irregular rising and falling, in d_y in the z direction shown in Fig. 5.11(a) caused by the unsteady weak helical airflow in the straight tube downstream. The quite large gradients of p_y in the de Laval tube are generated because the air velocity drops rapidly owing to the normal shock wave in the de Laval tube.

In the de Laval tube, the helical airflow is so strong to draw the running yarn into the high-speed and high-density flow area near the wall, and hence there is little difference in the distributions of d_y at varied ϕ as shown in Fig. 5.11(a). In the straight tube, d_y decreases roughly with increasing ϕ; the dependence of d_y on ϕ is small and is further weakened by the fluctuation in d_y. Large fluctuations in d_y exist in the yarn suction guns with unfavorable values of geometrical parameters (for example, ϕ = 60, 90º) where helical airflows of small strength are produced. The fluctuation in d_y reveals the instability of the yarn motion, which increases the chance of touching the inner wall of tube for a running yarn, and then increases the yarn moving resistance. This results in a decrease in the yarn suction force F_m.

p_y decreases with an increase in ϕ as shown in Fig. 5.11(b). The reduction in p_y, namely the increase in the yarn angle with respect to the tube axis, is caused by an increase in the circumferential component of yarn velocity v_{yc} because the circumferential component of air velocity v_c increases with ϕ as obtained in Chapter 4.

We will discuss the effects of ϕ on the yarn posture and the yarn suction force F_m. The values of d_y and p_y decrease with an increase in ϕ (Fig. 5.11). F_m increases to the maximum

value at ϕ = 150º and then decreases as ϕ increases (Fig. 4.5). Thus decreases in d_y and p_y cause F_m to increase. Here, a small p_y increases the length of the yarn in the airflow L_y and therefore causes an increase in the friction between the air and the yarn surface, i.e. F_m, which increases with L_y [7, 8]. A small d_y may considerably decrease the friction between the yarn and the tube wall. Thus appropriately small d_y promotes F_m by decreasing the friction on the tube wall, and makes the yarn motion stable by reducing the yarn retardation from wall friction. The large fluctuation in d_y at ϕ = 165° reveals the large instability of the yarn motion, which leads to a decrease in F_m although both d_y and p_y are small in this case.

5.3.2 Effect of Passage Diverging Angle of Nozzle θ on Yarn Posture

The results of yarn postures are shown in Fig. 5.12 showing plots of helix diameter of yarn posture d_y and helix pitch of yarn posture p_y at different passage diverging angle of nozzle θ. The values of ϕ, α and D are fixed at 150º, 90º and 10 mm respectively. On the whole, both d_y and p_y increase with θ. However, the relationship between d_y and θ becomes unstable in the downstream region of the straight tube because of the fluctuations in d_y, and the dependency of p_y on θ is also small. Therefore, θ has a small influence on the yarn motion in the yarn propulsion tube. It implies that the airflow in the yarn propulsion tube is hardly affected by θ, which has been confirmed in Chapter 4.

Yarn suction force F_m decreases when θ is increased from 60º to 120º, but the variation in F_m is small, as presented in Fig. 4.10. F_m is just a little smaller at θ = 30º than at θ = 60º.

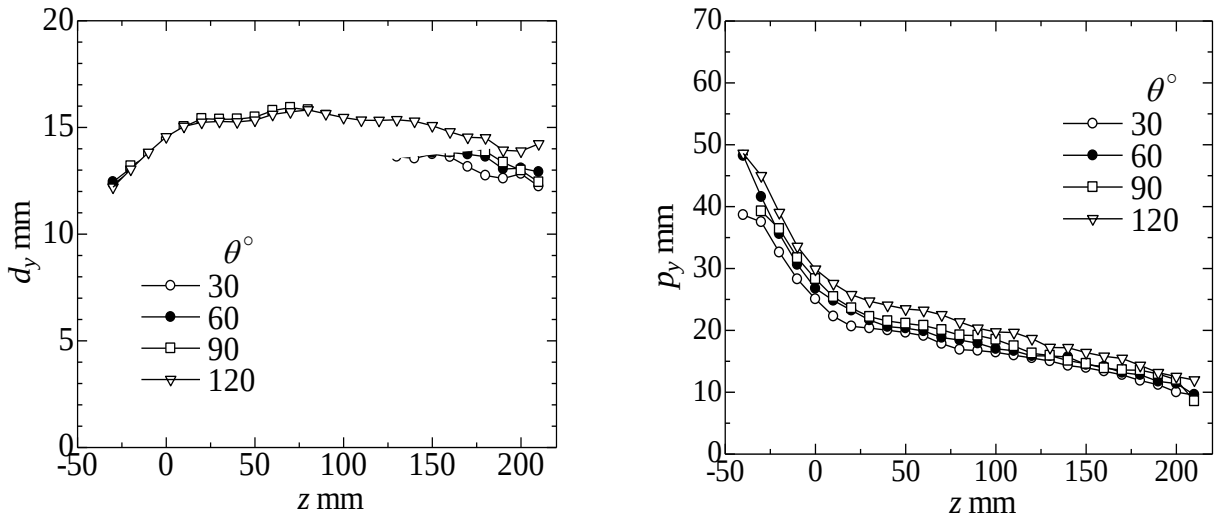

(a) Helix diameter of yarn posture d_y

(b) Helix pitch of yarn posture p_y

Figure 5.12 Yarn postures in yarn suction guns with different passage diverging angle of nozzle θ (ϕ = 150º, α = 90º and D = 10 mm).

The relation between F_m and the characteristic values of yarn posture obtained in this section are similar to those in Sec. 5.3.1.

5.3.3 Effect of Converging Angle of de Laval Tube α on Yarn Posture

Figure 5.13 presents the results of yarn postures in the yarn suction guns with different converging angle of de Laval tube α, fixing ϕ, θ and D at 150º, 60º and 10 mm respectively. The fluctuations in the helix diameter of yarn posture d_y make specifying the dependency of d_y on α impossible; however, the variation in d_y with z can be found rather smooth at $\alpha = 90°$ in Fig. 5.13(a). Furthermore, the variation in the helix pitch of yarn posture p_y with α is so small. As a result, the behavior of the running yarn seems to be almost independent of α so that the effect of α on the airflow in the yarn suction gun is of no importance, which agrees with the simulated results in Chapter 4. We can now understand why the variation of F_m with α is small, as depicted in Chapter 2.

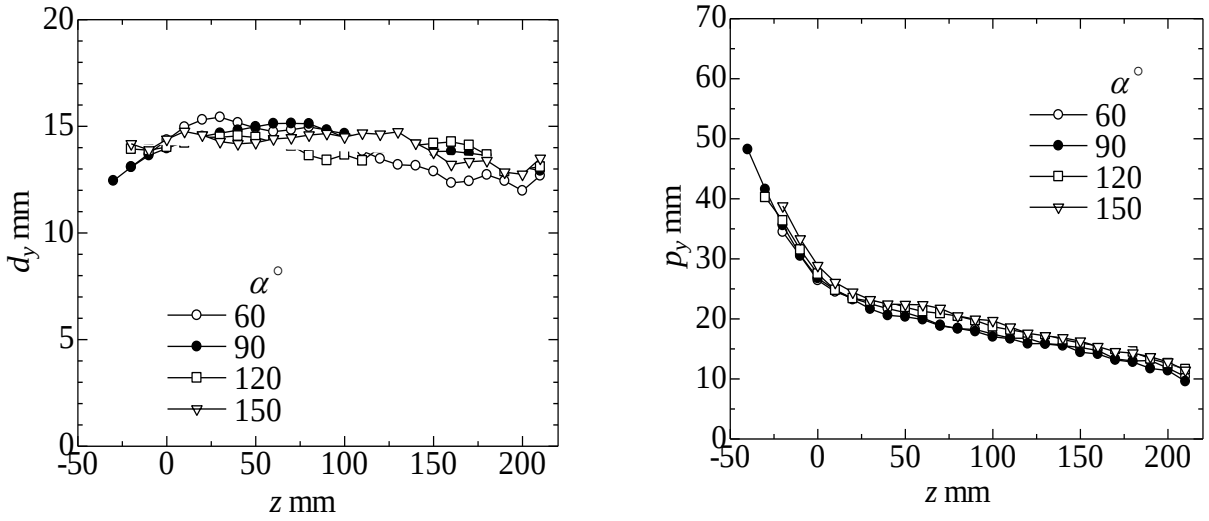

(a) Helix diameter of yarn posture d_y (b) Helix pitch of yarn posture p_y

Figure 5.13 Yarn postures in yarn suction guns with different converging angle of de Laval tube α (ϕ = 150º, θ = 60º and D = 10 mm).

5.3.4 Effect of Throat Diameter of de Laval Tube *D* on Yarn Posture

The results of yarn postures at different throat diameter of de Laval tube D are shown in Fig. 5.14. We fix ϕ, θ and α at 150º, 60º and 90º respectively, varying D from 9 to 13 mm. Both helix diameter of yarn posture d_y and helix pitch of yarn posture p_y decrease with decreasing D. The dependencies of d_y and p_y on D are comparatively larger than on the other three geometrical parameters; this indicates that D has the most considerable effect on the airflow in

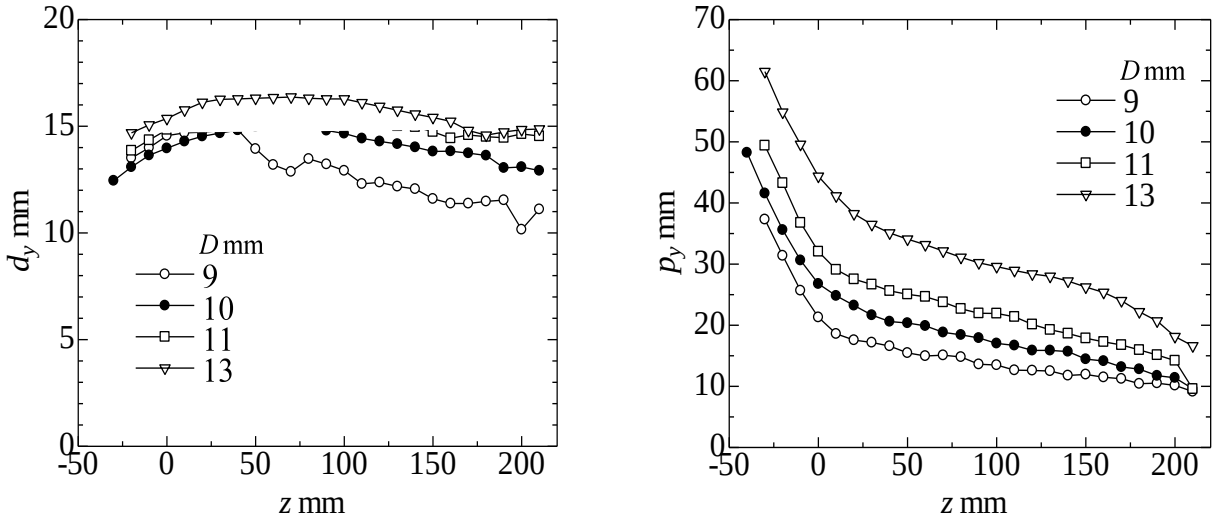

(a) Helix diameter of yarn posture d_y (b) Helix pitch of yarn posture p_y

Figure 5.14 Yarn postures in yarn suction guns with different throat diameter of de Laval tube D (ϕ = 150º, θ = 60º and α = 90º).

the yarn suction gun, which can also be seen from Chapter 4. At D = 9 mm, d_y is rather small and the yarn may be, therefore, located near or in the core region of the helical flow most of the time, wherein air density, and axial component v_z and circumferential component v_c of air velocity are smaller than those in the annular region of the helical flow. This may cause the yarn suction force F_m to decrease.

As D decreases from 13 to 9 mm, v_z in the de Laval tube increases rapidly with decreasing D accompanied by slightly decreasing v_c (Fig. 4.17). The ratio of v_c to v_z decreases with decreasing D in the yarn propulsion tube, and hence p_y will increase in theory. However, the tendency of p_y with respect to D in Fig. 5.14(b) does not coincide with the above-mentioned theory. Large changes in v_z do not produce marked changes in p_y. Thus p_y may have little relation to v_z and strongly depends on v_c. This also agrees with the results in Sec. 5.3.1 that p_y is significantly affected by ϕ, which plays an important role in generating the helical flow by controlling v_c as pointed out in Chapter 4.

Yarn suction force F_m increases as D is decreased from 13 to 10 mm, and it is a little smaller at D = 9 mm than at D = 10 mm (Fig. 4.18), which may relate to too small values of d_y and the large fluctuation in d_y in the straight tube shown in Fig. 5.14(a). Thus F_m increases with decreasing d_y and p_y in general. The similar trend exists in other two cases as discussed in Secs. 5.3.1 and 5.3.2.

5.4 Conclusions

To clarify the yarn posture in a yarn suction gun, transparent suction guns were made and a running yarn was photographed with a still camera. The postures of the running yarn were analyzed by processing yarn positions. The relations between the geometry of the suction gun, the yarn posture and the yarn suction force were discussed. By the experiments, the effects of geometrical parameters on the yarn posture and the relation between the yarn posture and the yarn suction force have been cleared up as follows.

(1) Both helix diameter of yarn posture d_y and helix pitch of yarn posture p_y decrease with an increase in the compressed-air inflow angle ϕ and a decrease in the throat diameter of de Laval tube D, which cause an increase in the yarn suction force F_m.

(2) d_y and p_y are almost independent of the passage diverging angle of nozzle θ and the converging angle of de Laval tube α.

(3) A rational design of the yarn suction gun can produce a stable yarn motion condition with appropriately small d_y, which reduces yarn moving resistance from tube wall, and small p_y, which increases the length of the yarn in the airflow. This greatly promotes F_m.

(4) In comparison with the axial component of air velocity, the circumferential component of air velocity has a considerable effect on the yarn posture.

References

[1] Iemoto Y, Chono S, Tanaka T (1998) Study on interlaced yarn Part 4: Yarn posture in interlacer, and relation between yarn postures and number of tangles. *J Text Mach Soc Japan* (predecessor journal of *J Text Eng*), **44**, 57-63

[2] Iemoto Y, Chono S, Tanaka T (1999) Study on interlaced yarn Part 6: Yarn motion in interlacer. *J Text Mach Soc Japan* (predecessor journal of *J Text Eng*), **45**, 44-50

[3] Chono S, Iemoto Y (1999) Study on interlaced yarn Part 7: Yarn motion in interlacer and production mechanism of tangling part. *J Text Mach Soc Japan* (predecessor journal of *J Text Eng*), **45**, 108-112

[4] Qiu H, Iemoto Y and Tanoue S (2007) Yarn motion in interlacers with various cross-sectional shapes of yarn duct. *J Text Eng*, **53**, 59-67

[5] Kitoh O (1991) Experimental study of turbulent swirling flow in a straight tube. *J Fluid Mech*, **225**, 445-479

[6] Slavyanov N (1973) Theoretical study of the swirling flows of an ideal gas in a Laval nozzle. *Fluid Dynamics*, **8**, 920-925

[7] Adanur S, Bakhtiyarov S (1996) Analysis of air flow in single nozzle air-jet filling insertion: corrugated channel model. *Text Res J*, **66**, 401-406

[8] Finnemore E. J, Franzini J. B (2003) *Fluid Mechanics with Engineering Applications (10th ed)*, pp374-375, McGraw-Hill Companies, Inc., New York, USA

Chapter 6

Yarn Motion in Yarn Suction Gun

List of Symbols

x, y, z	Cartesian coordinates
ϕ	Compressed-air inflow angle
θ	Passage diverging angle of nozzle
α	Converging angle of de Laval tube
D	Throat diameter of de Laval tube
v	Yarn feed speed
p	Supplied air pressure (gauge pressure)
t	Time
Δz	Yarn covered distance
ω_y	Angular velocity of yarn
v_y	Yarn velocity
v_{yc}	Circumferential component of yarn velocity
v_{yz}	Axial component of yarn velocity
r_y	Helix radius of yarn trajectory
d_y	Helix diameter of yarn posture
p_y	Helix pitch of yarn posture
v_c	Circumferential component of air velocity
v_z	Axial component of air velocity
F_m	Yarn suction force

6.1 Introduction

Yarn behavior in the airflow has a significant effect on the yarn suction efficiency of a yarn suction gun. As a fundamental experiment for analysis of the yarn behavior in the gun, in Chapter 5 we have investigated yarn postures by analyzing photographs of a running yarn taken with a still camera, and clarified the geometrical effects of the gun on the yarn posture and the relationship between the yarn posture and the yarn suction force.

However, yarn motion, i.e. yarn position as a function of time, is indispensable for analyzing the yarn behavior, which is considered an important issue for clarifying the working mechanism of the yarn suction gun. In this chapter we will investigate the motion of a running yarn in different regions of a yarn suction gun and the geometrical effects of the gun on the yarn motion with a high-speed video camera. The objective of this research is to discover the mechanism of yarn suction, and the relations between the yarn motion, the geometrical parameters and the yarn suction efficiency.

6.2 Experiments

Figure 1 illustrates the yarn suction gun used in this study. Yarn propulsion tube, which consists of de Laval tube ③ and straight tube ④, is made of transparent acrylic for measurement of yarn positions.

The basic working mechanism and the route of air from a compressor to the yarn suction gun have been described in Chapter 2 and therefore the descriptions of them are omitted here.

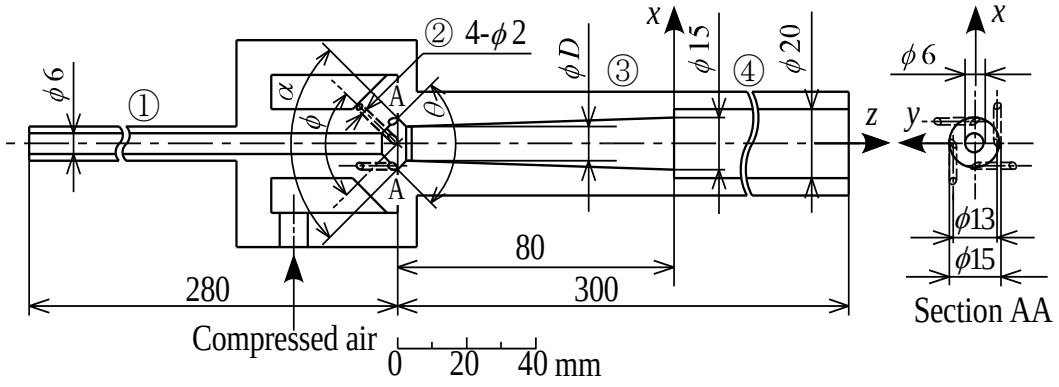

① yarn inhalation tube ② four compressed-air inflow tubes in nozzle ③ de Laval tube ④ straight tube

Figure 6.1 Schematic diagram of yarn suction gun.

In this chapter, we will limit consideration to four geometrical parameters of the yarn suction gun: compressed-air inflow angle ϕ, passage diverging angle of nozzle θ, converging angle of de Laval tube α and throat diameter of de Laval tube D, as shown in Fig. 6.1. Values of the geometrical parameters are given in Table 6.1. For the purpose of comparability with the previous study in Chapter 2, polyester filament yarn of 166.7 dtex/48 f was used; feed speed of the yarn v and supplied air pressure p were set at 600 m/min and 0.5 MPa (gauge pressure) respectively.

The method of photographing the running yarn in the yarn propulsion tube is shown in Fig. 6.2. Details of the photographing device and method have been given in Chapter 5, and therefore are omitted in this chapter except that a high-speed video camera (Trouble Shoter HR, Fastech Imaging, Inc. Canada) was used in place of a still camera. This method also has been used to investigate the yarn motion in an interlacer in interlacing process [1-4].

Table 6.1 Geometrical parameters of yarn suction gun

Geometrical parameter	Value
Compressed-air inflow angle ϕ	120, 150, 165°
Passage diverging angle of nozzle θ	30, 60, 90°
Converging angle of de Laval tube α	60, 90, 120°
Throat diameter of de Laval tube D	9, 10, 11 mm

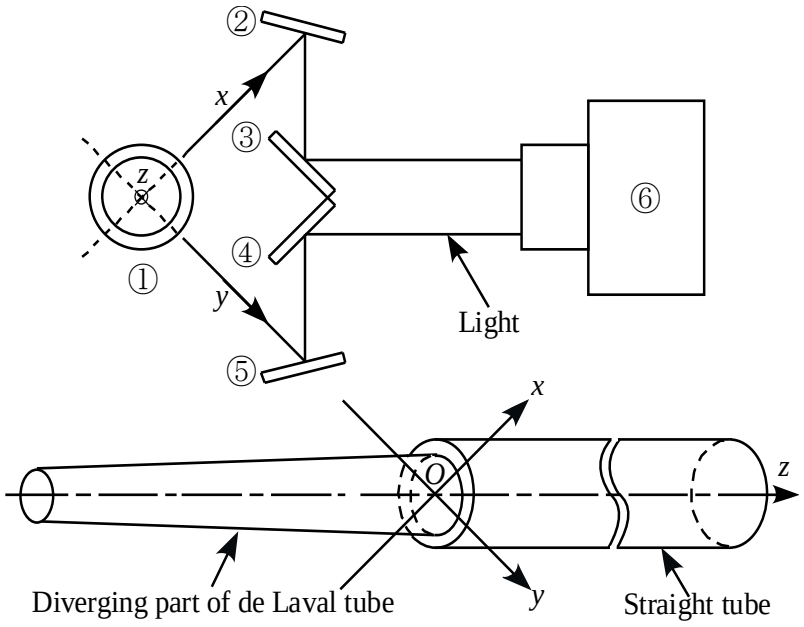

①Yarn propulsion tube ② ③ ④ ⑤ Mirror ⑥ High-speed video camera

Figure 6.2 Method of photographing the running yarn in yarn suction gun.

We read the coordinates of a marked yarn segment in a photograph. Then, the yarn motion was traced by measuring the position of the yarn segment in each frame. The record rate of the video camera was set at 16000 fps.

The yarn position shown in the photograph differs from the real one because of a photographing angle and refraction of light passing through the acrylic duct wall.

A detailed description of the measurement method for determining the yarn position has been given in Chapter 5, and therefore is omitted here.

6.3 Results and Discussion

Figure 6.3 gives a photograph of the running yarn in the region of z = -40 ~ -20 mm, where is in the middle of the de Laval tube. Experiments were performed with the yarn suction gun with ϕ = 150°, θ = 60°, α = 90° and D = 10 mm. A marked yarn segment can be seen in the photograph. We are able to address the motion of a yarn as it moves through a given region by measuring the position of the yarn segment in each frame.

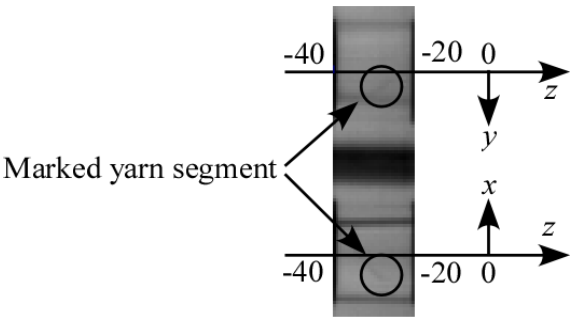

Figure 6.3 Example of the photograph of the running yarn in yarn suction gun (ϕ = 150°, θ = 60°, α = 90° and D = 10 mm).

6.3.1 Whole Characteristics of Yarn Motion in Yarn Suction Gun

Figure 6.4 shows the yarn position (x, y) as a function of time t in four regions where z = -40 ~ -20, 0 ~ 20, 100 ~ 120 and 190 ~ 210 mm respectively. The abscissa t is the elapsed time when the marked yarn segment begins to enter the cross-sections at z = -40, 0, 100 and 190 mm respectively. These figures reveal that the yarn position varies rapidly and the yarn vibrates violently when it moves through the yarn suction gun. In the de Laval tube (z < 0 mm) the yarn position varies regularly; in the straight tube(z > 0 mm), however，it shows larger irregularity of helix diameter and helix pitch, the width of one complete helix turn measured along the helix axis. This implies that air distribution varies considerably in the yarn suction gun and greatly affects the yarn motion.

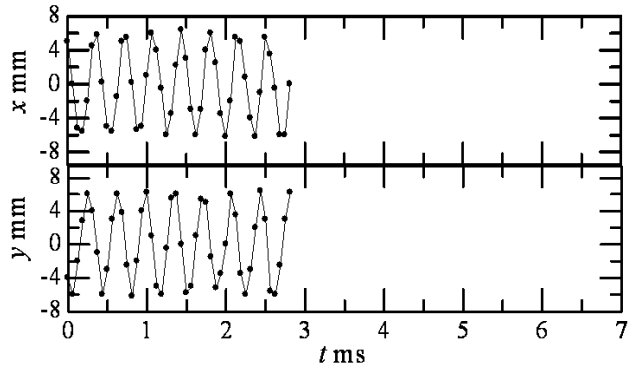

(a) z = -40 ~ -20 mm

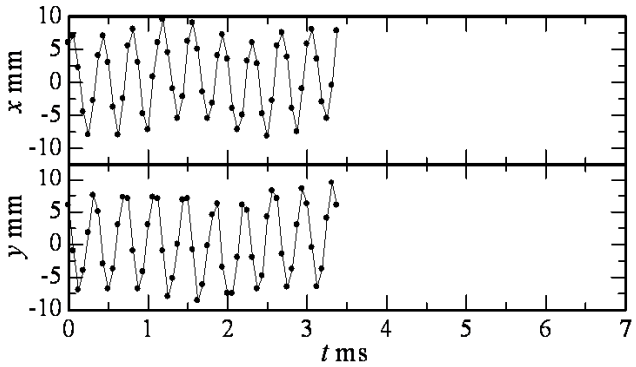

(b) z = 0 ~ 20 mm

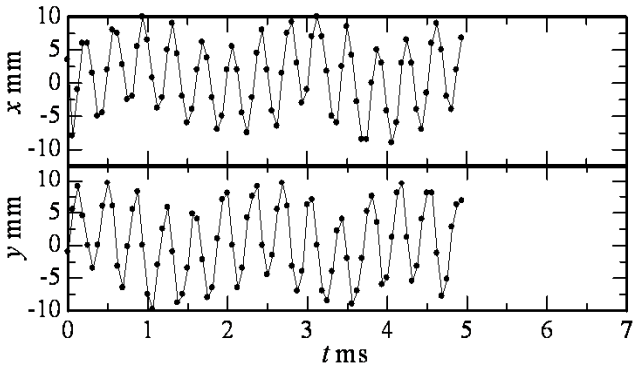

(c) z = 100 ~ 120 mm

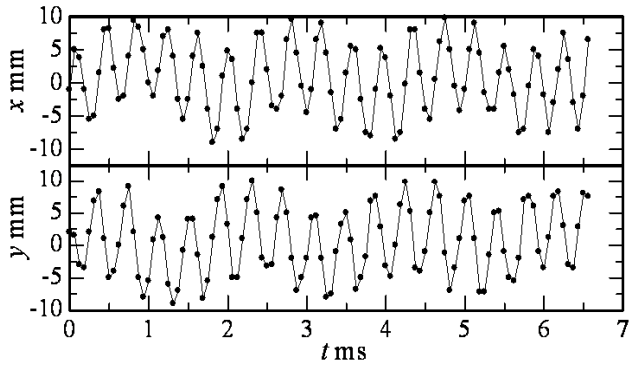

(d) z = 190 ~ 210 mm

Figure 6.4 Yarn positions in x and y directions as a function of time t (ϕ = 150°, θ = 60°, α = 90° and D = 10 mm).

Yarn trace in the circumferential direction of the yarn propulsion tube is shown in Fig. 6.5. Large circles represent the inner walls of the de Laval tube and the straight tube. The center of small circle indicates the yarn position; the number in each small circle gives the order of the yarn positions, and the increment of 1 means time progress of 1/16000 s. It rotates anticlockwise when moving in the direction of *z* axis, as shown in Fig. 6.5. From Figs. 6.4 and 6.5, we see that the yarn moves in a helical motion and the locus of the yarn motion in the de Laval tube is a conic helix, which is defined as a spiral on a conic surface. The air flows with a circumferential velocity component as well as an axial one in the yarn propulsion tube. It is for this reason that a yarn follows a helical path. However, the circumferential and axial velocity components of the running yarn are not constant owing to the decay of the swirl intensity [5]. It is impossible for us to give an exact equation of the yarn motion in the yarn suction gun. The yarn motion depends on positions in the yarn suction gun. For example, it varies with the distance from the throat of the de Laval tube (hereafter the throat). The dependence becomes large when the yarn is located near the throat. The yarn performs a helical motion more regularly in the de Laval tube than in the straight tube, as shown in Figs. 6.4 and 6.5.

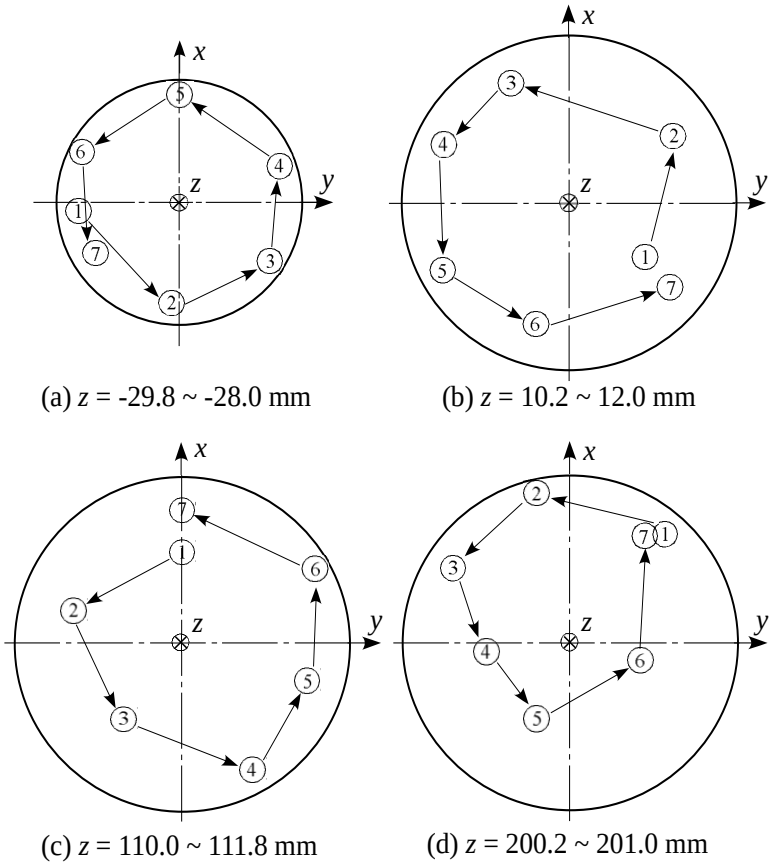

Figure 6.5 Yarn trace in circumference of yarn suction gun (ϕ = 150°, θ = 60°, α = 90° and D = 10 mm).

Figure 6.6 illustrates yarn positions in the circumferential direction of the yarn propulsion tube. Some yarn positions overlap each other in the figure. The yarn mostly moves along the inner wall of the de Laval tube, as shown in Fig. 6.6(a). The distribution of the yarn position performs less regularly with an increase in *z*. Most of the time, the yarn does not move along the inner wall of the straight tube most of the time.

The helical airflow in the straight tube is not strong as that in the de Laval tube to keep the yarn in stable helical motion in the vicinity of the wall, as shown in Figs. 6.4-6.6.

From Figs. 6.6(a)-(d), we get the average values of the helix radius in the four regions, r_y = 6.2, 7.5, 7.6, and 7.1 mm respectively. The high irregularity of yarn position (Figs. 6.6(c) and (d)) causes a larger error in our calculations of r_y in the downstream region of the straight tube.

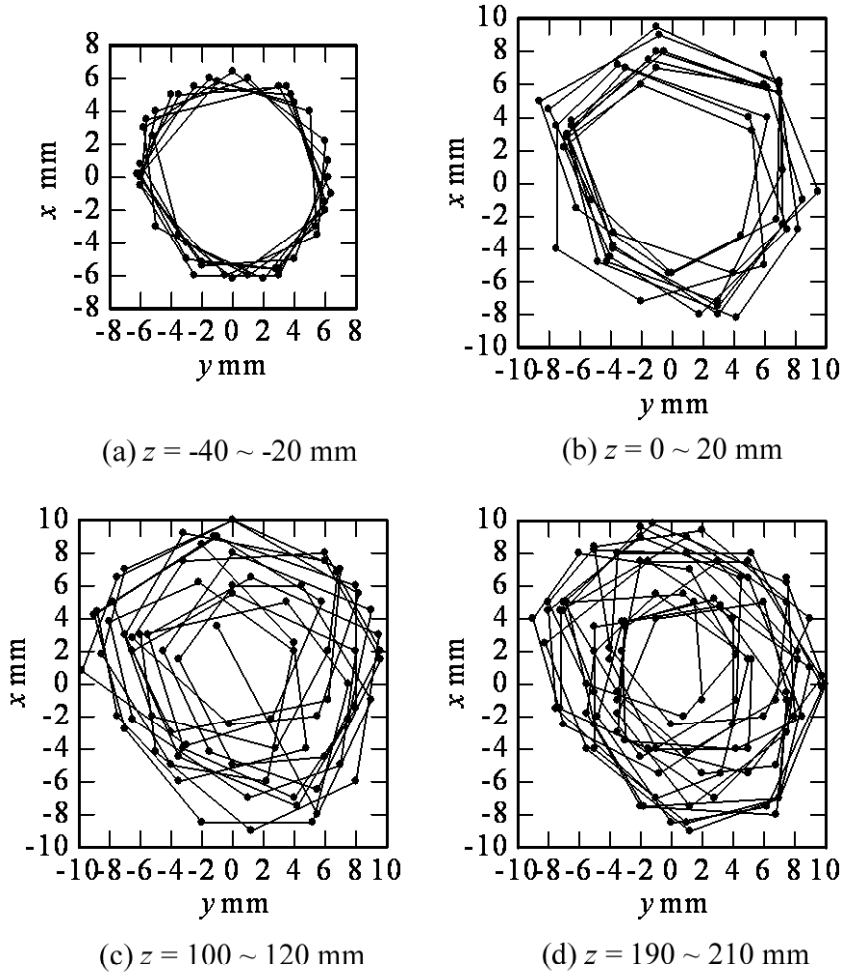

Figure 6.6 Yarn positions in the circumferential direction of yarn suction gun (ϕ = 150°, θ = 60°, α = 90° and D = 10 mm).

Figure 6.7 shows the yarn covered distance Δz as a function of time t. The fluctuation in Δz demonstrates that the yarn moves forward and backward periodically in the direction of z - axis. The air drag exerted on a yarn depends on the interaction between the yarn surface and air. The helical flow in the yarn suction gun is turbulent and unsteady. A distinguishing characteristic of turbulence is its irregularity. Turbulent flow is characterized by fluctuations in velocity at all points of the flow field [6]. The walls are not absolutely smooth; this contributes to the formation of turbulence [7]. The yarn geometrical structure is fundamentally irregular and flexible [8]. The yarn decelerates rapidly when frictionally touching the tube wall. These further complicated the yarn motion.

From Figs. 6.4 and 6.7, we obtain Fig. 6.8(a) showing the mean yarn axial velocity v_{yz} and the mean angular velocity ω_y in four regions of the yarn suction gun. v_{yz} decreases monotonously with an increase in z, while ω_y shows little change.

We change Fig. 6.8(a) to Fig. 6.8(b) using the calculated helix radius r_y as mentioned above. It should be noted that the accuracy of the mean yarn circumferential velocity v_{yc} in the downstream region of the straight tube in Fig. 6.8(b) is not high. v_{yc} increases and then decreases as z increases. v_{yc} does not show positive correlation with v_{ac}. This is against expectations because circumferential component of air velocity v_{ac} decreases with increasing z in the downstream region of the yarn propulsion tube from the throat, as presented in Fig. 3.19. The strong friction between the yarn and the wall retards the yarn motion in the de Laval tube; this may be the reason why v_{yc} is small relatively in the de Laval tube ($z < 0$ mm). The yarn still moves very quickly in the circumferential direction in the straight tube because of smaller helix diameter than tube diameter (= 20 mm), which greatly reduces yarn moving

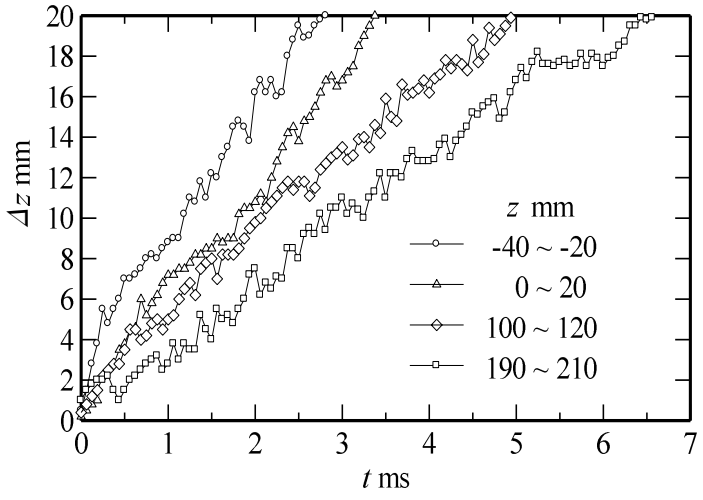

Figure 6.7 Yarn covered distance Δz as a function of time t ($\phi = 150°$, $\theta = 60°$, $\alpha = 90°$ and $D = 10$ mm).

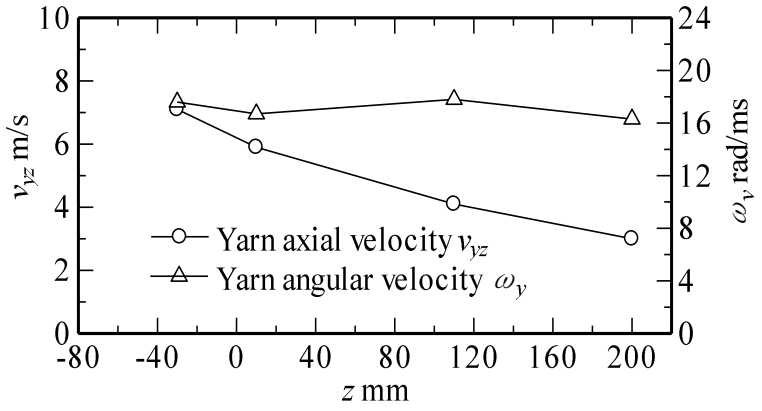

(a) Mean yarn axial velocity v_{yz} and mean angular velocity ω_y

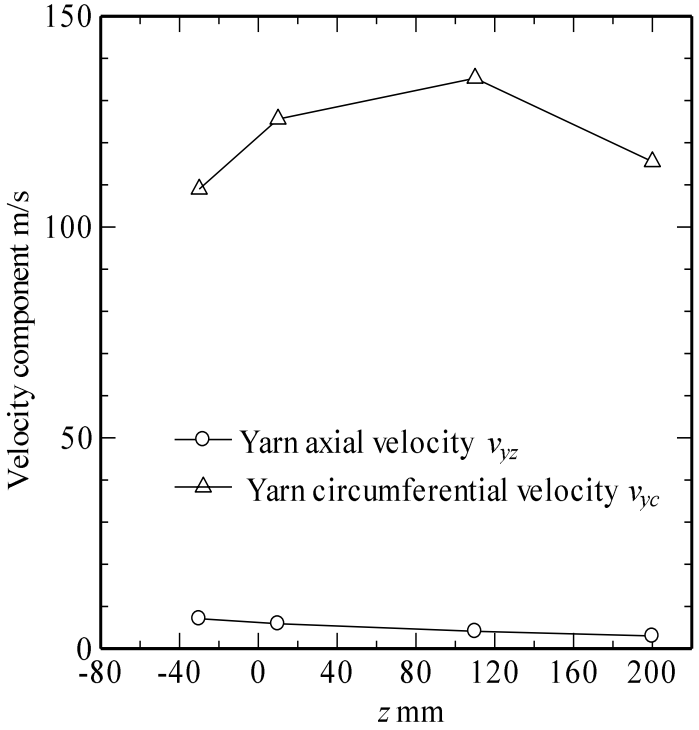

(b) Mean yarn axial velocity v_{yz} and mean yarn circumferential velocity v_{yc}

Figure 6.8 Mean yarn axial velocity v_{yz}, mean angular velocity ω_y and mean circumferential velocity v_{yc} in yarn suction gun ($\phi = 150°$, $\theta = 60°$, $\alpha = 90°$ and $D = 10$ mm).

resistance from the wall. Therefore, the yarn suction gun still provides the yarn with enough propulsion force in the straight tube, although the air velocity is smaller.

The mean yarn axial velocity v_{yz} and mean angular velocity ω_y are introduced to characterize the helical motion of the yarn in the following sections, because the accuracy of the mean yarn circumferential velocity v_{yc} in the straight tube is not high.

From Fig 6.4 we can see that the motion path of a yarn segment is different from the yarn posture in Fig. 5.3.

6.3.2 Effect of Compressed-air Inflow Angle ϕ on Yarn Motion

Figure 6.9 shows the effect of compressed-air inflow angle ϕ on the yarn motion in the region of z = -40 ~ -20 mm, where is in the middle of the de Laval tube. The results were obtained under the same condition as that for Fig. 6.4 except for $\phi = 120°$, 150° and 165°. The plots of x and y versus t at $\phi = 150°$ is the same as that in Fig. 4 (a), and therefore is not given here. The time and cycle number of the circular motion for the yarn travelling the same distance of 20 mm in z direction increase with ϕ. The yarn axial velocity v_{yz} decreases with an increase in ϕ, and the yarn angular velocity ω_y takes the maximum at $\phi = 150°$, as shown in Fig. 6.9(e). As ϕ is increased, the circumferential component of air velocity v_c increases as descried in Chapter 4; this causes an increase in the circumferential velocity of yarn v_{yc}, which increases ω_y. For too large ϕ such as 165°, however, it is relatively difficult for the injected compressed air to flow out of the throat in a favorable condition because of too small axial velocity component v_z, and more backflows are produced from outlets of the compressed-air inflow tubes. These result in the decrease of air velocity in the de Laval tube. Hence ω_y and v_{yz} are smaller at $\phi = 165°$ than at $\phi = 150°$.

Figure 6.10 presents v_{yz} and ω_y at different ϕ in the region of z = 100 ~ 120 mm, where is in the middle of the straight tube. The tendencies of v_{yz} and ω_y with respect to ϕ are similar to those shown in Fig. 6.9(d), but the effect of ϕ on the yarn motion is small, and the variations of v_{yz} can be neglected. It implies that the airflow distributions in the straight tube are similar in the range $120° \leqslant \phi \leqslant 165°$.

We now consider the relation between the yarn motion and yarn suction force F_m, which is indicated by yarn tension. F_m increases to the maximum value at ϕ = 150° and then decreases as ϕ is increased from 120° to 150° (see Fig. 4.5). F_m and ω_y present the similar trend with respect to ϕ. The helix pitch of yarn posture p_y becomes small as ω_y increases; this increases the length of the yarn in the airflow. Therefore, the frictional force between the air and the yarn becomes large because of the larger yarn surface that is in contact with air, and then F_m increases.

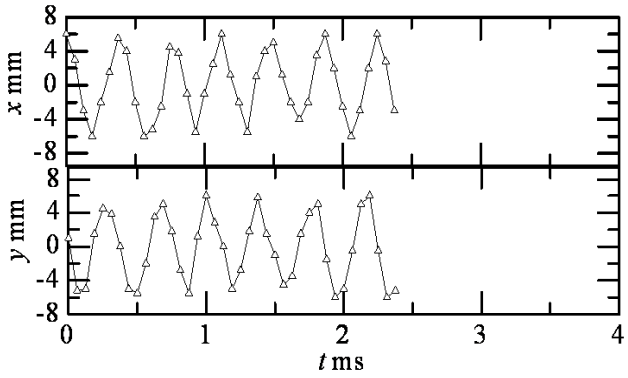

(a) x and y as a function of t at $\phi = 120°$

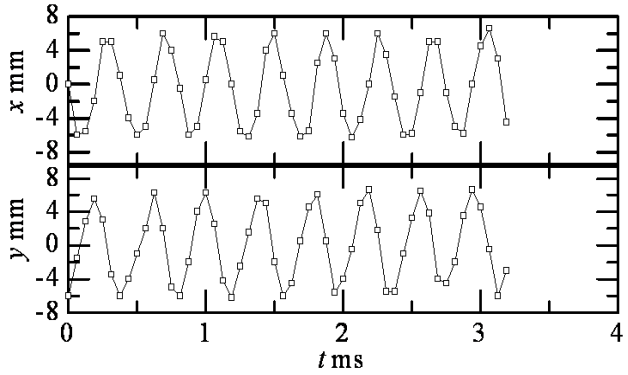

(b) x and y as a function of t at $\phi = 165°$

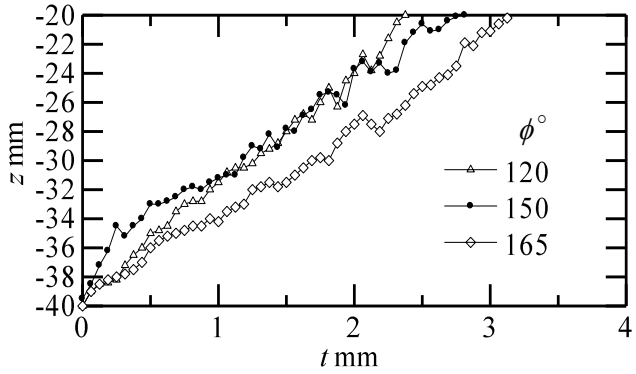

(c) z as a function of t

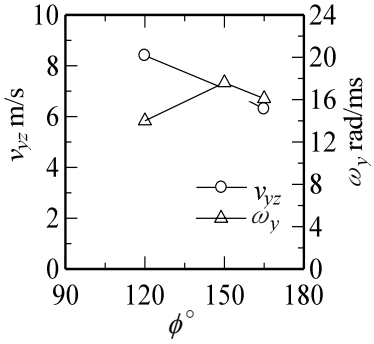

(d) v_{yz} and ω_y as a function of ϕ

Figure 6.9 Effect of compressed-air inflow angle ϕ on yarn motion in the middle of de Laval tube (z = -40 ~ -20 mm, $\theta = 60°$, $\alpha = 90°$ and D = 10 mm).

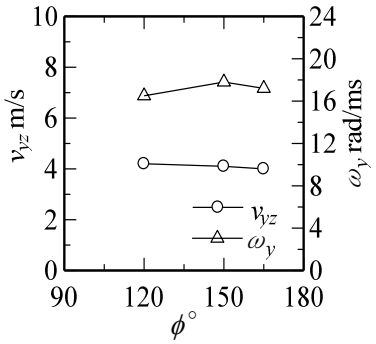

Figure 6.10 Yarn axial velocity v_{yz} and angular velocity ω_y in the middle of straight tube at different compressed-air inflow angle ϕ (z = 100 ~ 120 mm, θ = 60°, α = 90° and D = 10 mm).

6.3.3 Effect of Passage Diverging Angle of Nozzle θ on Yarn Motion

Figure 6.11 shows the yarn motion in the middle of the de Laval tube at different θ. The values of ϕ, α and D are fixed at 150°, 90° and 10 mm respectively. The plots of x and y versus t at θ = 60° is the same as that in Fig. 6.4 (a), and therefore is not presented here. As θ is increased, the yarn axial velocity v_{yz} increases and the yarn angular velocity ω_y decrease. However, the dependence of v_{yz} and ω_y on θ is much smaller than on ϕ.

The effect of θ on the yarn motion in the middle of the straight tube is also small, as shown in Fig. 6.12.

The diverging part of the nozzle is designed to provide surface to generate a tangential velocity component of the injected airflow, and to hinder the backflow from the outlets of the compressed-air inflow tubes. The airflow distribution in the yarn propulsion tube bears little relation to θ, as noted in Chapter 4. Hence the yarn motion shows a small dependence on θ.

Yarn suction force F_m attains the maximum value at θ = 60° as θ is changed from 30° to 90°, and F_m at θ = 30° is just a little smaller than at θ = 60° (see Fig. 4.10). F_m changes with θ in some different way to ω_y shown in Figs. 3.11 and 3.12. The reason is considered as follows: When θ is too small, more backflows from the outlets of compressed-air inflow tubes is generated in the diverging part of nozzle. This causes the velocity of the entrained ambient air in the yarn inhalation tube to decline, and then F_m becomes smaller.

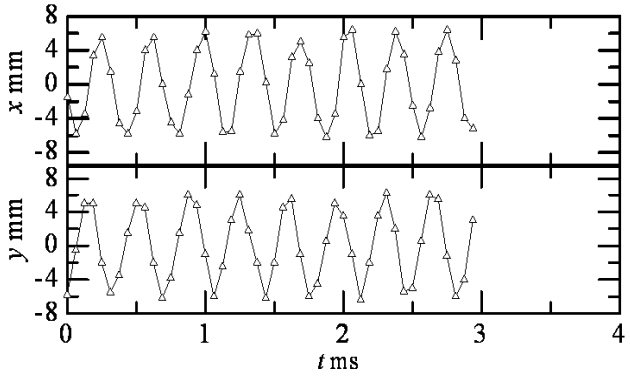

(a) x and y as a function of t at $\theta = 30°$

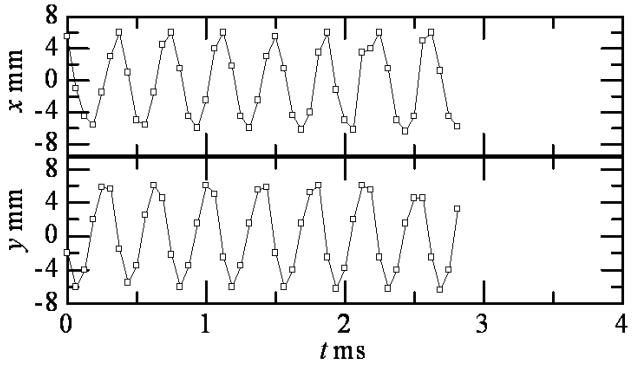

(b) x and y as a function of t at $\theta = 90°$

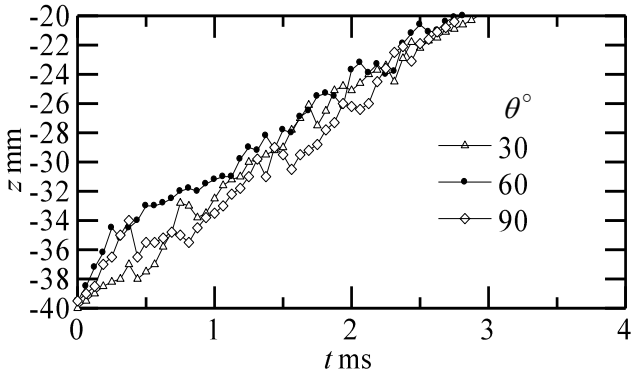

(c) z as a function of t

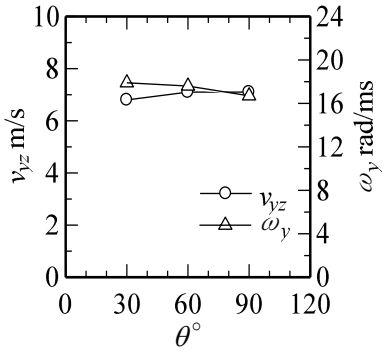

(d) v_{yz} and ω_y as a function of θ

Figure 6.11 Yarn motion in the middle of de Laval tube at different passage diverging angle of nozzle θ (z = -40 ~ -20 mm, ϕ = 150°, α = 90° and D = 10 mm).

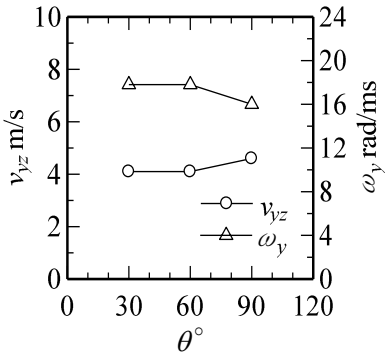

Figure 6.12 Yarn axial velocity v_{yz} and yarn angular velocity ω_y in the middle of straight tube at different passage diverging angle of nozzle θ (z = 100 ~ 120 mm, ϕ = 150°, α = 90° and D = 10 mm).

6.3.4 Effect of Converging Angle of de Laval Tube α on Yarn Motion

The effect of converging angle of de Laval tube α on the yarn motion in the middle of the de Laval tube is shown in Fig. 6.13. The other geometrical parameters are ϕ = 150°, θ = 60° and D = 10 mm. The plots of x and y versus t at α = 90° is not given in this figure because it has been given in Fig. 6.4(a). As α is increased, the yarn axial velocity v_{yz} decreases, and the yarn angular velocity ω_y increases. However, the yarn motion is more irregular at α = 120°.

Figure 6.14 shows v_{yz} and ω_y in the middle of the straight tube at different α. The effect of α on the yarn motion is smaller in the straight tube than in the de Laval tube; however the variation of ω_y with α in the straight tube presents a trend different from that in the de Laval tube shown in Fig. 6.13(d). The reason is considered that the yarn does not come in considerable contact with the tube wall in the straight tube as in the de Laval tube. In the straight tube the yarn motion may coincide more with the airflow distribution. v_{yz} becomes less closely related to ω_y because of more irregular yarn motion .

According to the experimental results, yarn suction force F_m reaches the maximum value at α = 90° (see Fig. 4.14). This coincides with the relation between ω_y and α shown in Fig. 6.14. F_m becomes small at α = 120° maybe because of the irregular yarn motion in Fig. 13(c).

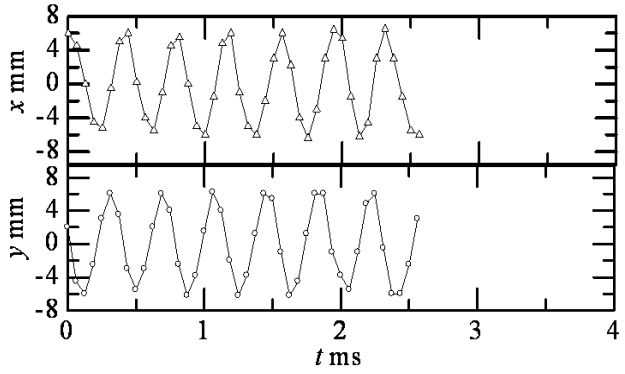

(a) x and y as a function of t at $\alpha = 60°$

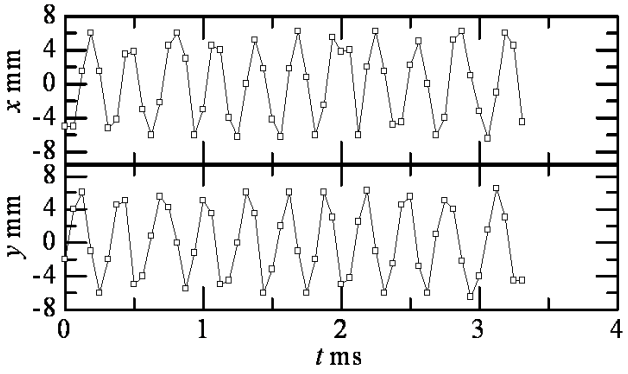

(b) x and y as a function of t at $\alpha = 120°$

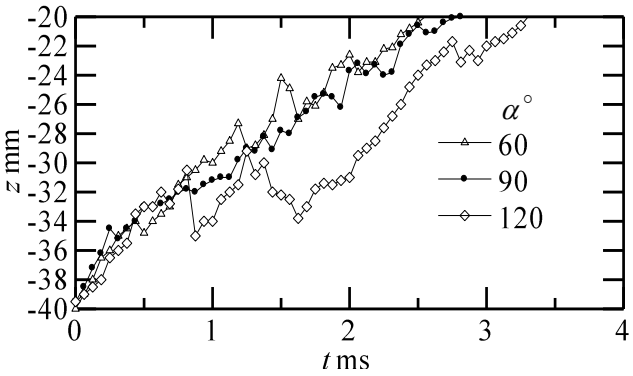

(c) z as a function of t

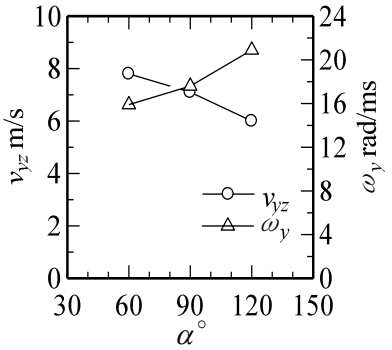

(d) v_{yz} and ω_y as a function of α

Figure 6.13 Yarn motion in the middle of de Laval tube at different converging angle of de Laval tube α (z = -40 ~ -20 mm, ϕ = 150°, θ = 60° and D = 10 mm).

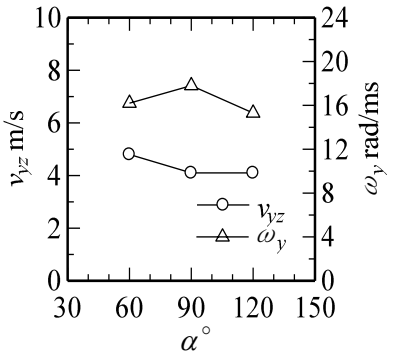

Figure 6.14 v_{yz} and ω_y in the middle of straight tube at different converging angle of de Laval tube α (z = 100 ~ 120 mm, ϕ = 150°, θ = 60° and D = 10 mm).

6.3.5 Effect of Throat Diameter of de Laval Tube *D* on Yarn Motion

Figure 6.15 shows the effect of throat diameter of de Laval tube D on the yarn motion in the middle of the de Laval tube. The other three geometrical parameters are fixed at ϕ = 150°, θ = 60° and α = 90°. The plots of x and y versus t at D = 10 mm is also the same as that in Fig. 6.4(a), and therefore is not shown here. As D is increased, the yarn axial velocity v_{yz} increases while the yarn angular velocity ω_y decreases. So a yarn segment covers a longer distance when going through the de Laval tube with smaller D because of small v_{yz}.

The profiles of v_{yz} and ω_y in the middle of the straight tube at different D are plotted in Fig. 6.16. By comparing Fig. 6.15 (d) and Fig. 6.16, it is clear that D has a great effect on the yarn motion in the de Laval tube and the straight tube in a similar way.

In theory, v_{yz} will decrease as D is increased because axial component of air velocity v_z decreases with increasing D as depicted in Fig. 4.17. However, v_{yz} does not follow this theory. Thus the yarn motion may be mainly determined by circumferential component of air velocity v_c in and shows less relation to v_z.

As D is decreased, yarn suction force F_m should increase because of the increased ω_y and air velocity. However, the maximum of F_m is achieved at D = 10 mm (see Fig. 4.18). So other factors should be taken into account. Air velocity in the yarn inhalation tube decreases with D; this causes the yarn drag force produced in the yarn inhalation tube to decrease. F_m will decrease when the reduction of the yarn drag force in the yarn inhalation tube is larger than the increase in the yarn drag force in the yarn propulsion tube. For example, this case occurs at D = 9 mm.

Generally, the dependency of yarn motion on D is comparatively larger than those on ϕ, θ and α. It implies that D has the largest effect on the airflow than ϕ, θ and α, which is also presented in Sec. 4.4.

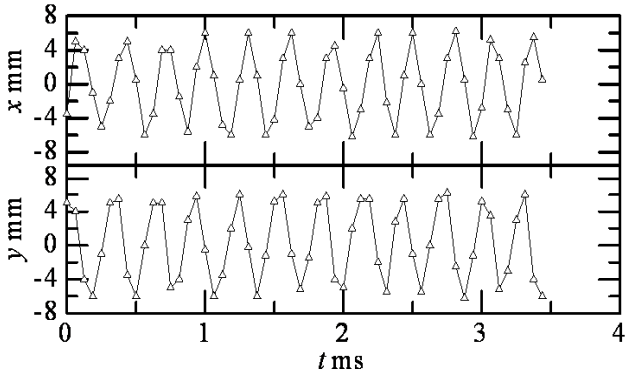

(a) x and y as a function of t at D = 9 mm

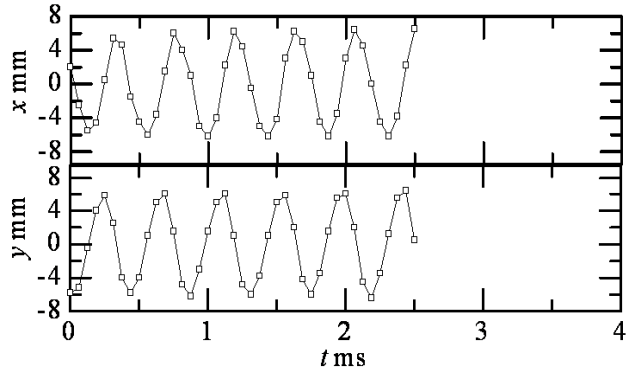

(b) x and y as a function of t at D = 11 mm

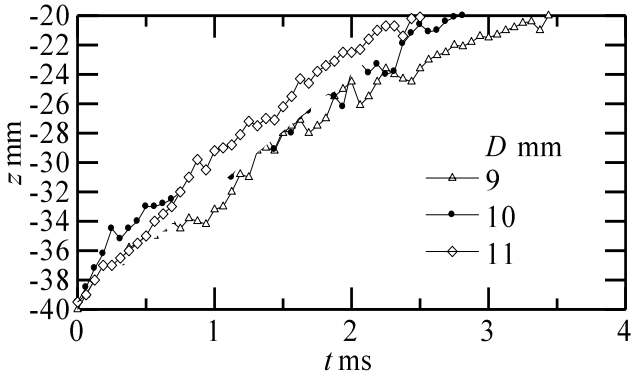

(c) z as a function of t

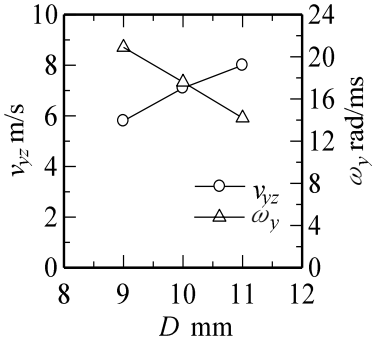

(d) v_{yz} and ω_y as a function of D

Figure 6.15 Yarn motion in the middle of the de Laval tube at different throat diameter of de Laval tube D (z = -40 ~ -20 mm, ϕ = 150°, θ = 60° and α = 90°).

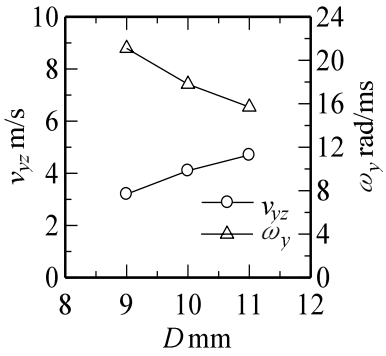

Figure 6.16 Yarn axial velocity v_{yz} and angular velocity ω_y in the middle of straight tube at different throat diameter of de Laval tube D (z = 100 ~ 120 mm, ϕ = 150°, θ = 60° and α = 90°).

Taking into consideration the relation between the yarn motion and the yarn suction force F_m, we can conclude that F_m depends more strongly on ω_y than on v_{yz}.

6.4 Conclusions

For clarifying the yarn behavior in a yarn suction gun, we investigated the motion of a running yarn in the gun with a high-speed video camera and analyzed the geometrical effects on the yarn motion. The relation between the geometrical parameters and the yarn motion is summarized in Table 6.2. Results obtained are as follows:

(1) A yarn moves forward in the yarn propulsion tube with a high-speed rotation. It performs the helical motion more regularly in the de Laval tube than in the straight tube. The yarn motion is unsteady and the motion path is different from the yarn posture.

Table 2 Relation between geometrical parameters and yarn motion

Increasing geometrical parameter	ϕ	θ	α	D
In de Laval tube				
In straight tube				
Yarn suction force F_m				

Note: —○— v_{yz} —△— ω_y

(2) The friction from the tube wall has a considerable effect on the yarn motion, particularly on the yarn circumferential velocity v_{yc}. The strong friction gives rise to a large reduction in v_{yc}.

(3) Both increases in compressed-air inflow angle ϕ and converging angle of de Laval tube α cause yarn angular velocity ω_y to increase and then decrease. As throat diameter of de Laval tube D is decreased, ω_y increases and yarn axial velocity v_{yz} decreases. Yarn motion is almost independent of θ. Its dependency on D is comparatively larger than on ϕ, θ and α.

(4) Yarn motion shows a stronger sensitivity to the circumferential component of air velocity than the axial one.

(5) Yarn suction force F_m is associated with various effects, but depends on v_{yc} in particular. I**t** has been demonstrated here that a high F_m are possible to be obtained by a rational geometrical design which can produce favourable helical flow with appopriate swirl intensity, an increment of which increases both the air drag on a yarn and the friction between the yarn and the tube wall.

References

[1] Iemoto Y, Chono S, Tanaka T (1998) Study on interlaced yarn Part 4: Yarn posture in interlacer, and relation between yarn postures and number of tangles. *J Text Mach Soc Japan* (predecessor journal of *J Text Eng*), **44**, 57-63

[2] Iemoto Y, Chono S, Tanaka T (1999) Study on interlaced yarn Part 6: Yarn motion in interlacer. *J Text Mach Soc Japan* (predecessor journal of *J Text Eng*), **45**, 44-50

[3] Chono S, Iemoto Y (1999) Study on interlaced yarn Part 7: Yarn motion in interlacer and production mechanism of tangling part. *J Text Mach Soc Japan* (predecessor journal of *J Text Eng*), **45**, 108-112

[4] Qiu H, Iemoto Y and Tanoue S (2007) Yarn motion in interlacers with various cross-sectional shapes of yarn duct. *J Text Eng*, **53**, 59-67

[5] Kitoh O (1991). Experimental study of turbulent swirling flow in a straight tube. *J. Fluid Mech*, **225**, 445-479

[6] Finnemore E. J, Franzini J. B (2003) *Fluid Mechanics with Engineering Application (10th ed)*, p100, McGraw-Hill Companies, Inc., New York, USA

[7] Adanur S, Bakhtiyarov S (1996) Analysis of air flow in single nozzle air-jet filling insertion: corrugated channel model. *Text Res J*, **66**, 401-406

[8] Adanur S, Mohamed M (1992) Analysis of yarn motion in single-nozzle air-jet filling insertion. Part II: Experimental validation of the theoretical models and statistical analysis. *J Textile Inst*. **83**, 56-68

Chapter 7
Conclusions and Future Research

In this chapter, a summary of the experimental and theoretical work performed, major conclusions, and recommendations for future research are presented.

7.1 Conclusions

Yarn suction gun plays an important role in yarn production. A desirable yarn suction gun should have high suction capacity, keeping the cost as low as possible. Improvement of the performance has been the major issue in this area.

In this dissertation we have conducted a systematic research on a yarn suction gun by investigating the geometrical effects on the yarn suction efficiency, airflow patterns and yarn behavior, and derived a yarn suction gun with high performance. A basic explanation of the working mechanism has been presented in this work, which is believed to be useful for designing new types of the yarn suction gun.

7.1.1 Concluding Remarks on Geometry and Suction Performance of Yarn Suction Gun

In Chapter 2 an attempt was made to experimentally discuss effects of airflow geometries in a yarn suction gun on the suction characteristics of running yarn, so as to provide the maximum yarn suction force with the minimum consumption of compressed air. It was shown that yarn suction efficiency η, which is defined as the yarn suction force F_m divided by mass flow rate of compressed-air, is obviously affected by converging angle of de Laval tube α and throat diameter of de Laval tube D, especially it strongly depends on compressed-air inflow angle ϕ. Passage diverging angle of nozzle θ has little effect on η. The study has suggested the optimum geometry of a yarn suction gun on the basis of η, which is ϕ = 150°, θ = 60°, α = 90°, D = 10 mm and L = 300 mm. In addition, F_m shows two types of time dependency under the same experimental conditions. Both F_m and η decrease with an increase in the yarn feed speed. As the supplied air pressure is increased, F_m increases, but η decreases. Not only has this study revealed the essential features of the yarn suction gun, but also it has generated significant information on the operation conditions necessary for the gun.

7.1.2 Concluding Remarks on Airflow Characteristics of Yarn Suction Gun

In Chapter 3 we investigated numerically flow patterns in the yarn suction gun with the optimum geometry and dependence of the flow pattern on the supplied air pressure p_0, in order to clarify the working mechanism of the gun and achieve an effective method to investigate the airflow in the gun using CFD. A compressible finite element model was proposed to model the behavior of airflow in the yarn suction gun at p_0 = 0.6 MPa. The simulation has revealed that the compressed air issued from compressed-air inflow tubes, which is supersonic, accelerates with the sucked ambient air in the converging part of de Laval tube, and keeps accelerating in the divergent part. The supersonic flow generates a normal shock wave and changes into a subsonic flow. Then, the air is discharged into the atmosphere. Since this compressed air has a circumferential component, it forms a helical flow in the yarn propulsion tube composed of the de Laval tube and the straight tube. Velocity and density of the helical airflow near the wall are larger than those near the centerline. Hence we can conclude that the suction efficiency is promoted greatly owing to this high focusing ability (bias of high speed and density flow toward the vicinity of the wall) and a large yarn length in the helical airflow. We have also found that increasing supplied air pressure brings about increases in both air density and supersonic flow region, which promotes the yarn suction force, but the normal shock wave generated by large p_0 lowers the yarn suction efficiency. It is suggested that the yarn suction gun should be operated at appropriate supplied air pressure. This simulation is an important step towards understanding the yarn suction process. The model, which is also supported by experimental evidence, can be used a numerical tool to design an efficient yarn suction gun.

In Chapter 4 numerical simulation was performed to investigate the airflow patterns in the yarn suction gun with different geometrical parameters and analyze the relation between the flow patterns and yarn suction force F_m, for a further understanding of the working mechanism and obtaining a basic theory for the optimum design. This study has shown that the compressed-air inflow angle plays an important role in generating a helical flow by controlling circumferential velocity component v_c of air in the yarn propulsion tube. This helical airflow greatly promotes yarn suction capacity. F_m has a closer relationship to the distribution of air velocity than air pressure, and strongly depends on v_c. The airflow patterns are weakly dependent on the passage diverging angle of nozzle and the converging angle of de Laval tube. A reduction in the throat diameter of de Laval tube causes a rapid extension of the supersonic flow area near the throat accompanied by increasing axial velocity component in the de Laval tube. However, it leads to decreases in v_c in the yarn propulsion tube and air

velocity in the yarn inhalation tube, which hinders the promotion of F_m. The numerical study has established the feasibility of designing a yarn suction gun by simulation. Based on the results of simulations, the suggested design of the yarn suction gun agrees with the one in Chapter 2.

7.1.3 Concluding Remarks on Yarn Behavior in Yarn Suction Gun

In Chapter 5 the geometrical effects of a yarn suction gun on yarn behavior were clarified by measuring postures of a running yarn with a still camera, with the aim of clarifying the working mechanism of the gun and then promoting the suction performance by controlling the yarn motion appropriately. The relation between the yarn posture and yarn suction force was also discussed. It is found that the yarn posture is a helix. This helical motion greatly improves the yarn suction efficiency owing to high concentration of air drag on the yarn. Helix diameter of yarn posture d_y and helix pitch of yarn posture p_y decrease with an increase in the compressed-air inflow angle and a decrease in the throat diameter of de Laval tube, and are almost independent of the passage diverging angle of nozzle and the converging angle of de Laval tube. Unfavorable values of geometrical parameters cause large fluctuations in yarn postures, i.e. violent yarn motion. This study indicated that a stable yarn posture with appropriately small d_y decreases the friction between the yarn and the wall of tube, and an appropriately small p_y increases the contact area between the yarn and the air. Hence the yarn suction force is promoted. The experimental analysis has suggested the possibility of obtaining high suction efficiency by controlling the yarn motion with appropriate airflow in the yarn suction gun.

Yarn motion, i.e. yarn position as a function of time, is indispensable for clarifying the working mechanism of the yarn suction gun. Therefore, yarn motion in different regions of a yarn suction gun and geometrical effects on the yarn motion were analyzed with a high-speed video camera in Chapter 6 for the purpose of gaining a physical insight into the yarn behavior in the gun. The analysis has shown that a yarn moves in the yarn propulsion tube with a high-speed rotation. It performs the helical motion more regularly in the de Laval tube than in the straight tube. The yarn motion is unsteady and the motion path is different from the yarn posture. Both increases in the compressed-air inflow angle ϕ and the converging angle of de Laval tube α cause yarn angular velocity ω_y to increase and then decrease. As the throat diameter of de Laval tube D is decreased, ω_y increases and yarn axial velocity v_{yz} decreases. The yarn motion is almost independent of θ. Its dependency on D is comparatively larger than

on ϕ, θ and α. The yarn motion shows a stronger sensitivity to the circumferential component of air velocity than the axial one. The yarn suction force depends more strongly on ω_y.

The approach in this dissertation has theoretically enabled us to consider the design of a new class of yarn suction gun.

7.2 Future Research

In this section we consider possible future development of the idea presented in this work. These fall into three major areas: improvements in the suction efficiency, enhancement of the predication accuracy of simulation and theoretical calculation of yarn suction force.

7.2.1 Improvements in Suction Efficiency

We intend to continue to improve the yarn suction gun for greater efficiency and ease of use. The world is going forward to the objective of low carbon, energy saving, environmental protection in more rapid pace. A reasonable design of the yarn suction gun can make it more energy efficient. Therefore it is a long-term work for us to improve the energy efficiency of the gun by experimentally and numerically optimizing the geometric design. Some new type of yarn suction guns will be designed on the basis of the present research with the goal of reducing energy use and costs to obtain improved performance. For example, the geometries of the nozzle and the de Laval tube need further research. Improving the performance of a product is endless and is a natural goal.

7.2.2 Enhancement of Predication Accuracy of Simulation

There are different ranges of applicability of different turbulence models. A suitable turbulence model will offer high accuracy. In the present work, the simulation was performed with the k-ε model, which is considered to be the most fundamental turbulence model, and gave the reasonable results compared with the experimental ones. However, the accuracy is not high in the region where shock wave occurs. Therefore applicability of other turbulence models to the airflow simulation in the yarn suction gun will be studied in the future. We believe that a proper treatment of the turbulence model will exhibit higher qualities of prediction.

We can select to use the First Order advection scheme, the High Solution scheme or specify a blend factor to blend between first and second advection schemes to calculate

advection terms in the discrete finite volume equation. In this dissertation, we have used the High Solution scheme to perform the calculation. We recommend that calculation should be carried out by trying to specifying the blend factor in the future in order to achieve higher accuracy.

In the present research, a comparison between the experimental and simulated wall pressures was made in a limited range. Extensive test will be conducted in the future.

In the present research, numerical simulation was carried out under the condition without a yarn in the yarn passage. Since the air in the yarn passage flows together with a yarn, the actual airflow will be a little different form that without a yarn. We will calculate the airflow in the yarn suction gun with a yarn in the passage in the future although the involved yarn considerably complicates the calculation.

7.2.3 Theoretical Calculation of Yarn Suction Force

Calculating the yarn suction force according to a streamline is quite challenging because: 1) The streamline depends on the original point; 2) The streamline is different from the posture of a running yarn; 3) Mathematical treatment will be fairly complex because it is hard to trace the helical streamline in the present yarn suction gun. But it is well worth the effort. We will study it in the future.

Finally, extending this work to new features and styles of yarn suction gun will require new thinking and creative work, and a lot of new issue will be raised. We look forward to further developments for higher performance in days to come.

Publications

Journal Papers

[1] IEMOTO Yoshiyuki, TANOUE Shuichi, HOSOKAWA Jun-ichi, LI Yonguui, MASUDA Atsuji, MURAKAMI Tetsuhiko. Geometry effect of air suction gun on the yarn suction characteristics. *Journal of Textile Engineering*, Vol. 54, No.2, 2008, pages 41-47.

[2] LI Yonggui, IEMOTO Yoshiyuki, TANOUE Shuichi, TAKASU Satoshi. Numerical simulation of airflow characteristics in air suction gun. *Journal of Textile Engineering*, Vol. 56, No. 4, 2010, pages 97-106.

[3] LI Yonggui, IEMOTO Yoshiyuki, TANOUE Shuichi, TAKASU Satoshi. "Numerical analysis of the geometrical effects on the airflow characteristics of an air suction gun" *Journal of Textile Engineering*, Vol. 56, No. 6, 2010 (to be published).

[4] LI Yonggui, IEMOTO Yoshiyuki, TANOUE Shuichi, Yarn posture in an air suction gun. *Journal of Textile Engineering*, Vol. 56, No. 6, 2010 (to be published).

[5] LI Yonggui, IEMOTO Yoshiyuki, TANOUE Shuichi, Yarn motion in an air suction gun. *Journal of Textile Engineering*, (in preparing).

International Conference Papers

[1] Yonggui Li, Yoshiyuki Iemoto, Shuichi Tanoue. Geometry effect of air suction gun on the yarn motion. *Proceedings of the 37th Textile Research Symposium*, August 20-22, 2008, Daegu, Korea.

[2] Yonggui Li, Yoshiyuki Iemoto, Shuichi Tanoue. Effect of air suction gun geometry on characteristics of air flow. *Proceedings of the 10th Asian Textile Conference (ATC-10)*, September 7-9, 2009, Ueda, Japan.

Domestic Conference Papers

[1] LI Yonggui, IEMOTO Yoshiyuki, TANOUE Shuichi, KANOU Akinobu. Yarn motion in an air suction gun. *Proceedings of the 61th Annual Meeting of the Textile Machinery* Society of Japan, May 29-30, 2008, Osaka, Japan.

[2] Yonggui Li, Yoshiyuki Iemoto, Shuichi Tanoue. Relation between geometry of air suction gun and yarn motion. *Proceedings of the 17th Symposium of the Textile Association of Japan*, Aug. 28-29, 2008, Nara, Japan.

Acknowledgements

My highest gratitude goes to my supervisor, Professor Yoshiyuki Iemoto, for his supervision, constructive comments, encouragement and patience throughout this research work. Without his help, this work would not have been completed. He has been an inspiration, a constant source of encouragement, and the warmest of friends. Not only has he enabled me to develop necessary research skills for a successful research study, but also he has enlightened the way to a fruitful academic life. I especially have benefited greatly from his rigorous scholarship.

I would like to express my appreciation to Associate Professor Shuichi Tanoue for the many valuable comments, suggestions and support for this work.

My earnest thanks go to Professor Susumu Saeki, Professor Nobuo Ogata and Professor Jun-ichi Ohta. Their constructive comments have surely enhanced the quality of this dissertation.

My deep thanks go to also Professor Shinji Yamaguchi and Assistant Professor Hideyukui Uematsu for their enthusiastic supports.

Sincere thanks are expressed to in-depth reviews and thoughtful comments from the anonymous referees arranged by *Journal of Textile Engineering*, which has made the dissertation clearer, more correct, and improved.

Sincere gratitude goes to the Monbu-kagakusho of Japan and University of Fukui for the scholarship and travel grant, without which my study at University of Fukui would have been impossible.

I thank all members of Polymer Processing Laboratory for making my overall stay in Japan sweet and memorable. Particularly, my heartfelt thanks go to Mr. Jun-ichi Hosokawa, Mr. Satoshi Takasu, Mr. Suguru Kitagawa and Mr. Akinobu Kanou for their cooperation and relentless support to make this work possible.

I would like to thank Professor Mingqiao Ge, Jiangnan University, China, for his encouragement.

Finally, I am deeply grateful to all my families, for too much to say, but especially for their support to pursue the PhD. I must express my great appreciation to my wife, who suffered the most from living separately with me during my study for this dissertation. My special thanks go to my lovely daughter. She is always a source of great joy and motivation.

Yonggui Li